Supernova Remnants Selected with X-Rays

— Contribution to the Galactic Cosmic-Ray Acceleration

Masaru Ueno

Department of Physics, Graduate School of Science, Kyoto University
Kitashirakawa Oiwake-cho, Sakyo-ku, Kyoto, 606-8502, Japan
masaru@cr.scphys.kyoto-u.ac.jp

This thesis was submitted to the Department of Physics,
Graduate School of Science, Kyoto University
on January 5, 2005
in partial fulfillment of the requirements
for the degree of Doctor of Philosophy in physics.

Abstract

SNRs have been the primary candidate for the galactic cosmic-ray acceleration, because of the large energy output. Since the discovery of synchrotron X-ray emission from SN 1006, nowadays synchrotron X-ray and Tev-gamma rays have been detected from several SNRs. Thus, existence of high energy particles in SNRs are being established. However, among more than 200 galactic SNRs, existence of high energy particles ($\sim$ 1 TeV) are shown in only about 10 SNRs. And as a result, we do not know in which SNRs high energy particles are accelerated. SNRs have been mainly discovered with radio surveys. However, SNRs emitting synchrotron X-rays, such as SN 1006 or G347.3−0.5 are tend to be faint in radio. Therefore, we noticed SNRs discovered X-rays or X-ray selected SNRs.

First, we analyzed *XMM-Newton* data of SNRs discovered with the *ROSAT* All Sky Survey. With *ASCA* observations, hard X-ray emission in G156.2+5.7 has already been known. Spatially resolving the contribution of point sources with *XMM-Newton*, we confirmed the hard X-ray emission is truly diffuse. Due to the high background, however, we could not determine the emission mechanism of the hard X-rays. We performed spatially-resolved spectroscopy on G272.2−3.2 and G299.2−2.9, resulting in no detection of non-thermal X-ray emission.

Next, we searched SNR candidates with the *ASCA* Galactic Plane Survey. The *ASCA* Galactic Plane Survey is the first imaging survey of the Galactic plane in the energy band >3 keV. We made exposure corrected image and analyses the survey data in detail. As a result, 15 extended X-ray sources were found in the hard band (2.0–7.0 keV). Although several sources are likely to be star-forming regions, pulsar-wind nebulae or clusters of galaxies, most of the new sources are likely to be SNRs.

Follow-up observations with *ASCA*, *XMM-Newton*, and *Chandra* have been performed on 5 of the new extended sources. As a result, G28.6−0.1 and G32.45+0.1 are established as SNRs emitting synchrotron X-rays. Although we confirmed non-thermal X-ray emission from G11.0+0.0, G25.5−0.1, and G26.6−0.1, observations with higher spatial resolution is required to find out the emission mechanism and their origins.

SNRs are known to get fainter in radio as they evolve, which is known as the Σ-D (radio surface brightness vs. diameter) relation. When we compared the SNRs emitting synchrotron X-rays with other SNRs, we found the former are faint in radio even when they are young. Since SNR brightnesses in radio have dependency on the ambient density, we suggest SNRs emitting synchrotron X-rays are located in low density media.

Contents

List of Figures

List of Tables

Chapter 1

Introduction

Supernovae are energetic explosions of stars at the ends of their lives. The total energy released in one event is up to 10^{53} ergs, most part of which is emitted as neutrinos, and 1/100 is emitted as kinetic energy of the surrounding matter. Along the explosions, elements produced in the progenitor stars and also those produced during the explosions are distributed outwards, and change the composition of the interstellar matter. Therefore, supernovae have significant influence on chemical evolution of galaxies. The kinetic energy of supernovae may also trigger next births of stars, compressing ambient molecular clouds. Supernova are important events in understanding evolutions of the interstellar matter.

We here concentrate on the aspect of supernovae as an origin of cosmic rays. The origin of cosmic rays has been a mystery since the discovery by Hess in 1912. The spectrum of cosmic rays showering onto the earth has been intensively studied, and nowadays it is known that the spectrum continues up to 10^{22} eV. However, the origin of cosmic rays even with energy of 10^{15} eV is yet unknown. Since cosmic rays themselves are charged particles, their directions are easily changed by the magnetic field filling the galaxy. For example, a proton of energy 10^{15} eV in a magnetic field of ~ 1 μG gyrates with a radius of 0.3 pc. Therefore, it is hard to know where cosmic rays come from. One of the break through was made by an observation with X-rays, which travel straight. Koyama et al. (1995) found synchrotron X-ray emissions from a supernova remnant, SN1006, which discovery showed existence of high energy electrons in the supernova remnant. Recently, TeV gamma rays are also detected from several supernova remnants, and existence of high energy particles in supernova remnants is getting firmly evidenced.

Because of the enormous energy input, supernova remnants have been a primary candidate for the acceleration site of the galactic cosmic rays. Now the discovery of synchrotron

X-rays and TeV gamma rays evidenced existence of high energy particles in supernova remnants. However, a question of what fraction of the galactic cosmic rays can be explained with supernova remnants is not yet solved. In order to answer this question we have to know roughly two things; How much energy is injected in each supernova remnants and how many supernova remnants are located in our Galaxy. We know only small number of supernova remnants showing evidence of acceleration, which is making the above systematic study difficult.

In order to work on these problems, we use X-ray observations which have many advantages in studying the acceleration in supernova remnants. First of all, the X-ray band is just the wavelength of synchrotron emission from high energy electrons of energy $\sim 10^{13}$ eV in a typical magnetic field of ~ 3 μG in the Galactic plane. X-rays, especially in the high energy band, have strong penetrating power through the interstellar matter, so that even clusters of galaxies behind the galactic plane can be observed. Nowadays, the instruments of X-ray observations are highly developed and as a result they are equipped with large effective areas, high energy resolution, and high imaging capability. These advantages are reflected to the situation that acceleration in a new supernova remnant has been evidenced mostly by detection of a synchrotron X-ray emission.

In this thesis, we concentrate on a study of supernova remnants selected with X-rays. The rate of synchrotron X-ray detection from SNRs which are discovered with X-rays is much higher than that from SNRs discovered with other wavelengths. First of all, in Chapter 4, we analyze supernova remnants discovered with the *ROSAT* All Sky Survey. In Chapter 5, we report on search for supernova remnants using the *ASCA* Galactic Plane Survey. We have performed follow-up observations on a part of the newly discovered candidates with *ASCA*, *Chandra*, and *XMM-Newton*, which will be explained in Chapter 6. We will discuss overall characteristics of the X-ray selected SNRs and their contribution to the galactic cosmic-ray acceleration in Chapter 7.

Chapter 2

Reviews

2.1 Cosmic Ray

Cosmic rays are discovered by Victor Hess in 1912. He measured the ionization level of the atmosphere up to 5 km altitude on a balloon and found that some radiation must come from space to explain the ionization state of the atmosphere. After that, many experiments have been done and the spectrum and the composition of cosmic rays have been measured extensively. However, the origin of the cosmic rays are yet unknown. In this section, we summarize the properties of the cosmic rays, which are the key information to constrain their origin.

2.1.1 Spectrum

Figure 2.1 shows the energy spectrum of cosmic rays (the vertical axis is differential flux multiplied by $E^{2.5}$). The spectrum extends up to $\sim 10^{20}$ eV at least, which is much higher than the energy obtained with any particle accelerators on earth. The spectrum is almost power-law like and featureless with few breaks. The break at $\sim 10^{15.5}$ eV is called "knee". (There is also another break at $\sim 10^{20}$ eV called "ankle".) The spectrum up to 10^{20} eV can be expressed quite well as:

$$N(E) \sim 10^{-2.7} (<\sim 10^{15.5} \text{ eV}) \tag{2.1}$$

$$N(E) \sim 10^{-3.0} (>\sim 10^{15.5} \text{ eV}). \tag{2.2}$$

The "knee" is one of the few features informing the origin of the cosmic ray. The energy densities of cosmic rays in the galactic plane is 1 eV cm^{-3}, which is large compared with that of the starlight, galactic magnetic field, or the cosmic micro-wave background ($\simeq 0.3$ eV cm^{-3}).

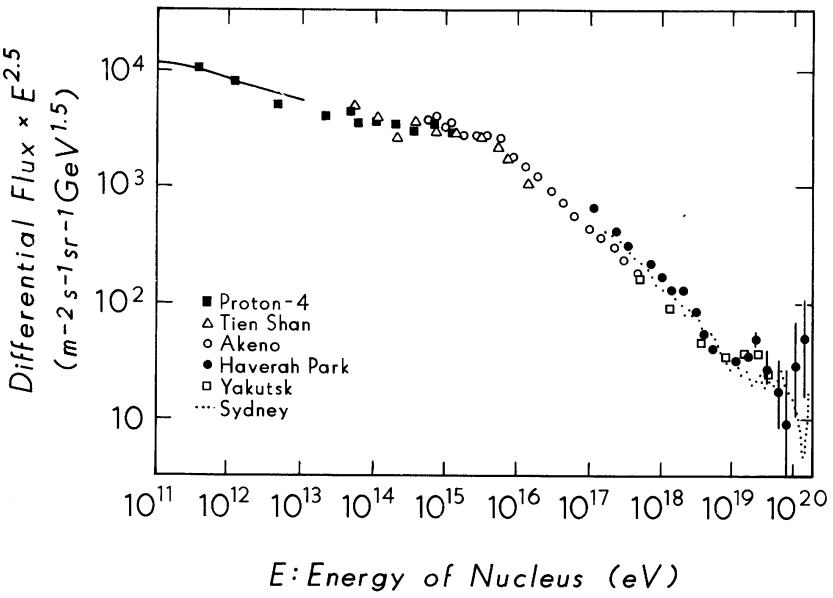

Figure 2.1: Energy spectrum of cosmic-ray protons (Sokolsky, 1989). The horizontal axis is energy of each proton, and the vertical is (differential flux) $\times$ (energy)$^{2.5}$.

2.1.2 Chemical Composition

Figure 2.2 shows the chemical composition of cosmic rays in comparison with the solar abundance. In a way similar to the solar abundance, the species with even atomic number are more abundant than those with odd number, though the difference is smaller than the solar values. Heavy elements are more abundant than the solar. It is notable cosmic rays are significantly overabundant in Lithium, Beryllium, and Boron. Since these elements are not produced either in the primordial nucleosynthesis or in the stellar evolution, it is thought that they themselves are not accelerated but they are produced by spallation, or inelastic interaction of cosmic rays with the interstellar matter. Using the cross sections of the spallations, the column density along the pass of cosmic rays from the birth place to the earth is estimated to be $\sim$5–10 g cm^{-2}. For a density of 1 proton cm^{-3}, the travel distance is estimated to to be $\sim$1000 kpc, which is much larger than the diameter of our Galaxy. Therefore, cosmic rays should be confined by the galactic magnetic field.

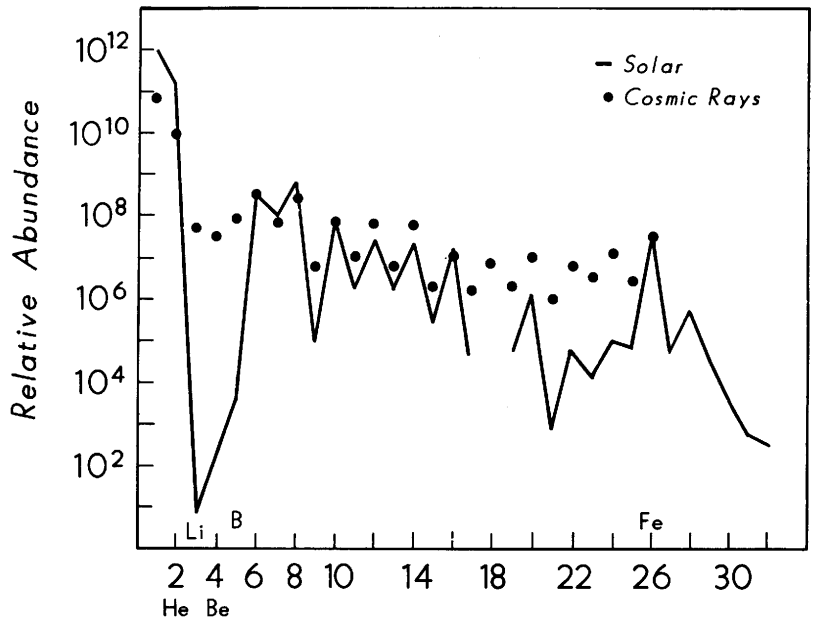

Figure 2.2: Chemical composition of cosmic rays (Sokolsky, 1989). The horizontal axis is atomic number, and the vertical axis is relative abundance. For comparison, the solar abundance, is designated with the solid line.

2.1.3 Energy Budget

If we assume the lifetime of cosmic rays is detemined mainly by escape from the Galaxy, the energy for maintaining the cosmic rays in our Galaxy ($L_{\rm cr}$) can be estimated from the life-time $t_{\rm cr}$, the energy density $\epsilon_{\rm cr}$, and the volume filled by cosmic rays V_G as

$$L_{\rm cr} = \frac{V_G \epsilon}{t_{\rm cr}}. \tag{2.3}$$

The life-time of cosmic rays is estimated from the observation of radio isotopes such as ^{10}B, and is known to be $t_{\rm cr} \sim 6 \times 10^6$ yr. As mentioned above, the energy density is $\epsilon \sim 1$ eV cm^{-3}. The volume filled by cosmic rays is approximated as

$$V_G \simeq \pi \times r_g^2 \times d_g \sim \pi \times (15 \text{ kpc})^2 \times 200 \text{ pc} \sim 4 \times 10^{66} \text{ cm}^3, \tag{2.4}$$

where r_g and d_g are the radius and the thickness of the disk of the galaxy, respectively. As a result, the energy is estimated to be $L_{\rm cr} \sim 5 \times 10^{40}$ ergs s^{-1}.

Among galactic sources, supernova remnants are the most strong candidate for the cosmic ray acceleration on this point of view. Supernovae are thought to occur one event per

$\sim$30 yr, emitting kinetic energy of 10^{51} erg per each event. Therefore, if 10% of this kinetic energy is injected into the acceleration, the above required energy for the galactic cosmic ray acceleration can be fulfilled by SNRs.

2.1.4 Fermi Acceleration

Particles moving between two media which have different speeds can gain energy. By moving back and forth many times, even high energy can be attainable. When the speed difference is formed by an infinite plane shock of compression ratio 4, the energy spectrum of the accelerated particles is expected to be a power-law of index 2 (Bell 1978). Since this value is proper to explain the spectrum of the cosmic ray, the Fermi Acceleration mechanism has been widely accepted as a standard acceleration mechanism (see e.g., recent review by Malkov & Drury 2001). Acceleration time-scale is summarized in Appendix C.

2.2 Supernovae and Supernova Remnants

2.2.1 Supernovae and their Classification

The term *supernova* was coined by Baade & Zwicky (1934) to distinguish from the more ordinary novae those anomalously bright stellar outbursts which at maximum often outshine their entire parent galaxy. This phenomenon is now known to be an explosion of a star at the end of its evolutionary lifetime, and the explosion energy is as large as 10^{51} ergs.

Historically astronomers have recognized two types of supernova which are distinguished by their optical spectra. Figure 2.3 shows the basic classification scheme. The class of a supernova has traditionally depended on the spectrum near maximum light. Those without H line in their spectra are called Type I, and those with H line are called Type II.

Among the SN II, a further differentiation has been proposed based on the shape of the light curve. Those with a pronounced plateau have been termed Type II plateau (SN II-P), and those with a nearly linear decline in magnitude with time from peak are termed Type II linear (SN II-L). However, the recently exploded SN 1987A event falls neither of case. The light curve of SN 1987A was very different due to the blue compact nature of the progenitor, although it showed some similarity to Type II plateau on the exponential tail (see Dopita (1988); Arnett, Bahcall, Kirshner, & Woosley (1989), and references therein). In addition, SN 1987A has given a new spectral behavior. Traditional SN II-L and P events have shown a nearly pure continuum near maximum light, a week or two after the explosion. SN 1987A,

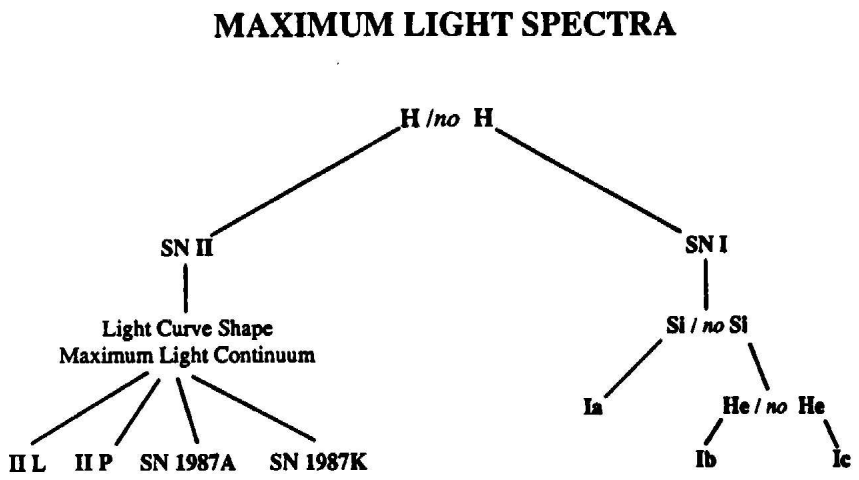

Figure 2.3: The basic classification scheme for supernovae based on spectral features at early times (Harkness & Wheeler, 1990).

in contrast, showed strong P Cygni features of the Balmer lines from the first day.

Type I supernovae should also divided into subclasses. The existence of two populations of Type I supernova precursors was evidenced by their occurrence throughout spiral and elliptical galaxies and their correlation with the rate of star formation. Firstly, it was found that a part of Type I SNe show no Si II absorption at $\lambda \sim 6150$ Å near maximum light in contrast to the "normal" Type I (Type Ia) events. Those peculiar Type I (Type Ib) events have common characteristics different from SN Ia. At maximum light, SN Ib tend to be weaker and redder than SN Ia, and they show stronger non-thermal radio emission than SN Ia. They occur in S galaxies and regions of star formation. The most clear difference between Type Ia and Ib show up 25 days or more after the explosion: lines of [Fe II] and [Fe III] dominate the spectra of Type Ia events, while lines of [O I] dominate those of Type Ib events (Gaskell et al., 1986). None of these distinctions is purely phenomenological, and they all bear on the specific physics of the situation. Thus the term SN I will hence be considered to be essentially meaningless unless it is further qualified as SN Ia and SN Ib.

Nowadays, the SN Ia is thought be an explosion of white dwarfs in binary systems with mass transfer. Material is added to the white dwarf until the core reaches a critical density 2×10^9 g cm^{-3}, resulting in an uncontrolled fusion of carbon and oxygen, thus detonating the white dwarf. The progenitors of SN Ib is thought to be massive stars that have lost all their hydrogen envelope. Wolf-Rayet stars, for example, are possible progenitors. SN II is an explosion of a massive star more than 10 $M_\odot$. The iron core produced after nuclear

fusion process along the evolution of the star grows so massive that the core cannot sustain the gravitation of itself. Then the core collapse and release the gravitational energy, which turns into a supernova.

2.2.2 Evolution of Supernova Remnant

A supernova remnant (SNR) is the aftermath of the explosion, which expands as a shell within the interstellar medium (ISM) for thousands of years. The evolution of an SNR can be divided into several phases.

Free Expansion Phase

The initial phase of evolution is characterized by the free expansion of ejected shell at a velocity $v_0 = (5 - 10) \times 10^3$ km s^{-1}, with essentially no deceleration. The deceleration of the shock front starts when the mass of swept-up matter becomes comparable to that of the ejected matter, which is the end of the first phase. The radius and age of the remnant at that point are

$$R_s = (3M_0/4\pi\mu m_{\rm H} n_0)^{1/3} = 1.9 \left(\frac{M_0}{1M_\odot}\right)^{1/3} \left(\frac{\mu}{1.36}\right)^{-1/3} \left(\frac{n_0}{1{\rm cm}^{-3}}\right)^{-1/3} \ {\rm pc}, \tag{2.5}$$

and

$$t \approx R_s v_0^{-1} \approx 190 \ {\rm yr}, \tag{2.6}$$

in a medium with mean ambient hydrogen density $n_0 = 1$ cm^{-3}, and with $M_0 = 1M_\odot$, $v_0 = 10^4$ km s^{-1}, and $\mu = 1.36$ (mean atomic weight of cosmic material per H atom). In this stage, almost all the initial explosion energy is manifested by kinetic energy of the ejected matter.

Sedov Phase (Adiabatic Phase)

The next phase of the SNR evolution is called an adiabatic phase. In this phase, the shock front is started to decelerate by encountering with the ambient interstellar matter. Shklovskii (1962) proved that the SN explosion within the interstellar matter can be likened to a point explosion in a gas with constant heat capacity. He also proved that the self-similar Sedov (1959) solution was applicable. At this stage, the evolution of the radius R_s and the velocity of the shock wave V_s, are described as,

$$R_s \ = \ 5.0 \left(\frac{E_0}{10^{51} \ {\rm ergs}}\right)^{1/5} \left(\frac{n_0}{1 \ {\rm cm}^{-3}}\right)^{-1/5} \left(\frac{t}{10^3 \ {\rm yr}}\right)^{2/5} \ {\rm pc}, \tag{2.7}$$

$$V_s \equiv \frac{dR_s}{dt} = \frac{2}{5}\frac{R_s}{t}, \tag{2.8}$$

where E_0, n_0, and t are the ambient density, initial explosion energy, and age, respectively. Numerical calculations by Chevalier (1974) showed that in this stage about 70% of the initial explosion energy has been transformed into thermal energy of the swept-up interstellar gas.

Radiative Cooling Phase

The remnant continues to expand adiabatically until the radiative cooling is important, when the gas temperature behind the shock front reaches the value that corresponds to the maximum on the radiative loss curve, $kT \sim (4-5) \times 10^5$ K. According to Falle (1981), the age t_{cool}, radius R_{cool}, and expansion velocity V_{cool} of an SNR entering into this radiative cooling stage are,

$$t_{cool} = 2.7 \times 10^4 \left(\frac{E_0}{10^{51}\ \mathrm{ergs}}\right)^{0.24} \left(\frac{n_0}{1\ \mathrm{cm}^{-3}}\right)^{-0.52}\ \mathrm{yr}, \tag{2.9}$$

$$R_{cool} = 20 \left(\frac{E_0}{10^{51}\ \mathrm{ergs}}\right)^{0.295} \left(\frac{n_0}{1\ \mathrm{cm}^{-3}}\right)^{-0.409}\ \mathrm{pc}, \tag{2.10}$$

$$V_{cool} = 277 \left(\frac{E_0}{10^{51}\ \mathrm{ergs}}\right)^{0.055} \left(\frac{n_0}{1\ \mathrm{cm}^{-3}}\right)^{0.111}\ \mathrm{km\ s}^{-1}. \tag{2.11}$$

2.2.3 Shock Wave

When the shell of an SNR speed exceeds the sound speed, a shock wave is formed, and the gas is heated. We here define up-stream and down-stream as Figure 2.4 on the coordinate in which the shock is at rest. There are physical properties between gases in the upstream and downstream of the shock wave. Conservation of mass, momentum, and energy across the shock front give Rankine-Hugoniot shock jump conditions, which can be expressed as:

$$\rho_1 v_1 = \rho_2 v_2 \tag{2.12}$$

$$\rho_1 v_1^2 + p_1 = \rho_2 v_2^2 + p_2 \tag{2.13}$$

$$\frac{1}{2}v_1^2 + h_1 = \frac{1}{2}v_2^2 + h_2 \tag{2.14}$$

where ρ, v, P,h are the density, velocity, pressure, and specific enthalpy of both upstream (subscript 1) and downstream (subscript 2), respectively. If the fluid can be assumed to be ideal gas, the third equation can be written as,

$$\frac{1}{2}v_1^2 + \frac{\gamma}{\gamma-1}\frac{p_1}{\rho_1} = \frac{1}{2}v_2^2 + \frac{\gamma}{\gamma-1}\frac{p_2}{\rho_2} \tag{2.15}$$

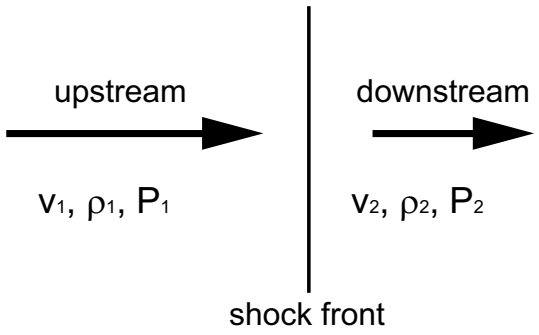

Figure 2.4: A schematic view around the shock front.

where γ is the specific-heat ratio. If we define sound speed (a_1) and the Mach number M_1 in the downstream as,

$$a_1 = \sqrt{\frac{\gamma p_1}{\rho_1}} \tag{2.16}$$

$$M_1 = \frac{v_1}{a_1}, \tag{2.17}$$

then the equations can be written as

$$\frac{\rho_1}{\rho_2} = \frac{v_1}{v_2} = \frac{(\gamma+1)M_1^2}{(\gamma-1)M_1^2+2} \tag{2.18}$$

$$\frac{p_2}{p_1} = \frac{2\gamma M_1^2-(\gamma-1)}{\gamma+1}. \tag{2.19}$$

With the equation of state,

$$\frac{T_2}{T_1} = \frac{p_2\rho_1}{p_1\rho_2} \tag{2.20}$$

$$= \frac{[2\gamma M_1^2-(\gamma-1)](\gamma-1)M_1^2+2]}{(\gamma+1)^2M_1^2} \tag{2.21}$$

When the shock is strong enough, or $M_1 \gg 1$, the density is compressed up to $(\gamma+1)/(\gamma-1) = 4$ ($\gamma = \frac{5}{3}$). In this case, the temperature in the downstream can also be written as

$$kT_2 = \frac{2(\gamma-1)}{(\gamma+1)^2}\mu v_1^2 = \frac{3}{16}\mu v_1^2 \tag{2.22}$$

where μ is the mean atomic weight and k is the Boltzmann constant. This is the post-shock temperature and is determined only by the up-stream velocity, or the shock speed. For example, when the shock velocity is 1000 km s^{-1}, $kT_2 = 1\times10^7$ K (= 1 keV). Since a plasma at this temperature emits strong X-rays, X-ray observations are strong tool to investigate the physics of supernova remnants.

2.2.4 Plasma Physics

Non-Equipartition

It has been debated whether electron and ion temperatures are quickly equilibrated by plasma processes behind collisionless high Mach number supernova shocks.

Electrons and ions (mainly protons) exchange energy through Coulomb interactions, which provide the minimum level of heating expected in the case of nonequipartition. The temperature varies as

$$\frac{dT_e}{dt} = 0.13\frac{T_p - T_e}{T_e^{3/2}} \tag{2.23}$$

(in cgs units; Spitzer 1978, p. 22).

2.2.5 Non-Equilibrium Ionization

The characteristic timescale for a plasma to reach collisional ionization equilibrium was derived by Masai (1994, 1984). The collisional ionization rate equation for an element of atomic number Z is written as

$$\frac{df_z}{d(n_e t)} = S_{z-1}f_{z-1} + (S_z + \alpha_z)f_z + \alpha_{z+1}f_{z+1} \tag{2.24}$$

where f_z is the ionic fraction of the element that is ionized $(z-1)$ times, and

$$\sum_{z=0}^{Z} f_z = 1, \tag{2.25}$$

and where S_z and α_z represent the rate coefficients for ionization and recombination from an ion of charge z to $z+1$ and $z-1$, respectively.

The ionization timescale (τ) to reach ionization equilibrium is estimated with the zero-th order approximation to be,

$$\begin{aligned} \tau = n_e t &\approx \sum_{z=0}^{Z}(S_z + \alpha_z)^{-1} && (2.26)\\ &\approx [(S_z + \alpha_z)_{\min|S_z - \alpha_z|}]^{-1} && (2.27)\\ &\approx 10^{12} \text{ s cm}^{-3}. && (2.28) \end{aligned}$$

It is notable that this time scale is nearly independent of both the element Z and the electron temperature T_e. Typically, as the electron density is 1 cm^{-3} in the interstellar medium, shock heated plasmas in young SNRs up to 10^4 yr old are expected to be in non-equilibrium ionization. In fact, underionized plasmas have been observed from many SNRs, such as Cassiopeia A and SN1006.

Heat Conduction

If the mean free path of electrons $\lambda_{\rm e} \approx 10^{18}(T_{\rm e}/10^7\ {\rm K})^2(n_{\rm e}/1\ {\rm cm}^{-3})^{-1}$ is much shorter than the scale length of the temperature gradient, $l_{\rm T} \equiv T/|\nabla T|$, the heat flux Q is given by,

$$Q = -\kappa|\nabla T|. \tag{2.29}$$

Here, κ is the thermal conductivity in a fully ionized hydrogen plasma,

$$\kappa = 1.31 n_{\rm e} k \lambda_{\rm e} \left(\frac{kT_{\rm e}}{m_{\rm e}}\right)^{1/2} \tag{2.30}$$

$$\simeq 2.6 \times 10^{11} \left(\frac{kT_1}{1.0\ {\rm keV}}\right)^{5/2} \left(\frac{\ln\ \Lambda}{32.2}\right)^{-1}\ {\rm ergs\ s^{-1}\ K^{-1}} \tag{2.31}$$

where for $T > 4.2 \times 10^5$ K the Coulomb logarithm is $\ln\ \Lambda = 29.7 + \ln\ n^{-1/2}(T_{\rm e}/10^6\ {\rm K})$.

2.2.6 X-ray emission from Supernova Remnants

In this section, we summarize X-ray emission mechanisms seen in supernova remnants. Distinguishing between these mechanisms is an important work in determining the physical properties (such as temperature, density, and energies of particles) of SNRs.

Bremsstrahlung (Free-Free) Emission

Radiation due to the acceleration of a charged particle in the Coulomb field of another charged particle is called *bremsstrahlung* or *free-free* emission.

The total emission from a medium with ion density n_i, electron density n_e and a fixed electron speed v is given by

$$\frac{dW}{d\nu dV dt} = \frac{32\pi^2 e^6}{3\sqrt{3}c^3 m^2 v} n_e n_i Z^2 g_{ff}(v,\nu) \tag{2.32}$$

where $g_{ff}(v,\nu)$, e, m, c, and Z are a Gaunt factor, charge unit, electron mass, light speed, and charge number of ion, respectively. Bremsstrahlung from a thermal plasma can be formalized by averaging the above single-speed expression over a thermal distribution of speeds. The emission power of the thermal bremsstrahlung is given as

$$\frac{dW}{d\nu dV dt} = 6.8 \times 10^{-38} Z^2 n_e n_i T_e^{-1/2} e^{-h\nu/kT_e} \bar{g}_{ff}\ ({\rm ergs\ sec^{-1}\ cm^{-3}\ Hz^{-1}}) \tag{2.33}$$

in CGS units, where $\bar{g}_{ff}$ is a frequency average of the velocity averaged Gaunt factor and k is the Boltzmann constant. $\bar{g}_{ff}$ is in the range 1.1 to 1.5.

Typical gas in an SNR is thermalized more than 10^6 K and H and He are totally ionized. As a result, *bremsstrahlung* is a major process of X-ray emission from an SNR.

Line Emission (Bound-Bound) Emission

The transitions between two discrete quantum levels are often accompanied by photon emissions, which are called line emission or *bound-bound* emission. Ionized plasma can be collisionaly excited by electrons and emits line emissions. Since the excited levels come very quickly, for the first approximation, we can assume that the rate of photon emission is the same as the excitation. Therefore, the line intensity is proportional to $n_e n_i$, which determines the probability of collisions between electrons and ions. We can derive relative abundances by comparing line intensities from different elements. Moreover, since emissivity of the continuum emission (bremsstrahlung) is proportional to $n_e n_{\rm H}$, by comparing the intensity of the line and continuum emission, the absolute abundance with respect to H can be derived.

A level of transition changes with a degree of ionization. Therefore, the energy of lines show the ionization level of that element . However, it is difficult to produce low ionized plasmas in a ground experiment energies and strengths of emission lines from low-ionized plasmas have been determined by interactive studies between astronomical observations and atomic theories.

Synchrotron Emission

Particles accelerated by a magnetic field will radiate. For extreme relativistic particles, this radiation is known as *synchrotron radiation*. The synchrotron radiation power per unit frequency from a single charged-particle of energy E $(= \gamma mc^2)$ in a magnetic field B is

$$P(\omega) = \frac{\sqrt{3}}{2\pi} \frac{q^3 B \sin\alpha}{mc^2} F\left(\frac{\omega}{\omega_c}\right), \tag{2.34}$$

where α is the pitch angle of the particle trajectory and $F(x)$ is a dimensionless function, which can be derived by integrating a modified Bessel function (Rybicki & Lightman 1979). The characteristic frequency ω_c is

$$\omega_c = \frac{3\gamma^2 qB \sin\alpha}{2mc}. \tag{2.35}$$

Since $F(x)$ peaks at $x \sim 0.29$, $P(\omega)$ has emission peak at $\sim 0.29\omega_c$. Therefore, for a relativistic electron of energy $E_{\rm e}$, the peak energy of emitted photon $E_{\rm p}$ is given as,

$$E_{\rm p} \sim 5.3 \left(\frac{B}{10\ \mu{\rm G}}\right) \left(\frac{E_{\rm e}}{100\ {\rm TeV}}\right)^2\ {\rm keV}. \tag{2.36}$$

where E_p is averaged over α. By integrating equation (2.34), the total emission power is given as

$$P_{tot} = \frac{2q^4 B^2 \gamma^2 \sin^2 \alpha}{3m^2 c^3}. \tag{2.37}$$

For synchrotron radiation emitted by electrons in a power-law distribution with index p over a sufficiently broad energy range, the spectrum is also power-law and the spectral index is

$$s = \frac{p-1}{2} \tag{2.38}$$

(Rybicki & Lightman 1979).

Inverse Compton

The scattering of a high-energy (nearly equal to or larger than the rest mass energy of an electron) photon by a low-energy free electron is called the Compton scattering, in which the photon partly loses its energy. Conversely, when an electron is relativistic and has sufficiently higher energy than a photon, the photon can gain energy by interacting with the electron. This process is called inverse Compton scattering. The energy transfer by a single collision averaged over the scattering angle is given as

$$E \simeq \gamma^2 E_0, \tag{2.39}$$

where E_0, E, and γ are the photon energies before and after the scattering, the Lorentz factor of the electron, respectively. The total power transfered from an electron to photons (radiation field) by the inverse Compton scattering is given as

$$P_{IC} = \frac{4}{3}\sigma_T c \gamma^2 \beta^2 U_{ph}, \tag{2.40}$$

where σ_T, U_{ph}, and β are cross section of Thomson scattering, energy density of the radiation field, and the particle speed in a unit of c (light speed). The difference between synchrotron emission and inverse Compton is the target against which an electron interact; the target of synchrotron emission is magnetic field and that of inverse Compton is radiation (photon) field. Ratio between the emission powers of synchrotron emission and inverse Compton is given only by

$$\frac{P_{sync}}{P_{IC}} = \frac{U_B}{U_{ph}}. \tag{2.41}$$

When the energy of the electron is high enough that the energy of photon in the electron rest frame (γE_0) is comparable or higher than the electron rest mass ($m_e c^2$), the cross section of Thomson scattering have to be modified using the Klein-Nishina cross section.

2.3 Other Diffuse X-ray Sources

2.3.1 Pulsar-wind nebula

Rotation-powered pulsars rotate very fast ($\sim$10 Hz) and have strong magnetic field $\sim 10^{12}$ G. The pulsar accelerate particles in thier magnetosphere, although the detailed acceleration region is still controversial between a polar cap region (e.g., Sturrock 1971) and an outer gap region (e.g., Cheng, Ho, & Ruderman 1986). A relativistic magnetized wind of accelerated particles injected by the pulsar is thermalized at a shock where the wind comes into pressure equilibrium with the surroundings, and creates a pulsar-wind nebula. Since a pulsar-wind nebula contains relativistic electrons, synchrotron emission is observed in wide spectral band: radio to γ-rays.

Since rotation-powered pulsars use their spinning energy into the radiation and the acceleration of particles, the spinning period P becomes gradually longer. Since the spinning power is given as:

$$E_{rot} = \frac{1}{2} I \omega^2 = 2\pi I P^{-2}, \tag{2.42}$$

where I is the moment of inertia of the neutron star, and ω is the angular frequency, the energy loss rate (or spin-down luminosity) is given as:

$$\frac{d}{dt} E_{rot} \equiv \dot{E}_{rot} = I\omega\dot{\omega} = 4\pi I \dot{P} P^{-3}. \tag{2.43}$$

Pulsars which have large spin-down luminosity are detected in the X-ray and gamma-ray bands. For example, the famous pulsar-wind nebulae, the Crab Nebula, with the X-ray luminosity $L_{\rm X} = 1 \times 10^{37}$ ergs s^{-1}, has a rotation-powered pulsar of spin-down luminosity $\dot{E}_{rot} = 5 \times 10^{38}$ ergs s^{-1} on its center. The relation between X-ray luminosity and spin-down luminosity of pulsars has been sought since Seward & Wang (1988) found a correlation of the form $L_{\rm X} \propto \dot{E}^{1.39}$.

2.3.2 Star-forming Regions

Star-forming regions can be roughly divided into two categories with their sizes: high-mass and low-mass star forming regions.

High-mass star formation is thought to occur in giant molecular clouds, which contain a mass of 10^5–3×10^6 M$_\odot$. High-mass star forming regions emit strong X-ray radiation with luminosities $\sim 10^{33}$–10^{34} erg s^{-1} and with temperatures of several keV, sometimes accompanying diffuse emission (e.g., Townsley et al. 2003). Since the size of those star-forming

regions are 0.1–50 pc, X-ray emissions are very similar to those from SNRs. Moreover, they may be enclosing even SNRs originating from rapidly evolved highly massive stars. High-mass star forming regions are also known as H II regions; massive stars ionize ambient dense media with strong ultra-violet radiation. Since H II regions radiate strong radio continuum, nowadays more than 1000 H II regions are known (e.g., Paladini et al. 2003). Therefore, an X-ray emitting high-mass star forming regions which is not identified as an H II regions is quite unlikely.

In smaller molecular clouds, which are generally called "dark clouds" having a mass about 1/1000–1/100 of giant molecular clouds, only low-mass stars are formed. These regions also emit X-ray emission with luminosity $\sim 10^{32}$ erg s^{-1}. Since those regions do not contain high-mass stars, they are not accompanied by H II regions. Therefore, if they are deeply embedded in the galactic plane and deeply absorbed, they may escape radio surveys. However, the size of the star-forming region is relatively small (1–2 pc), they would be easily distinguished from SNRs.

2.3.3 Cluster of Galaxies

Clusters of galaxies are gravitationally bound systems containing typically hundreds of galaxies in a region about 10^6 pc in size. Clusters of Galaxies are bright X-ray sources with luminosities of 10^{43-45} ergs s^{-1}, and the emission mechanism is thermal bremsstrahlung from hot ($\sim 10^8$ K), low density ($\sim 10^{-3}$ atoms cm^{-3}) gas. X-ray observations of clusters of galaxies have provided size of the total mass and about 80–90% of the mass in clusters of galaxies are known to be dark matter. Since the gas is gravitationally bounded, the structure seen in the X-ray band is center-filled morphology.

When we see clusters of galaxies located behind the Galactic plane, we can only observe their hard X-ray emission due to the deep interstellar absorption. Therefore, we expect to find only high-temperature ($\geq$ 2 keV) clusters. Moreover, the positive correlation between X-ray luminosities and temperatures are known for clusters, we can expect to observe only clusters of large luminosities ($\geq 10^{44}$ ergs s^{-1}). A deeply absorbed cluster of galaxies located behind the Galactic plane is reported by Nevalainen et al. (2001). The temperature and luminosity of the cluster are $\sim$ 6 keV and $\sim 4 \times 10^{44}$ erg s^{-1}, respectively.

Chapter 3

Instruments

3.1 *ASCA*

ASCA is a Japanese fourth X-ray satellite launched on February 20th, 1993. *ASCA* has four identical X-ray telescopes with nested thin foil mirrors (XRT; Serlemitsos et al. 1995). The focal-plane instruments consist of two kinds of detectors: two CCD cameras, and two gas counters. The former are called Solid-state Imaging Spectrometers (SISs: Burke et al. 1994), which are good in energy resolution. The latter are called two Gas Imaging Spectrometers (GISs: Ohashi et al. 1996; Makishima et al. 1996), which realized large field of view. In the following sections, the above XRT, GIS, and SIS are described respectively.

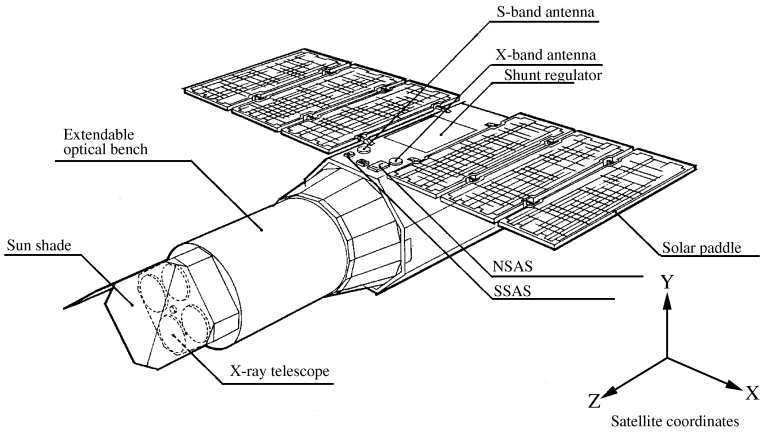

Figure 3.1: The schematic view of the *ASCA* satellite.

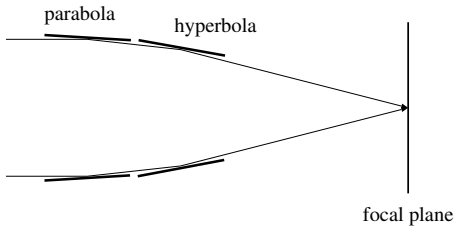

Figure 3.2: The schematic view of the Wolter type-I configuration.

3.1.1 XRT (X-Ray Telescope)

The XRT mirrors of *ASCA* utilize total X-ray reflection under the Wolter type I configuration, which employs paraboloid and hyperboloid surfaces as the primary and the secondary mirrors (Figure 3.2).

Usually, the effective area of an X-ray mirror is increased by nesting multiple reflective surfaces, because the critical angle for the total X-ray reflection is very small. Moreover, the critical angle gets smaller for X-ray photons of higher energy. The *ASCA* XRT has realized a drastically large number of nestings by utilizing 120 thin aluminum foils (127 μm thick). Thus, the XRT had a large effective area even at 5$\sim$10 keV; however, the angular resolution was so poor as 2$\sim$3 arcmin due to the shape errors of the mirror surfaces. In fact, since such a thin foil is very difficult to shape into a paraboloid or hyperboloid, a conical surface was instead used as an approximation, which degraded the imaging quality. Although surface of the aluminum foils was coated with lacquer to increase the surface smoothness, the residual surface waviness added to the image degradation. Design parameters and performance of the XRT are summarized in table 3.1.

3.1.2 GIS

GIS (Gas Imaging Spectrometer) is a gas scintillation proportional counter with imaging capability (Ohashi et al. 1996; Makishima et al. 1996). The energy resolution was $\sim$ 8% at 6 keV, which was almost the highest value ever achieved with a gas counter. The GIS had a very low detector background, since charged particles and X-rays could be strongly discriminated by the "rise time discrimination". The design parameters and performance of the GIS are summarized in Table 3.2.

Table 3.1: Design parameters and performance of the *ASCA* XRT

Mirror substrate	Aluminum foil (127 μm)
Mirror surface	Acrylic Lacquer (10 μm) + Au (50 μm)
Mirror length	100 mm
Inner / outer diameter	120 mm / 345 mm
Focal length	3500 mm
Incident angle	$0.24^\circ - 0.7^\circ$
Total weight of four XRTs	$\sim$ 40 kg
Geometrical area	558 cm^2 / telescope
Field of view	$\sim 24'$(FVWM at 1 keV)
	$\sim 16'$(FVWM at 7 keV)

Table 3.2: Design parameters and performance of the GIS

Bandpass	0.7–15 keV
Energy Resolution	8% at 5.9 keV (FWHM)
Effective Area	50 mm ($50'$) diameter
Entrance Window	10 μm beryllium
Absorption material	Xe (96%) + He (4%), 10 mm depth, 1.2 atm at 0°C
Positional Resolution	0.5 mm ($0.'5$; FWHM)
Minimum Time Resolution	$\sim$ 61 μs (in PH Mode)

Structure of GIS and the X-ray detection

Two identical detectors (named GIS-2 and GIS-3) are mounted on the focal plane of XRT. The structure of the GIS is shown in Figure 3.3, where the left side corresponds to the top while the right to the bottom along the z-axis of the satellite coordinates in Figure 3.1. Each GIS consists of a gas cell, a position-sensitive phototube, and high voltage suppliers. The X-rays from the XRT are detected by the 25 mm-depth gas cell, which is filled with 96% of Xe and 4% of He to 1.20 atm pressure (at 0°C). The gas is sealed by a beryllium foil of a 10 μm thickness and a 52 mm diameter, supported by a stainless grid and fine mesh. The gas cell is divided into two regions by the intermediate mesh: the drift region and the following scintillation region. Each region is biased by 1 kV cm^{-1} and 4 kV cm^{-1} electric fields.

The principle of the X-ray detection by the GIS is shown in Figure 3.4. First, an X-ray

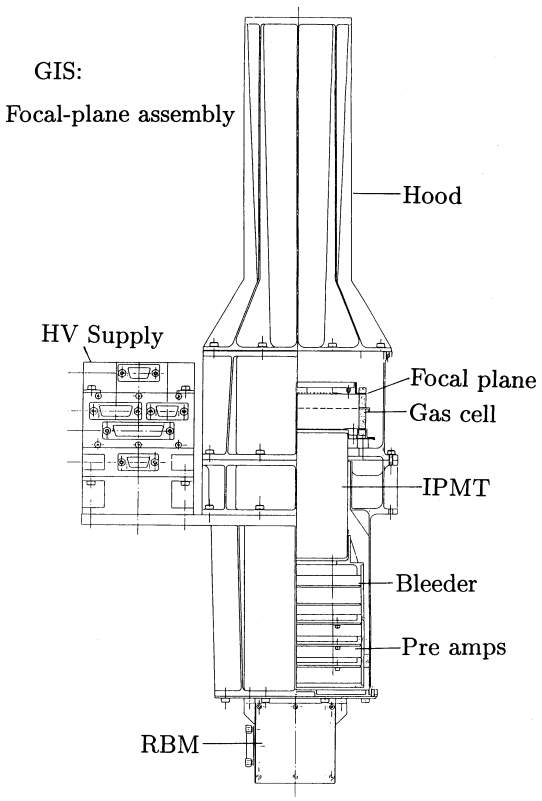

Figure 3.3: Cross section view of the GIS sensor.

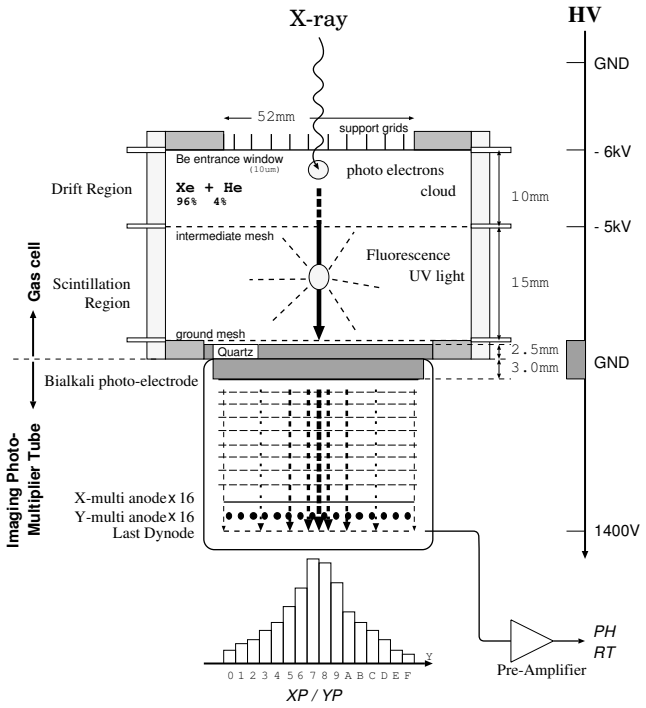

Figure 3.4: Schematic diagram of the principle of the GIS detector.

photon is photo-absorbed in the drift region and creates free electrons. These electrons drift toward the intermediate mesh guided by the electric field, then accelerated by the stronger field in the scintillation region. These accelerated electrons repeatedly excite xenon atoms, which produce a large number of scintillation UV photons. These UV photons are finally collected by the imaging photo-multiplier tube attached beneath the gas cell. The energy information is obtained from the final dynode signal. As the multiplication does not use avalanche like gas proportional counters, higher energy resolution ($\sim$8% at 6 keV) could be achieved.

Background Rejection and Data Screening

When X-rays are properly absorbed in the drift region, the signal should exhibit a rise time of about 3 μs which corresponds to the drift time of elections in the scintillation region. If a charged particle enters the gas-cell of the GIS detector, it creates a long track in the drift region and the resultant signal exhibits a long rise time. With these discriminations, 99% of non-X-ray backgrounds are eliminated and the residual non-X-ray backgrounds in the 17$'$

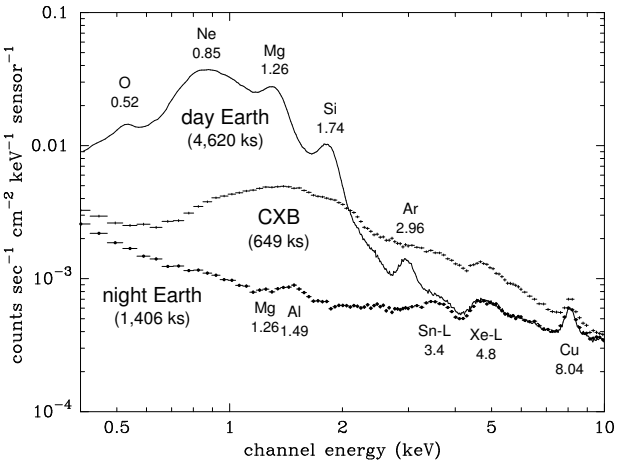

Figure 3.5: GIS spectra of day earth, blank sky, and night earth from Ishisaki (1997).

radius from the detector center is achieved to be 5×10^{-4} cts s^{-1} cm^{-2} keV^{-1}. In Figure 3.5, the GIS spectra of day earth, blank sky and night earth are displayed. The night earth data are thought to represent the non-X-ray events.

The characteristics of the RNXB have been investigated by using data from night-earth observations (Ishisaki 1997):

1. The total counting rate of the RNXB is gradually increasing by about 8% per year.
2. The intensity of the RNXB depends on the position of the satellite in orbit and can be reproduced as a function of the geomagnetic cut-off rigidity (COR) and H02 counts (GIS monitoring counts: G2_H0+G2_H2+G3_H0+G3_H2).
3. There are some geographical points in orbit where the intensity of the RNXB becomes anomalously high. At those points, RMB counts are founded to be high. RBM is a radiation belt monitor equipped to GIS2. Therefore, these are defined as "flare- events" and interpreted as a phenomenon associated with a local geomagnetic anomaly.

To reject the "flare-events", the screening procedure, called "flare-cut", using H02 counts and RBM counts (RBM_CONT) as parameters was introduced (Ishisaki 1997). The screening conditions of the flare-cut are summarized in Table 3.3.

3.1.3 SIS

The SIS (Burke et al. 1994) is the first satellite-bourne X-ray experiment that utilizes CCDs in the photon counting mode. Design parameters and performance of the SIS are summarized in Table 3.4. The main characteristics is its high energy resolution realized simultaneously

Table 3.3: The selection criteria for GIS data.

SAA	Excluded
GIS_RBMF	Excluded
COR	> 4 (GV)
ANG_DIST	$> 0\&\&< 0.01$
ELV	$>10^\circ$
SFR	Excluded
HFR	Excluded

SAA : South Atlantic Anomaly passage
COR : CutOff Rigidity
ANG_DIST : ANGular DISTribution
ELV : ELeVation from the rim of the earth
SFR : Soft Flare Region
(RMB_CONT < 100 && G2_H0+G2_H2+G3_H0+G3_H2<=45)
HFR : Hard Flare Region
(G2_H0+G2_H2+G3_H0+G3_H2<=0.45×COR^2 − 13×COR+125)

with the imaging capability. One of the short points is the narrow field of view. Because of the degradation by cosmic ray bombardment in orbit, only a part of the CCDs is operated in each observation after several years after launch. Therefore, the SIS is not suited for our survey and study of extended SNRs. The knowledge about the X-ray CCD in space obtained with the SIS experiment is taken over by the CCD instruments on *Chandra* and *XMM-Newton*.

Table 3.4: Design parameters and performance of the SIS

Illumination Method	Front Illumination
Number of Pixels (1 chip)	420 ×420
Pixel Size	27 μm
Area (1 chip)	11×11 mm square
Field of View (1 chip)	11×11 mm square
Thickness of Depletion Layer	$\sim 40\mu$m
Bandpass	0.4–12 keV
Quantum Efficiency	$\sim 80\%$ at 5.9 keV
Energy Resolution	2% at 5.9 keV (FWHM)

3.2 *XMM-Newton*

XMM-Newton is a ESA's X-ray observatory launched on December 10th, 1999. It carries two distinct types of telescopes: three X-ray telescopes with different X-ray detectors in their foci, and a 30-cm optical/UV telescope with a microchannel-plate pre-amplified CCD detector in its focal plane.

XMM-Newton provides the following three types of scientific instruments: three X-ray CCD cameras called European Photon Imaging Camera (EPIC), two high-resolution X-ray spectroscopy instruments called the Reflection Grating Spectrometer (RGS), and the Optical Monitor (OM). Three EPIC cameras consist of two different detectors; two MOS cameras and one pn. They provide X-ray imaging, moderate resolution spectroscopy, and X-ray photometry, and suit for our study of supernova remnants. Since we mainly used the EPIC cameras, characteristics of them and the associated X-ray telescopes are described below.

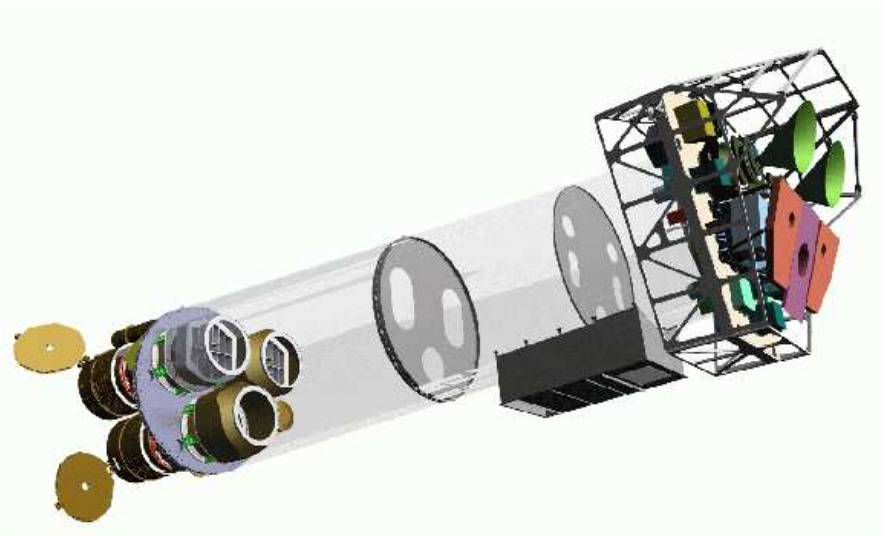

Figure 3.6: Sketch of the *XMM-Newton* payload. The three X-ray mirror modules are visible at the lower left. At the right end of the assembly, the focal X-ray instruments are shown: the EPIC-MOS cameras with their radiators, the radiator of the EPIC-pn camera and those of the RGS detectors. The OM telescope is obscured by the lower mirror module.

3.2.1 X-ray Telescopes

Design Structure

XMM-Newton's three X-ray telescopes are co-aligned with a relative astrometry between the three EPIC cameras calibrated to better than 1–2″ across the full FOV. One telescope has a light path simply illuminating the focal plane detector, the pn camera. On the other hand, two others have grating assemblies in their light paths and part of the incoming radiation is diffracted onto their secondary foci where RGSs are located. 44% of the incoming light is directed onto the MOS cameras at the prime foci, while 40% of the radiation is dispersed onto a linear CCD strips of RGSs. The remaining light is absorbed by the support structures of the grating assemblies.

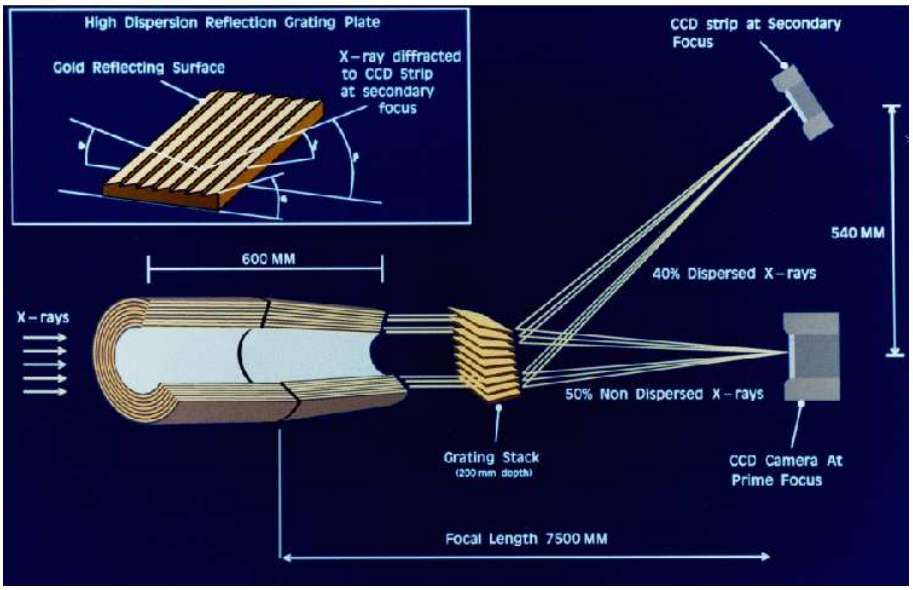

Figure 3.7: The light path of the two *XMM-Newton* telescopes with grating assemblies (not to scale). Note that the actual fraction of the non-intercepted light that passes to the primary MOS focus is 44%, while 40% of the incident light is intercepted by grating plates.

Mirror Characteristics

The PSF depends on the source off-axis angle (e.g., the PSF at large off-axis angles is elongated due to the off-axis aberration), and slightly depends on the source azimuth within the FOV. Values for the half energy width (HEW) of the PSFs on-axes are 13.8″, 13.0″, and 15.2″ for the MOS1, MOS2, and pn telescopes, respectively. These values are about ten times smaller than those of the ASCA telescopes.

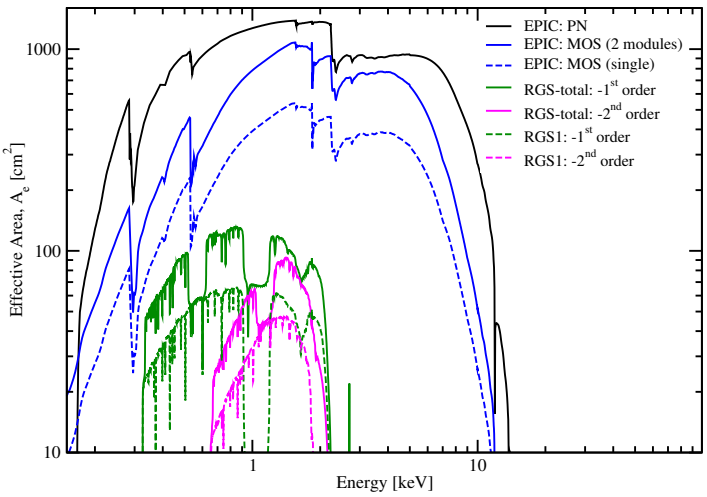

Figure 3.8: The on-axis effective areas of the *XMM-Newton* telescopes, combined with the quantum efficiency of the focal X-ray instruments, EPIC and RGS.

Figure 3.8 shows both the on-axis and off-axis effective areas of the *XMM-Newton* telescopes. The XMM-Newton mirrors are most efficient in the energy range from 0.1 to 10 keV, with a maximum at about 5 keV and a pronounced edge near 2 keV (Au M edge). The effective area of each MOS camera is smaller than that of the pn camera, because only part of the incoming radiation falls onto those detectors as described above. The effective areas decreases with increasing off-axis angle due to the vignetting effect. The off-axis vignetting in the two telescopes with the grating assemblies (and associated with the MOS cameras) has a dependence also with the azimuth angle. A source at an off-axis position perpendicular to the dispersion direction will be vignetted by a different amount to one at a position parallel to the dispersion direction. This dependency is shown in Figure 3.9.

X-ray stray light in the EPIC is produced by rays which are singly reflected by the mirror hyperbola and which reach the sensitive area of the camera. Thus, and X-ray baffle was implemented to shadow those singly reflected rays.

3.2.2 EPIC Cameras

EPIC cameras are X-ray imagers, consists of two MOS (Metal Oxide Semi-conductor) CCD arrays (Turner et al. 2001) and one CCD camera called pn (Strüder et al. 2001). All EPIC cameras are operated in a photon counting mode with a fixed frame-readout frequency, producing event lists. This allows for simultaneous imaging and non-dispersive spectroscopy

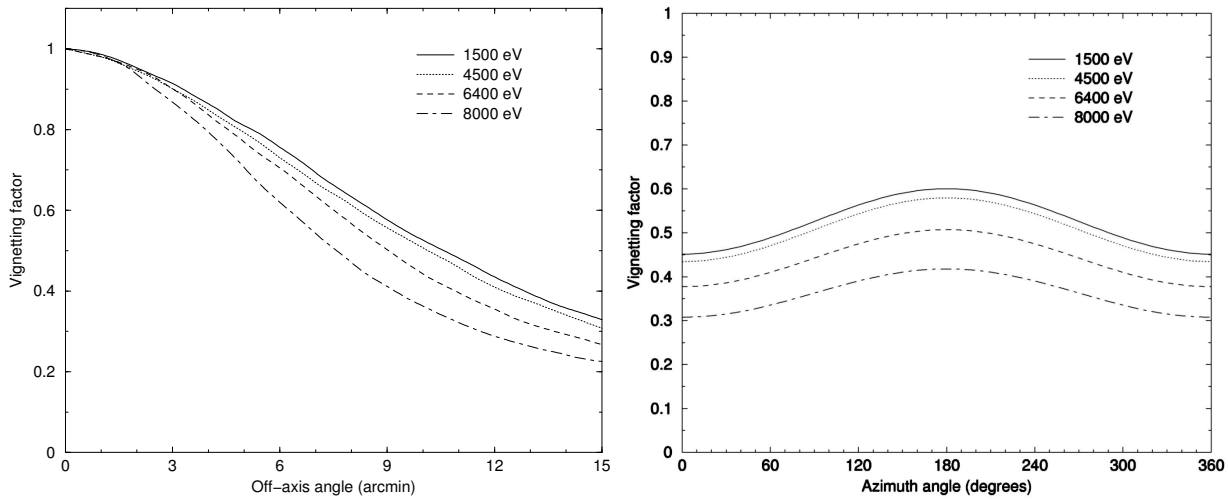

Figure 3.9: (left): The vignetting factor as a function of off-axis angle at a few selected energies, of the X-ray telescope in front of the pn camera. (right): Vignetting effect as a function of azimuth angle of the X-ray telescope in front of the MOS1 camera. The curves are given for an off-axis angle of 10 arcmin. Due to the presence of grating assemblies in the beams of the X-ray telescopes, the vignetting functions measured in the MOS cameras are modulated azimuthally.

due to the intrinsic energy resolution of the pixels.

Design Structure of EPIC MOS and pn

Each of the MOS cameras consists of 7 individual front-illuminated chip. The central CCD is at the focal point on the optical axis of the telescope while the outer six are stepped towards the mirror by 4.5 mm to follow approximately the focal plane curvature, and improve the focus for off-axis sources. Each chip is equipped with a frame store region. Two MOS cameras are rotated by 90° with respect to each other, in order to compensate for the dead spaces between the chips.

The pn-CCD, developed by MPE, consists of 12 back-illuminated CCD chips. The main characteristics of the pn-CCD is thick depletion layer of 300 μm. This realizes high quantum efficiency for the high energy X-ray photons. Each pixel column of pn chips has its own readout node; 64 channels per chip and a total of 768 channels for the entire camera. This allows much faster readout of the pn camera than the MOS cameras.

In Table 3.5, we show several design parameters and the performance of the EPIC

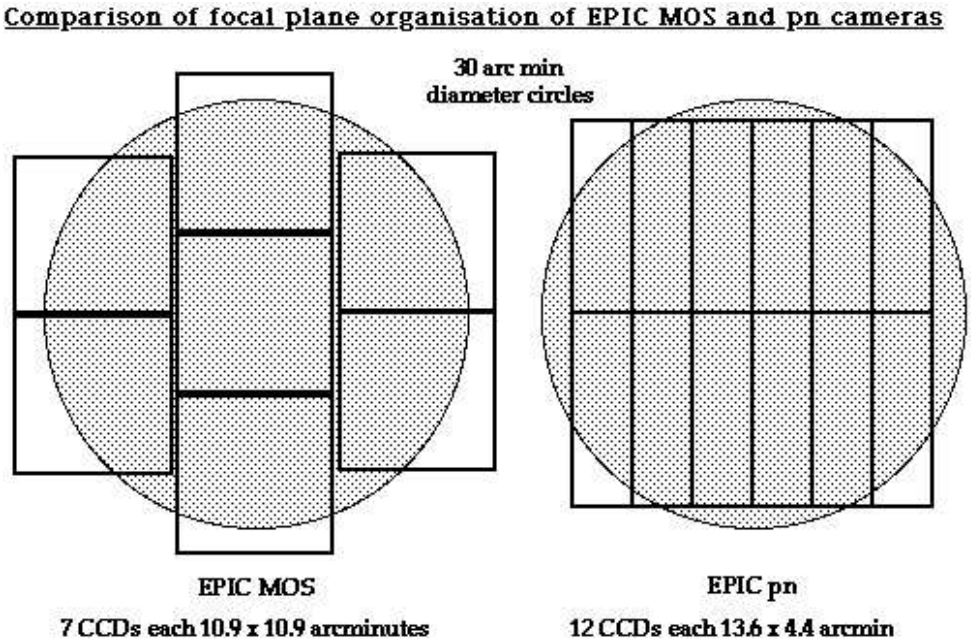

Figure 3.10: A sketch of the FOV of the two types of EPIC cameras; MOS (left) and pn (right). The shaded circles depict 30′ diameter areas.

Table 3.5: Design parameters and performance of the EPIC MOS and pn

	EPIC-MOS	EPIC-pn
Illumination Method	Front illuminated	Back illuminated
Number of Pixels (1 chip)	600 × 600	378 × 64
Pixel Size	40 μm (1.″1) square	150 μm (4.″1) square
Area (1 chip)	10.′9 × 10.′9	13.′6 × 4.′4
Field of View	$\sim$ 30′ diameter	$\sim$ 30′ diameter
Thickness of Depletion Layer	35–40 μm	300 μm
Time Resolution	2.6 s (Full Frame)	73.4 ms (Full Frame)
Bandpass	0.15–12 keV	0.15–15 keV

cameras with “full frame” mode, which we used in this thesis, while the EPIC cameras allow several other modes of data acquisition.

3.2.3 EPIC background

XMM-Newton takes an highly elliptical orbit with an apogee of about 115,000 km and a perigee of about 6000 km and thus mostly fly outside of the Earth's magnetosphere. This is thought to be responsible for the violent variability of the background of EPIC cameras as large as two orders of magnitudes. This variation is caused by protons scattered through the mirror system.

The background of the EPIC cameras consists of mainly two components: the cosmic X-ray background and the instrumental background. The latter component is mainly due to the interactions of charged paticles with the structure surrounding the detectors and the detectors themselves. This component can be further divided into 2 components: a transient component and quiescent component. Since spatial and temporal characteristics are different between these components, it is important to study them separately.

The transient component is thought to be induced by soft protons with energies less than a few 100 keV. Since the soft protons are scattered through the mirror system, they are vignetted. The spectra of soft proton flares are variable and no clear correlation has been found betweeen intensity and spectral shape. Therefore, observation intervals affected by this component have to be screened off.

The quiescent component is induced by high energy cosmic rays with energies larger than some 100 MeV which penetrate the satellite. As the spectrum in Figure 3.11 shows, the quiescent background consists of a continuum component and lines. While the continumm component is induced by high energy particles directly in the detector, the lines correspond to the florescent lines induced by cosmic rays interacting the surrounding structures. Whereas the continuum component is spatially flat, the intensities of the lines spatially change depending on the detector structure. Figure 3.12 show images of MOS camera in energy bands centered around Al-K and Si-K emission. The outer 6 of 7 CCDs detect more Al K radiation due to their closer proximity to the Al camera housing. Si K emission, however, is concentrated along the edges of some CCDs. This is attributed to detection of Si K X-rays escaping from the back substrate of a neighbouring CCD placed slightly forward and overlapping the subject chip.

3.3 *Chandra*

The *Chandra* X-Ray Observatory, which was successfully put into its orbit in July 1999 with Space Shuttle Columbia, is an astronomical X-ray satellite managed by NASA and Chandra

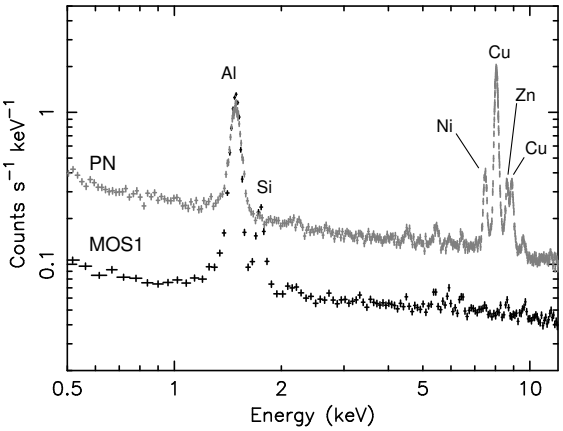

Figure 3.11: Background spectra for the PN (grey) and MOS1 (black) cameras during observations with the filter wheel in the CLOSED position. Names of elements are shown near the corresponding prominent K-fluorescence lines.

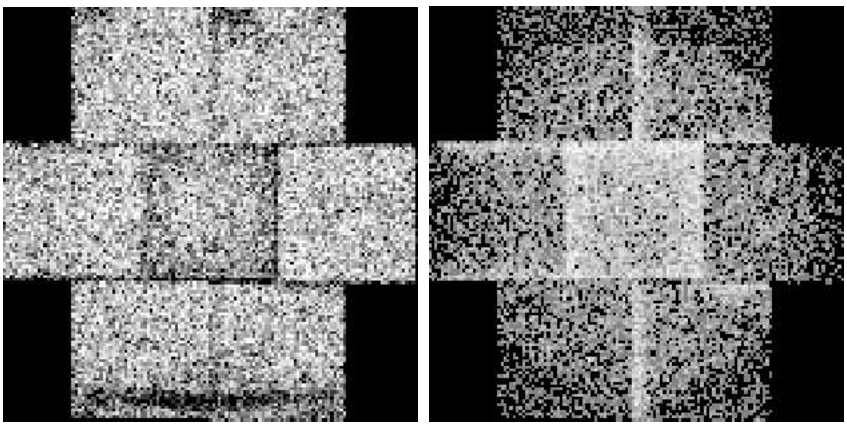

Figure 3.12: Images of Al-K (*left*) and Si-K (*right*) fluorescent emissions from the MOS camera Lumb, Warwick, Page, & De Luca (2002).

X-ray Center.

Chandra's main feature is its high spatial resolution of $\sim 0.5''$, which can be ascribed to the X-ray telescope called High Resolution Mirror Assembly (HRMA). For the focal plane instrument, we can choose one of two kinds of X-ray detectors: the Advanced CCD Imaging spectrometer (ACIS) and the High Resolution Camera (HRC). HRC is a multiple-channel plate type detector optimized for imaging and is without ability of spectroscopy. Since we used only ACIS in this thesis, HRMA and ACIS are described further below.

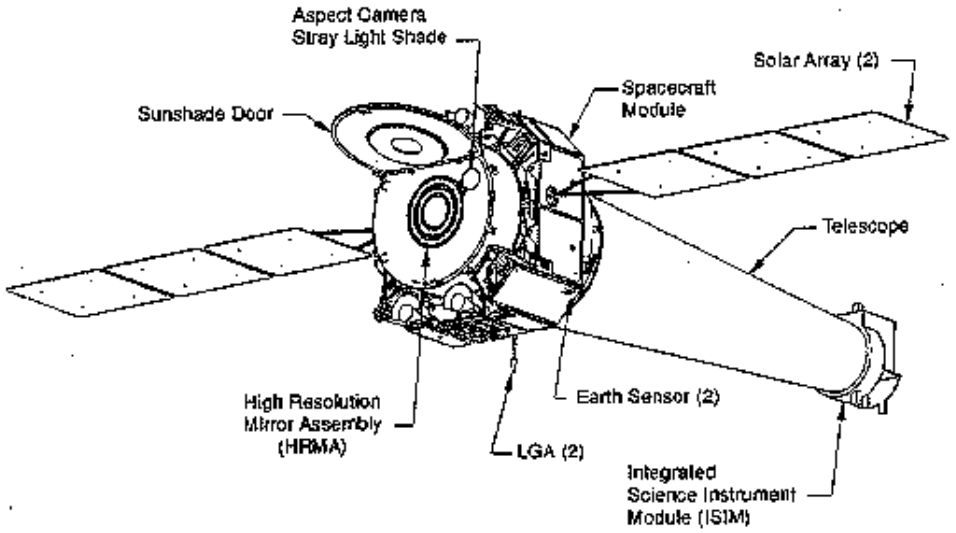

Figure 3.13: Schematic view of the *Chandra* satellite.

3.3.1 HRMA

Just as the telescopes of *ASCA* and *XMM-Newton*, HRMA also utlizes total X-ray reflection under the Wolter type-I configuration. HRMA consists of 4 pairs of concentric thin-walled paraboloid and hyperboloid mirrors, with the focal length of $\sim$ 10 m and the largest mirror having a diameter of $\sim$ 1.2 m. Those eight mirrors were fabricated from Zerodur glass, polished, and coated with iridium on a binding layer of chromium. In order to keep high accuracy of the mirror surface, the glass is very thick and heavy with the total mass of $\sim$ 1500 kg.

Figure 3.14 (left) shows the HRMA effective area as a funciton of X-ray energy in log-log scale, as well as the HRMA/ACIS and HRMA/HRC effective areas. The effective area also decreases as source position departs from on axis (Figure 3.14 (right))

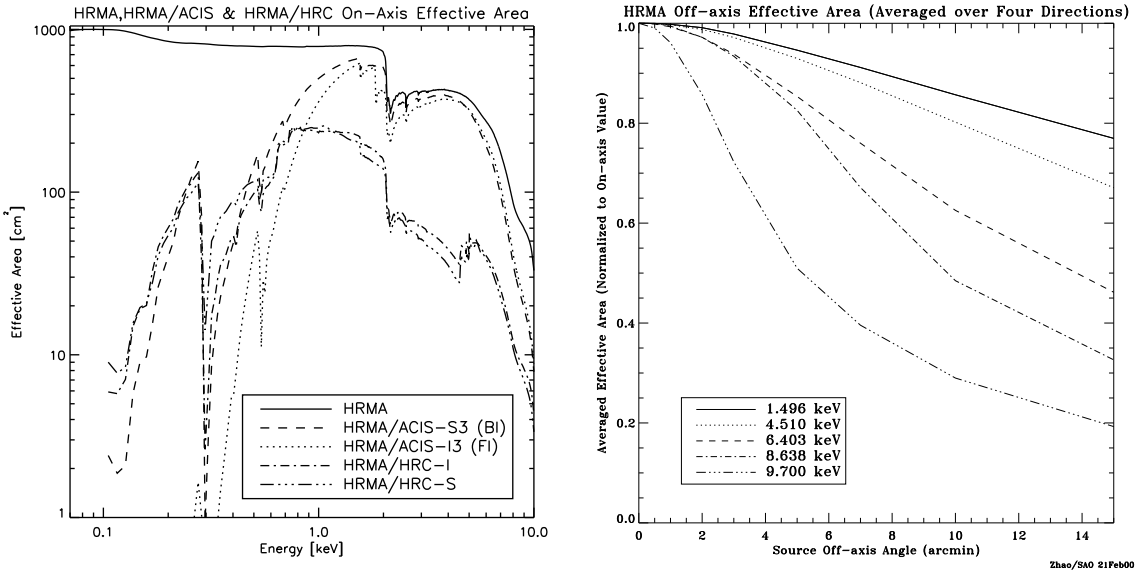

Figure 3.14: (left):On-axis effective areas of HRMA as a function of X-ray energy. (right):Off-axis effective areas of HRMA in several X-ray energies.

The point-spread function is so sharp that most of parallel X-ray photons are focused into a circle of $\sim 1''$ radius on a detector. The encircled energy function of HRMA is shown in Figure 3.15. On axis, 50% photons are included in a radius of $\sim 0''.35$ for 4.51 keV X-rays. The focus blurrs as the distance from the on axis point becomes large (Figure 3.15 (right)).

3.3.2 ACIS

The ACIS array, developed by the Pennsylvania State University, consists of ten CCDs, which are divided into two parts; ACIS-I with 2×2 CCDs and ACIS-S with 1×6 CCDs. The former is mainly used for imaging-spectroscopy, whereas the latter are for grating spectroscopy. ACIS-S1 and ACIS-S3 are back-illuminated CCDs, whereas all the other CCDs are front-illuminated CCDs.

Figure 3.17 (left) shows the energy resolution of ACIS estimated by ground calibrations. The FI chips have a good resolution near the theoretical limit ($\sim$ 120 eV at 5.9 keV), whereas that of the BI chips is slightly poor. After the launch, however, the ACIS-I chips were significantly by low energy protons encountered during radiation belt passages. The protons made many charge traps at buried channels, which cause the increase of charge transfer inefficiency (CTI). Since the gate structure of the BI chips are at opposite side to HRMA, the energy resolution of the BI chips remains at their pre-launch values. In the present

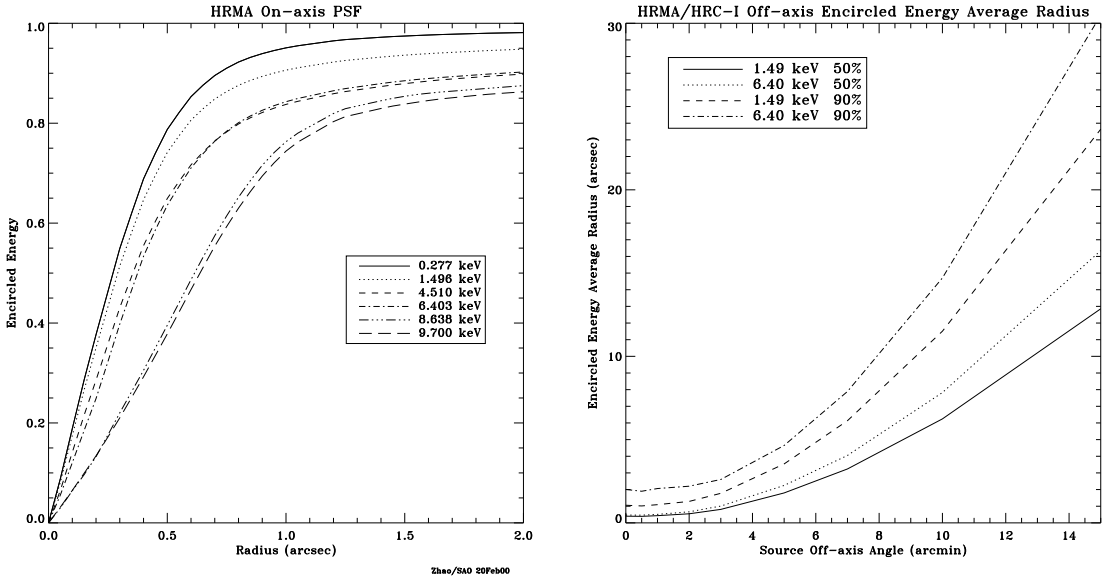

Figure 3.15: (left):On-axis effective areas of HRMA as a function of X-ray energy. (right):Off-axis effective areas of HRMA in several X-ray energies.

operation, ACIS is not left at the focal position during the radiation belt passages, hence no further degradation of CTI is expected. Furthermore, in order to reduce the effect CTI, the CCD temperature is lowered from $-90°$C to $-120°$C.

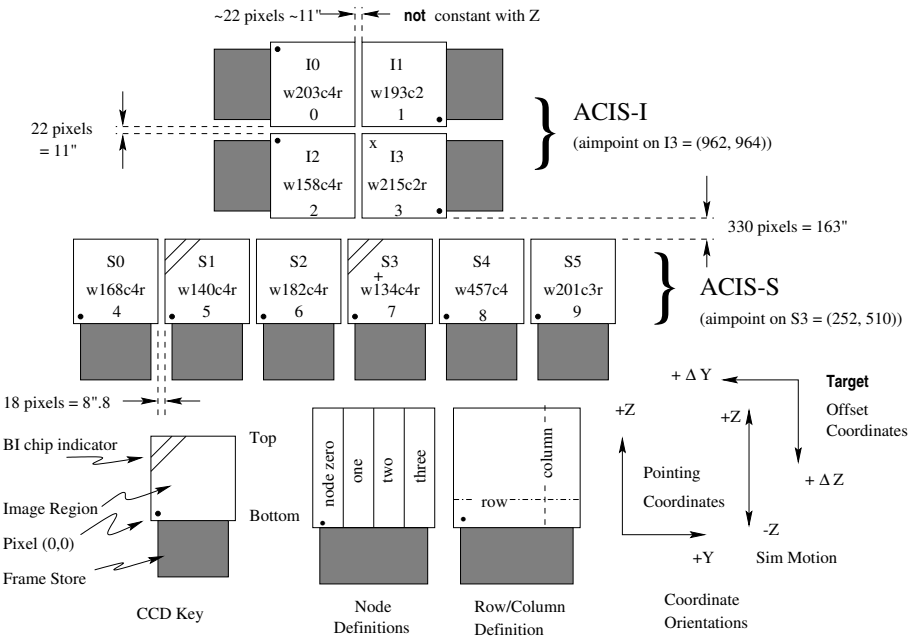

Figure 3.16: A schematic drawing of the ACIS-array configuration.

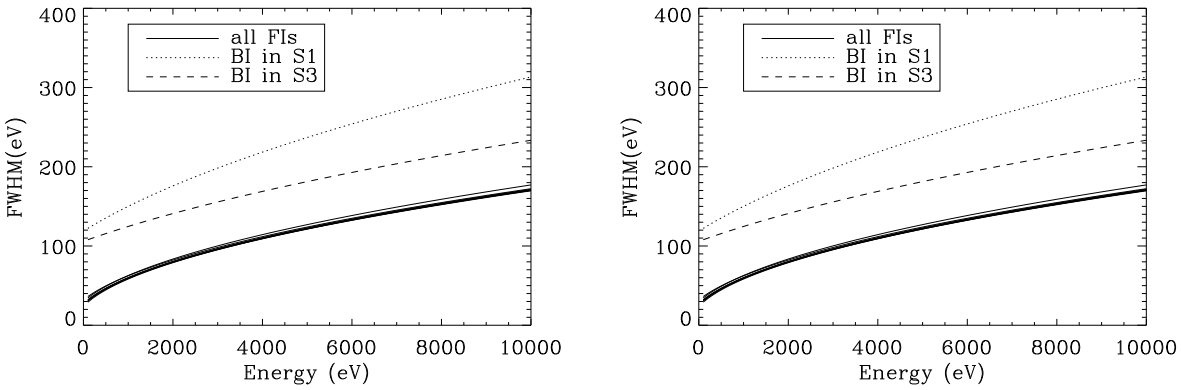

Figure 3.17: (left): The pre-launch energy resolution of ACIS. (right): The energy resolution of chip S3 and I3 as a function of row number, after the proton damage on orbit. The data were taken at the CCD temperature of $-120°$C.

Chapter 4

X-ray Observations of SNRs Discovered with *ROSAT*

The *ROSAT* All-Sky Survey (RASS) was mainly performed from 1990 to 1991 during the first phase of the satellite lifetime with the Position Sensitive Proportional Counter (PSPC; Pfeffermann et al. 1987). From the RASS data, SNRs listed in Table 4.1 have been discovered. From the fact that they escaped radio surveys it is inferred that they are relatively radio faint. Since the sensitive energy band of the PSPC was restricted to low energy band (< 2 keV) and the energy resolution was low (the PSPC is proportional counters), follow-up observations with X-ray satellites with wider energy band and higher energy resolution are required to reveal physical properties of the SNRs. RX J1713.7−3946 and G266.2−1.2 were later found to emit synchrotron X-ray with *ASCA* (Koyama et al., 1997; Slane et al., 1999), and the results were confirmed with higher spatial resolution of *Chandra* or *XMM-Newton* (Uchiyama, Aharonian, & Takahashi, 2003; Lazendic et al., 2004a; Iyudin et al., 2004).

Among the $\sim$ 250 known SNRs, non-thermal X-ray emission has been detected from 9 SNRs in total. Up to three of them are SNRs discovered with RASS, and the number is large in comparison with the total number of SNRs discovered in the RASS.

In order to study the characteristics of these SNRs, we analyzed data of both proposed observations and archival data. Since G266.2−1.2 and G347.3−0.5 are extensively studied and many papers have been published, we cite the literature. Since G13.3−1.3, G28.8+1.5, and G32.1−0.9 are large and faint, follow-up observations have not been done much. After the report of the ASCA observations by Yamauchi et al. (1999) and Tomida (1999), other parts of G156.2−0.5 were observed with *ASCA* and follow-up observations with *XMM-Newton* were also performed. We report here results of these observations. G272.2−3.2

and G299.2−2.9 were observed with *XMM-Newton*. Using the high spatial resolution and the good statistics, the physical conditions of the plasmas, existence of non-thermal X-ray emission, and the reason for the faintness in radio band were studied.

Table 4.1: SNRs discovered with RASS and follow-up observations

Name	Coordinate (R.A., Dec.)$_{J2000}$	Diameter (arcmin)	Radio Flux (Jy)	ASCA	XMM	Chandra
G13.3−1.3	($18^h19^m20^s$, $-18°00'$)	50	?	no obs.	–	no obs.
G28.8+1.5	($18^h39^m00^s$, $-02°55'$)	100?	?	no obs.	no obs.	no obs.
G32.1−0.9	($18^h53^m10^s$, $-01°08'$)	40?	?	[1]	no obs.	no obs.
G156.2+5.7	($04^h58^m40^s$, $+51°50'$)	110	5	[2],[3]	this work	no obs.
G266.2−1.2	($08^h52^m00^s$, $-46°20'$)	120	50?	[4]	[5]	–
G272.2−3.2	($09^h06^m50^s$, $-52°07'$)	10	0.4	[6]	this work	no obs.
G299.2−2.9	($12^h14^m50^s$, $-65°28'$)	3	0.5?	[7]	this work	no obs.
G347.3−0.5	($17^h13^m21^s$, $-39°46'$)	60	??	[8,9]	[10]	[11,12]

Ref. [1]Folgheraiter, Warwick, Watson, & Koyama (1997) [2]Yamauchi et al. (1999) [3]Tomida (1999) [4]Slane et al. (2001) [5]Iyudin et al. (2004) [6]Harrus et al. (2001) [7]Bai & Wang (2000) [8]Koyama et al. (1997) [9]Slane et al. (1999) [10]Cassam-Chenaï et al. (2004) [11]Uchiyama, Aharonian, & Takahashi (2003) [12]Lazendic et al. (2004a)

4.1 G156.2+5.7

4.1.1 Previous Observations

G156.2+5.7 (RX 04591+5147) was first discovered in the RASS data as a large shell-like SNR of 108'-diameter (Fig. 4.1; Pfeffermann, Aschenbach, & Predehl 1991). The totally circular shape shown by *ROSAT* suggests that G156.2+5.7 is a remnant of SN exploded in rather smooth ISM. The radio emission is highly polarized with a shell of 1.9° in diameter (Reich, Fuerst, & Arnal 1992), which indicates the radio emission is non-thermal. With *Ginga* observations, hard X-ray emission extended up to 10 keV was detected from the region of this SNR (Yamauchi et al. 1993). However, due to the poor spatial resolution of *Ginga*, whether this emission comes from the SNR or an overlapping source was not determined. From the pointing observation of the north and the center regions with ASCA, the hard X-ray emission was confirmed and located in the north and the center regions (Yamauchi et al. 1999; Tomida 1999). However, the emission mechanism of the hard X-ray could not be determined: synchrotron emission, bremsstrahlung, or inverse compton. They also found

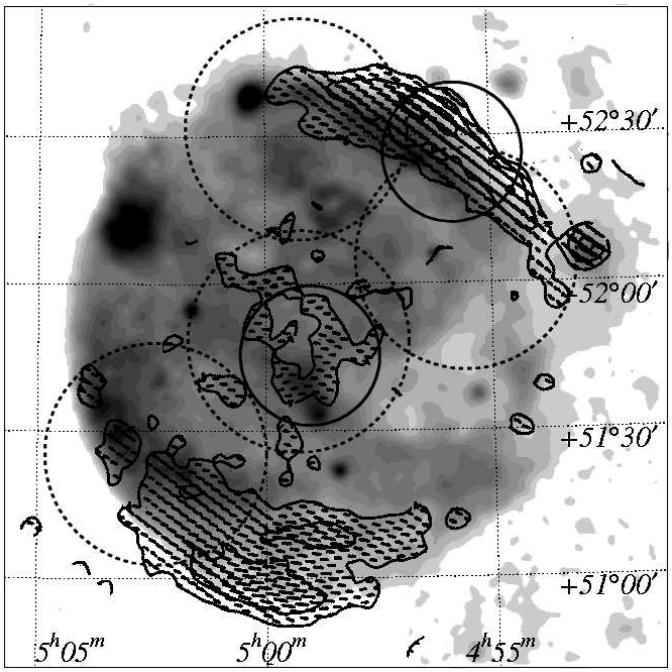

Figure 4.1: *ROSAT* gray-scale image of G156.7+5.7 with intensity map of the radio polarized component (Reich, Fuerst, & Arnal, 1992). The solid lines filling the radio contours designate the direction of polarization. Broken-line and solid-line circles indicate the fields of view of the *ASCA*/GIS observations and the *XMM-Newton* observations, respectively.

that the silicon and sulfur abundances in the center region are 3–5 and 3–10 times higher than the cosmic value. From the size (108′ diameter), X-ray flux ((1.2–1.6)$\times 10^{-9}$ ergs s^{-1} cm^{-2}), and temperature (0.4 keV), they estimated the age, distance, ambient density, and swept-up mass to be $\sim 1.5 \times 10^4$ yr, $\sim$ 1.3 kpc, $\sim$ 0.2 cm^{-3}, and $\sim$110 M$_\odot$, respectively, assuming this SNR is in the Sedov phase. Since this age is larger than that of SN1006, the archetype of SNRs emitting synchrotron X-ray, G156.2+5.7 is important in studying the history of particle acceleration in SNRs: how long particle acceleration continues in one SNR.

4.1.2 Mapping Observations with ASCA

Observations and Images

ASCA observed G156.2+5.7 five times in total (Table 4.2). Since the FOV of GIS is larger than SIS, we concentrate on the GIS results. We screen the GIS data with the standard criterion mentioned in §3.1.2. The resultant exposure times are shown in Table 4.2.

Table 4.2: *ASCA* observations performed on G156.2+5.7.

Obs. Id	Date	Pointed Direction	Expo.
	yyyy/mm/dd	(R.A., Dec.)$_{J2000}$	(ksec)
50010000	1993/09/03	($04^h59^m16\overset{s}{.}2$, $51°48'10''$)	10
50010010	1993/09/25	($04^h59^m17\overset{s}{.}4$, $51°48'12''$)	15
50011000	1993/09/24	($04^h59^m16\overset{s}{.}7$, $52°31'14''$)	19
57058000	1999/03/04	($05^h02^m23\overset{s}{.}7$, $51°25'22''$)	28
57059000	1999/03/05	($04^h55^m33\overset{s}{.}7$, $52°04'38''$)	32

We generated exposure-corrected GIS images of G156.2+5.7. First, the GIS2 and the GIS3 images of the five observations were overlaid, and a mosaicked NXB image normalized by exposure times was subtracted from it. The exposure map was created from the blank sky observations (see Sakano 1999). Next, dividing the NXB-subtracted image with the exposure map, we constructed a exposure-corrected composite image.

The resultant images in the 0.7–1.5 keV, 1.5–2.0 keV, and 2.0–7.0 keV ranges are shown in Figure 4.2 (a 3-color version of these images is shown in Appendix). The 0.7–1.5 keV band image is rather consistent with the *ROSAT* image: a shell like structure with enhancement in several regions (north, center, and south-east). A fan-like structure with point-like emission on its axis is seen in the center of both images. As the spectral analysis below shows, the X-rays in the 1.5–2.0 keV energy band are dominated by those of Si-K line and *ROSAT* was insensitive in this energy band. The image of this band show that Si is concentrated in the center region and suggests the ejecta exists in this region. The 2.0–7.0 keV band image shows that the hard X-ray emission is enhanced in the center and the north east regions, just as suggested by the *Ginga* observation (Yamauchi et al. 1993) and the previous analysis of the *ASCA* data (Yamauchi et al. 1999; Tomida 1999).

Spectral Analysis

In order to locate hard X-ray emission and to reveal spatial distribution of abundances, we extracted *ASCA* spectra from several regions shown in Figure 4.2. Although the data of the center observations have already been analyzed by Yamauchi et al. (1999) and Tomida (1999), we performed spectral analysis on the central circular region of $12'$ radius in order to easily compare the spectrum with that of the *XMM-Newton* observation. A point-like source (*dashed-line circle*) is excluded from the SW region with $3'$ radius. For the background, we used the blank-sky background provided by HEASARC, which are made from blank

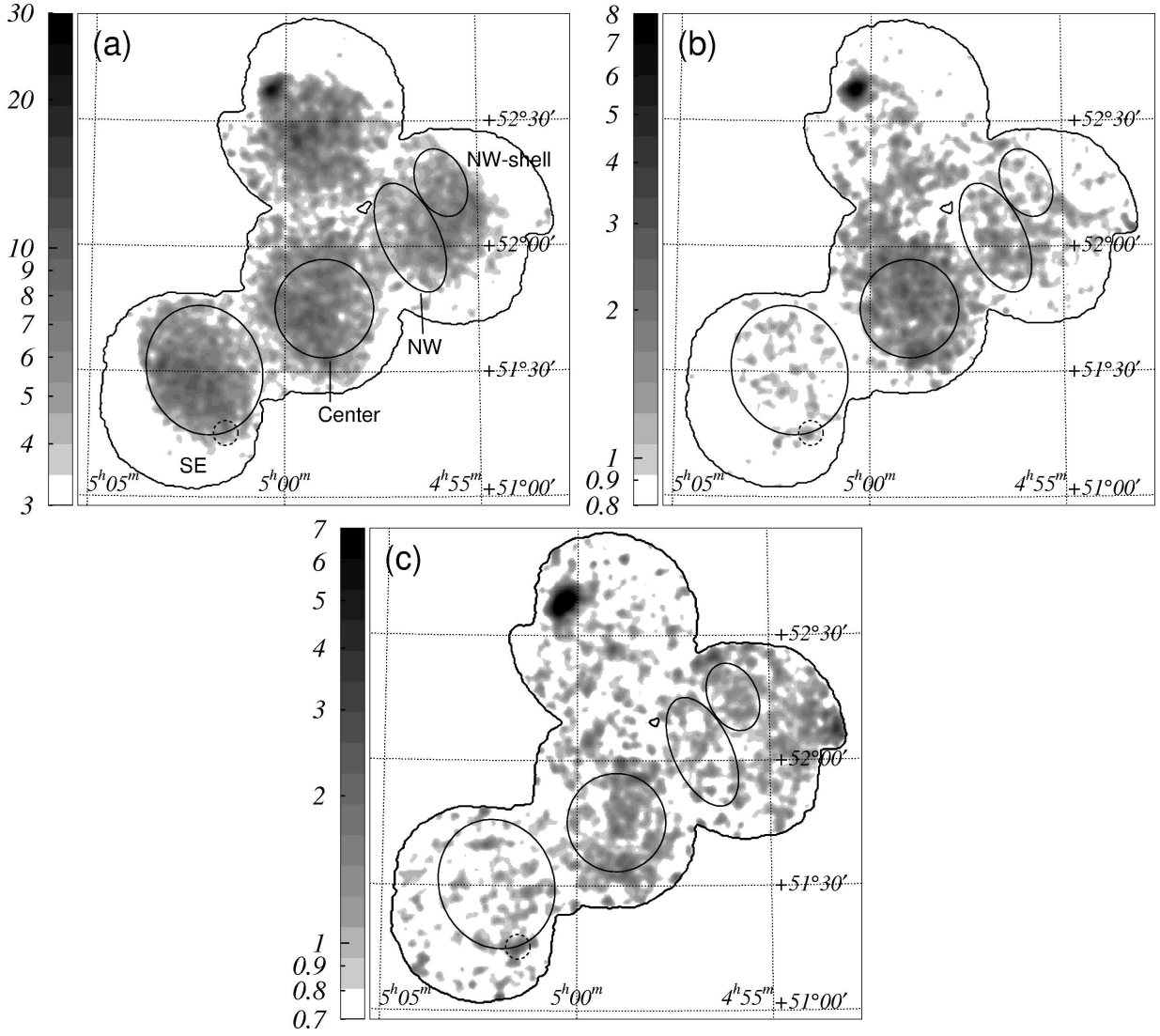

Figure 4.2: *ASCA* GIS images of G156.2+5.7 in the energy bands of 0.7–1.5 keV (a), 1.5–2.0 keV (b), and 2.0–7.0 keV (c). After the subtraction of the NXB, correction for the exposure was performed for each image. Scales are logarithmic and the numbers next to the scale bars show surface brightness ($\times 10^{-6}$ counts s^{-1} cm^{-2} $arcmin^{-2}$). The spectral regions are designated with solid lines.

sky observations by extracting point sources with flux larger than 1×10^{-13} ergs cm^{-2} s^{-1} (Ishisaki, 1997). Assuming the CXB is uniform on the sky, we extracted the background spectra from the same position of the detectors as the source regions.

The background-subtracted spectra are shown in Figure 4.3. Since the spectra of GIS2 and 3 are consistent with each other, both data are combined. As for the center region, the data of observations 50010000 and 50010010 are also combined after a check for the consistency. While the spectra of the SE and the NE regions are soft, those of the center and the NW-shell regions are hard showing X-ray emission extending up to 7 keV or higher. Si-K lines are prominent in the center and NW regions.

We first fitted these spectra with a NEI model (vnei model in XSPEC v11.3) modified by the ISM absorption. In order to correct for the systematic energy shift of GIS (Makishima et al. 1996), we applied 3% gain shift for all the spectra. Since the effective area of GIS is small in the soft band (< 1 keV), the spectra have weak constraint on the absorption column densities. We fixed them to the value 3.5×10^{21} cm^{-2} determined by Yamauchi et al. (1999) with ASCA/SIS, which is consistent with the total galactic H I column density in this direction (Dickey & Lockman 1990). The NEI model reproduce the spectrum of the SE region with the solar abundance (Anders & Grevesse 1989), whereas the spectrum of the NW region left residual at the Si and S lines. Therefore, we freed these abundances. As a result, the spectra of the SE and NW regions could be fitted with the NEI model with the best-fit parameters and models shown in Table 4.3 and Figure 4.3, respectively. The spectra of the Center and the NW-shell regions left residuals in the hard band (>3 keV) against the fitted NEI model. Accordingly, we allocated a power-law model for the hard X-rays. We then obtained acceptable fit for the spectrum of the NW-shell, whereas wavy residual remained in the energy band of $\sim$ 1.5–2.5 keV in the spectrum of the Center region suggesting that the abundances of Mg, Si, and S are different from the solar values. Therefore, we allowed the abundances of these elements vary and as a result, we obtained an acceptable fit. The best-fit parameters and the best-fit model with a NEI+power-law model are shown in Table 4.3 and Figure 4.3, respectively.

The abundances of Si and S are higher than the solar values not only in the Center region, but also in the NW region. The overabundance of Si in the NW region is consistent with the narrow band image (1.5–2.0 keV) in Figure 4.2. We confirmed hard X-ray emission from the Center region, and newly detected hard X-ray emission from the north-west shell region of G156.2+5.7.

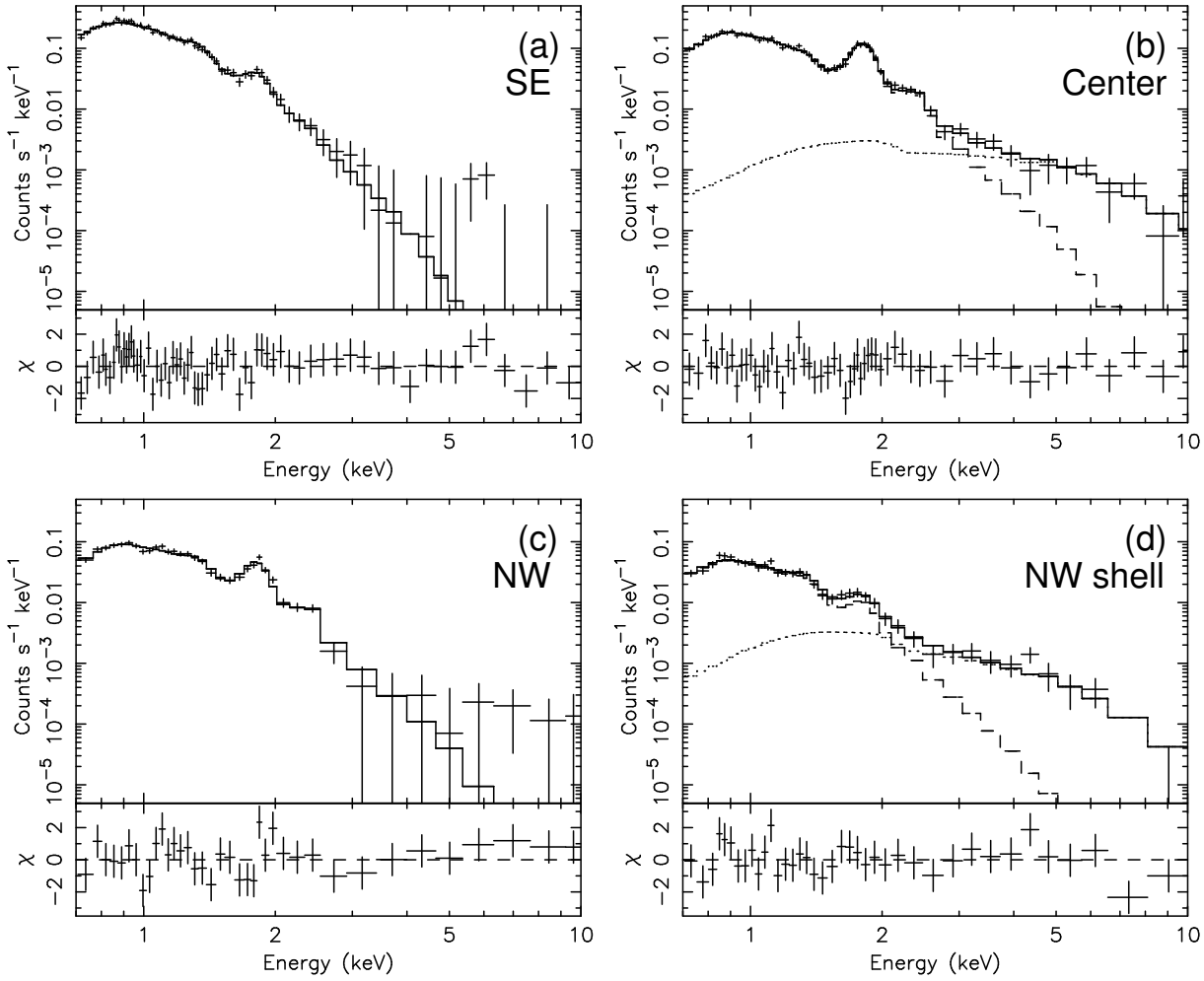

Figure 4.3: Background-subtracted *ASCA* spectra of the SE (a), center (b), NW (c), and NW-shell (d) regions. Best-fit models with parameters in Table 4.3 are shown with solid-lines. As for the spectra of the center (b) and the NW-shell (d) regions, the NEI and power-law components are shown with broken and dotted lines, respectively.

Table 4.3: Best-Fit Model Parameters of the *ASCA* G156.2+5.7 spectra.

Parameter	SE	Center	NW	NW-shell
NEI model:				
kT[keV]	$0.53^{+0.10}_{-0.07}$	$0.85^{+0.27}_{-0.21}$	$0.9^{+0.6}_{-0.3}$	$0.60^{+0.46}_{-0.15}$
Mg	1.0 (fixed)	$0.6^{+0.1}_{-0.1}$	1.0 (fixed)	1.0 (fixed)
Si	1.0 (fixed)	$3.2^{+1.2}_{-0.6}$	$2.7^{+1.4}_{-0.7}$	1.0 (fixed)
S	1.0 (fixed)	10^{+25}_{-5}	13^{+19}_{-8}	1.0 (fixed)
$\log(n_{\rm e}t$ [cm^{-3} s])	$10.5^{+0.4}_{-0.3}$	$10.5^{+0.2}_{-0.3}$	$10.4^{+0.6}_{-0.2}$	$10.7^{+1.0}_{-0.4}$
norm[a]	21^{+5}_{-4}	$6.3^{+2.9}_{-1.4}$	$4.9^{+3.3}_{-1.0}$	$3.0^{+2.1}_{-1.4}$
Power-law model:				
Γ	–	$0.8^{+0.8}_{-0.6}$	–	$1.7^{+0.6}_{-0.7}$
flux[b]	–	1.3×10^{-12}	–	6.3×10^{-13}
$N_{\rm H}$ [10^{21} cm^{-2}] ..	3.5 (fixed)	3.5 (fixed)	3.5 (fixed)	3.5 (fixed)
χ^2/d.o.f.	51.0/64	33.4/50	37.5/32	31.1/34

[a] $n_e n_p V/4\pi D^2 (\times 10^{11}$ cm$^{-5})$.

[b] Unabsorbed flux (ergs cm^{-2} s^{-1}) in the 2.0–10.0 keV.

4.1.3 Observations with *XMM-Newton*

In order to find out whether the hard X-ray emission detected with *ASCA* is truly diffuse or only a collection of faint point sources and to determine the emission mechanism of the hard X-rays, we performed *XMM-Newton* observations on the the center and the north-west regions.

Data Reduction, and Image

Observed dates and positions are shown in Table 4.4. In all these observations, the EPIC/PN and MOS cameras were operated in full frame mode with medium filter selected. Since the background showed flares during all the observations, we accumulated the background light curves of the full-field data between 10–12 keV energy (Appendix A), and screened out the time intervals when the count rate is larger than specific thresholds for each detector. We set the thresholds at 0.15 count s^{-1} for the MOS1 and 2 cameras and 0.7 count s^{-1} for the PN camera. Resultant exposures are shown in Table 4.4. Since the background light curves of observation 0148850101 show violent variability and only little exposures are left, we discarded this observation here. We hereafter call observations 0148850201 and 0205970201 as the center and the north-west observations, respectively, after their positions

on G156.2+5.7.

Table 4.4: *XMM-Newton* observations performed on G156.2+5.7.

Obs. Id	Date yyyy/mm/dd	Pointed Direction (R.A., Dec.)$_{J2000}$	Total Exposure M1/M2/PN (ks)	Screened Exp. M1/M2/PN (ks)
0148850201	2002/10/01	($04^h59^m00^s$, $51°45'00''$)	24/24/20	10/10/5.8
0148850101	2003/02/18	($04^h55^m55^s$, $52°26'00''$)	39/39/34	7.5/7.3/3.5
0205970201	2004/09/20	($04^h55^m50^s$, $52°26'00''$)	48/48/42	29/31/20

Figure 4.4 and 4.5 shows the MOS1+2 images of the north-west and the center observations in the 0.5–2.0 and 2.0–7.0 keV bands. In the soft band images, we see structures consistent with the *ROSAT* and *ASCA* images: in the north-west image the shell-like structure is conspicuous, whereas the triangle-like structure is seen in the center image. In the hard band, we see neither a clear diffuse structure nor clustered point sources. It is suggested that the extended hard X-ray emission found with the *ASCA* observations is not a collection of point sources but truly diffuse, although the brightness is too small in comparison with the EPIC background to be clearly recognized in those images.

Resolved Sources

In order to estimate the point-source contribution into the extended hard X-ray emission detected with *ASCA*, we first searched for point sources from the combined MOS1+2 images in the 2–7 keV band using the *emldetect* software. Since the PN images have large gaps and therefore the sky coverage is incomplete, we used only the MOS images here. The images were binned into pixel size of $3\farcs1 \times 3\farcs1$. We accepted source detection with likelihood values above 10 (about 4σ). As a result, 52 and 18 sources are detected from the north-west and the center observations, respectively (*crosses* in Figure 4.4 and 4.5).

For the bright sources with total counts larger than 100, we performed spectral analysis. The position of these sources are shown in Table 4.5, and designated with numbers in Figure 4.4 and 4.5. The source and background regions were selected to be circular regions of $20''$ radius and surrounding annular regions of $40''$ outer radii, respectively, except for source 4. If other sources are detected in those spectral regions (both the source and background), they were excluded with circular regions of $20''$ radius. Source 4 is extended, and is confirmed to be a cluster of galaxies after the spatial and spectral analysis. The detail is discussed in Appendix B. The background-subtracted spectra of sources 1–3 and 5 are shown in Figure 4.6. Since the spectra of sources 1, 2, and 5 are featureless, we fitted them

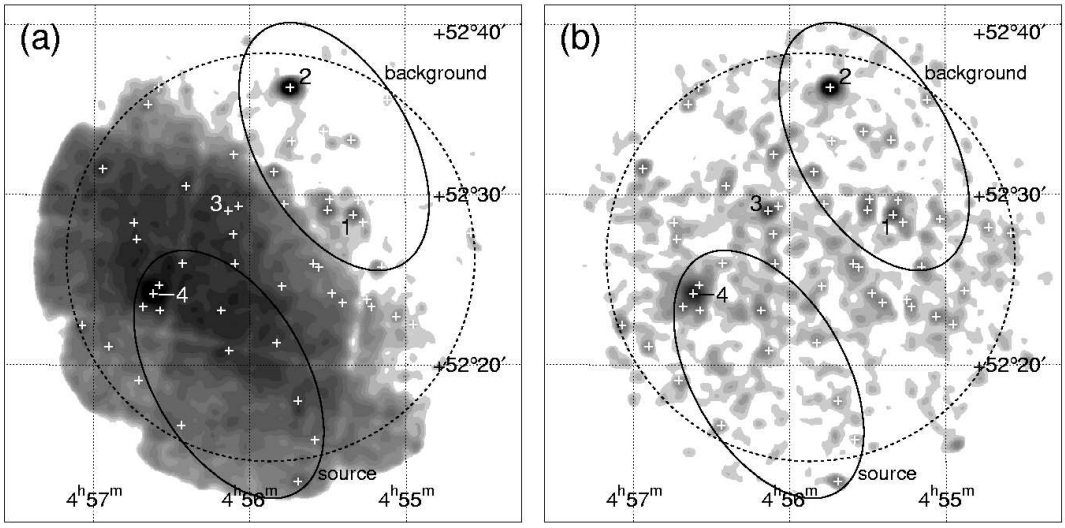

Figure 4.4: *XMM-Newton*/MOS1+2 images of the north-west region of G156.2+5.7 in the 0.5–2.0 keV (a) and 2.0–7.0 keV (b) bands. The point sources detected with the *emldetect* software in the 2.0–7.0 keV image are shown with plus signs. The spectral regions for the diffuse emission are shown with the solid-line ellipses. The dotted-line circle shows the 12′-radius region in which the diffuse hard X-ray emission detected with *ASCA* and the population of the hard point sources are studied.

with power-law models, resulting in acceptable fits with the best-fit parameters shown in Table 4.5. The photon indices and the absorption column densities are consistent with that these sources are background AGNs (Type 1). The spectrum of source 3 shows a concave structure and suggests Type 2 AGN. When fitted with a power-law model, the absorption column density became large and a marginal excess remained in the soft band (< 1 keV) a Type 2 AGN. However, since classification of each source is beyond the scope here, we only derive the flux in the 2.0–10.0 keV range here. We found that the hard X-ray fluxes (2–10 keV) of these relatively bright sources are well below that of the the diffuse X-ray detected with *ASCA*.

For sources with less photon counts (< 100), we estimated their fluxes on assumption of absorbed power-law spectra of photon indices Γ =1.4 and absorption column densities $N_{\rm H} = 3 \times 10^{21}$ cm^{-2}. The photon index is selected so as to be consistent with the analysis of the CXB by Moretti et al. (2003). The column density in this direction is so small that the flux in the 2.0–7.0 keV is insensitive to the value, but is chosen to be the same as the total galactic H I column density (Dickey & Lockman 1990). We estimated the counts-to-flux conversion factor for the MOS observations to be 3.8 cts s^{-1} per 10^{-10} erg cm^{-2} s^{-1} using

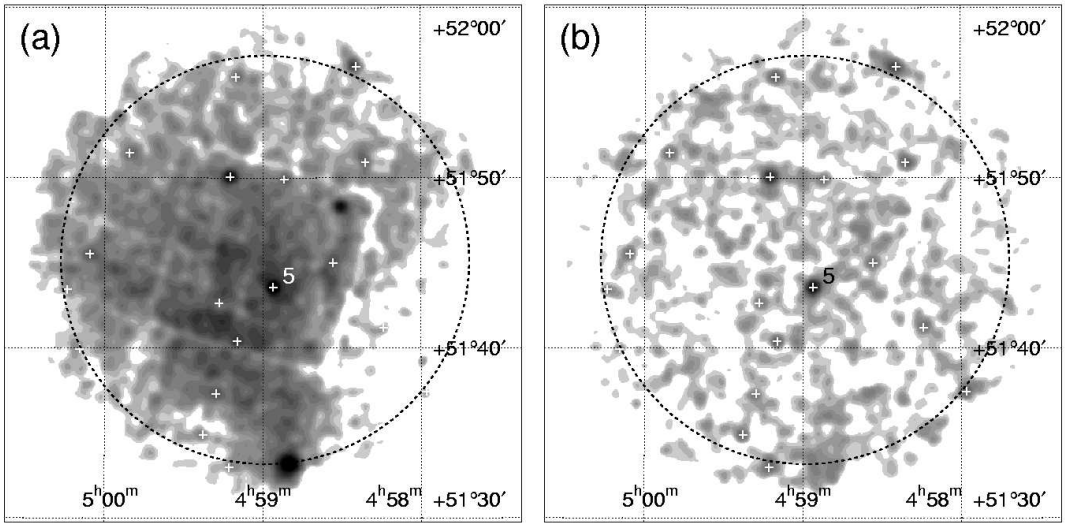

Figure 4.5: *XMM-Newton*/MOS1+2 images of the center region of G156.2+5.7 in the 0.5–2.0 keV (a) and 2.0–7.0 keV (b) bands. The point sources detected with the *emldetect* software in the 2.0–7.0 keV image are shown with plus signs. The dotted-line circle shows the 12′-radius region in which the diffuse hard X-ray emission detected with *ASCA* and the population of the hard point sources are studied.

version 3.6a of the *pimms* software. Using the resultant fluxes, we compared the cumulative flux distribution (log N–log S) of the 12′-radius regions shown in Figure 4.4 with that of the CXB. log N–log S is a distribution of the number of all sources brighter than S weighted by the sky coverage $\Omega_{\rm tot}$:

$$N(S) = \sum_{S_i > S} \frac{1}{\Omega_{\rm tot}(S_i)}. \tag{4.1}$$

By combining results of multiple surveys, Moretti et al. (2003) derived the log N–log S distribution of the CXB in the 2–10 keV band to be:

$$N(>S) = 5300 \left[\frac{(2\times10^{-15})^{1.57}}{S^{1.57} + (4.5\times10^{-15})^{1.13} S^{0.44}} \right] \ {\rm deg}^{-2}. \tag{4.2}$$

where S is measured in erg cm^{-2} s^{-1}. Figure 4.7 shows the log N–log S distributions of the G156.2+5.7 regions (*circle* and *square* for the center and the NW observations) and the CXB (*solid line*). We see the $\log N$-$\log S$ in the north-west and the center regions show excess against that of the CXB about a factor of 1.5–2.5. Therefore, the hard excess seen with the *ASCA* observation is partly due to the high population of point sources.

We computed flux sum of the point sources down to the detection limits. The detection limits for the north-west and the center observations are 2.0×10^{-14} and 3×10^{-14} erg cm^{-2} s^{-1},

Table 4.5: Bright Point Sources Detected in the G156.2+5.7 Observations.

	position	Power-law Parameters[a]			
No.	(R.A., Dec.)$_{J2000}$	Γ	N_H	flux	χ^2/d.o.f.
1	($04^h55^m20^s.1$, $+52°28'50''$)	$1.4^{+0.3}_{-0.3}$	$4.6^{+2.8}_{-1.3}$	7.8×10^{-14}	8.4/10
2	($04^h55^m44^s.4$, $+52°36'19''$)	$1.69^{+0.14}_{-0.13}$	$3.1^{+0.7}_{-0.5}$	3.7×10^{-13}	50.4/50
3	($04^h56^m08^s.4$, $+52°29'04''$)	$1.7^{+1.1}_{-0.6}$	60^{+60}_{-30}	8.4×10^{-14}	19.1/15
4	($04^h56^m37^s.2$, $+52°24'12''$)	—[b]	—[b]	(1.5×10^{-13})[b]	—[b]
5	($04^h58^m56^s.1$, $+51°43'34''$)	$1.65^{+0.27}_{-0.22}$	$3.0^{+2.0}_{-1.3}$	1.2×10^{-13}	7.7/13

[a] Best-fit parameters of a power-law model [photon index Γ, absorption column density N_H ($\times 10^{21}$ cm^{-2}), and absorbed flux (ergs cm^{-2} s^{-1}) in 2.0–10.0 keV].

[b] This source was fitted with a thermal model. See Appendix B.

respectively. The resultant values are compared with the flux sum of the CXB in the same flux range, and the flux of the extended emission detected with *ASCA* in Table 4.6. The flux sum of the point sources is excess against CXB for 3.5×10^{-12}, and 4.8×10^{-12} erg cm^{-2} s^{-1} deg^{-2} in the center and the north-west observations, respectively. In comparison with the fluxes of the hard X-ray emission detected with *ASCA*, these values are significantly smaller. Therefore, the hard X-ray emission can not be explained with the population excess of point sources.

Table 4.6: Comparison of the hard X-ray fluxes in the G156.2+5.7 region[a].

Regions	*ASCA*	resolved sources	CXB
Center.....	1.0×10^{-11}	6.3×10^{-12} [b]	2.8×10^{-12} [c]
NW	1.4×10^{-11}	8.8×10^{-12} [d]	4.0×10^{-12} [d]

[a] Fluxes in the 2.0–10.0 keV band normalized for the sky region ($\times$ erg cm^{-2} s^{-1} deg^{-2}) are shown.

[b] For sources $3.0 \times 10^{-14} < S < 1.2 \times 10^{-13}$ erg cm^{-2} s^{-1}.

[c] For sources $3.0 \times 10^{-14} < S < 1.0 \times 10^{-13}$ erg cm^{-2} s^{-1}.

[d] For sources $2.0 \times 10^{-14} < S < 1.0 \times 10^{-13}$ erg cm^{-2} s^{-1}.

Spectrum of the Diffuse Emission

For the next we analyze the X-ray spectrum of the diffuse emission directly. However, since the full field of view of the center observation is filled with the X-ray emission from G156.2+5.7, it is highly difficult to estimate the background, especially the soft proton component of the non-X-ray background, we avoid of analyzing the diffuse component of

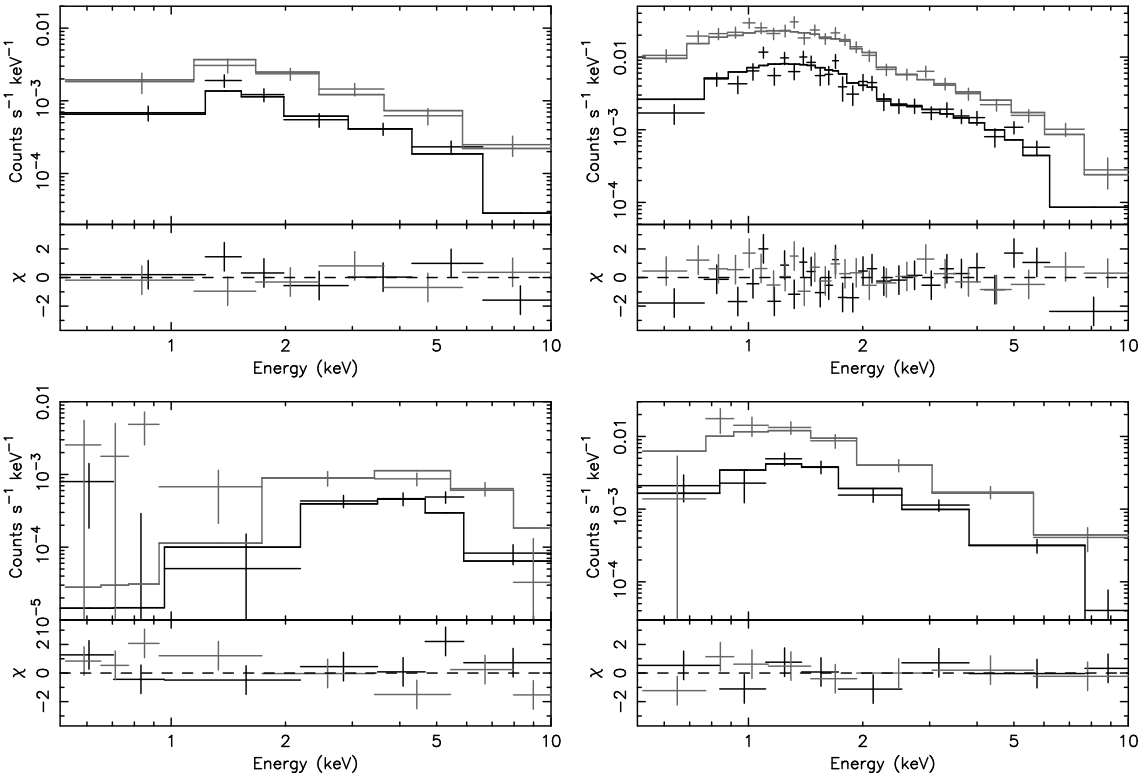

Figure 4.6: EPIC spectra of the point sources detected in the G156.2+5.7 observations. The combined MOS1 and 2 data are designated with black, whereas the PN data are designated with gray. The solid lines represent the best-fit power-law models (Table 4.5).

the center observation here. On the other hand, since the north-west observation covers the outer region of the soft X-ray emission, we can estimate the background from that region. We extracted the source and background spectra from the elliptical region shown in Figure 4.4, which were chosen so that both regions are on the same distance from the nominal point. The 20″ regions around point sources detected in the previous section were excluded from both regions. The extended source, source 4, was excluded with a circular region of 100″ radius.

The MOS1+2 spectra of the source and background regions are shown in Figure 4.8. Although we expect hard X-ray emission in the source region, no excess against the background region can be seen. We will discuss the hard X-ray emission, in the following. Figure **??** shows the background-subtracted spectra. We fitted this spectrum with a non-equilibrium ionization plasma (vnei model in XSPEC 11.3; Borkowski et al. 2001a). As a result, the model reproduced the spectrum quite well, with the best-fit parameters shown in Table 4.7.

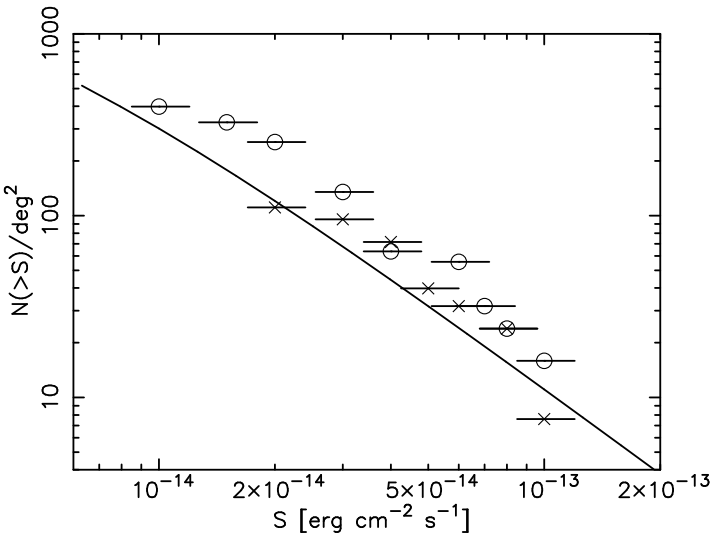

Figure 4.7: Cumulative source counts $N(S)$ in the 2–10 keV within the 12′-radius regions of the G156.2+5.7 observations. The data-point of the center and the NW observations are designated with the circles and crosses, respectively. The solid line refers to the CXB counts by Moretti et al. (2003).

All the abundances are consistent with the solar values.

Table 4.7: Best-fit Spectral parameters for the NW region with a NEI model.

kT (keV)	O	Ne	Mg	Si	Fe	log($n_e t$)	norm[a]	$N_{\rm H}^{\rm b}$	χ^2/d.o.f.
$0.29^{+0.03}_{-0.03}$	$0.5^{+0.7}_{-0.2}$	$0.8^{+0.9}_{-0.3}$	$0.6^{+0.6}_{-0.2}$	$1.0^{+1.1}_{-0.5}$	$0.6^{+0.4}_{-0.2}$	$11.3^{+0.3}_{-0.2}$	$1.9^{+1.1}_{-0.7}$	$5.3^{+0.7}_{-0.5}$	134/97

[a] $n_e n_p V/4\pi D^2 (\times 10^{12}$ cm$^{-5})$.

[b] Absorption column density ($\times 10^{21}$ cm^{-2}).

According to the *ASCA* result, hard X-ray emission is expected in the source region, but we found no excess against the background region. In Figure 4.10, we compare the spectral regions of the *ASCA* analysis and *XMM-Newton* analysis. The background region is outside of the thermal X-ray emission, wheras on the radio shell. Therefore, the hard X-ray emission may be extending out to the radio shell beyond the thermal X-ray shell.

4.1.4 Discussion on G156.2+5.7

We newly detected hard X-ray emission from the NW region with *ASCA*. With spatially resolved observations with *XMM-Newton*, the hard X-ray emission is found to be not due

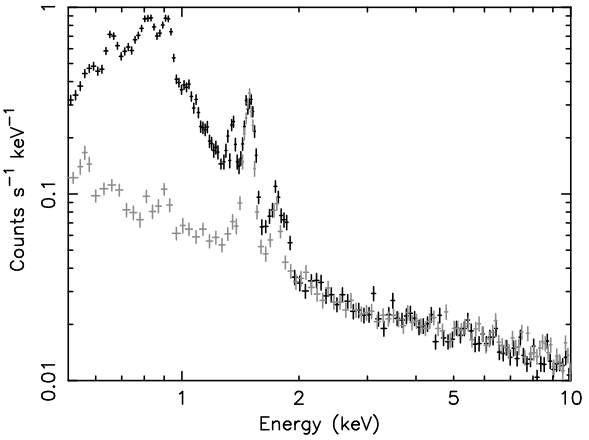

Figure 4.8: MOS1+2 spectra of the source (black) and background (gray) regions in the NW observation.

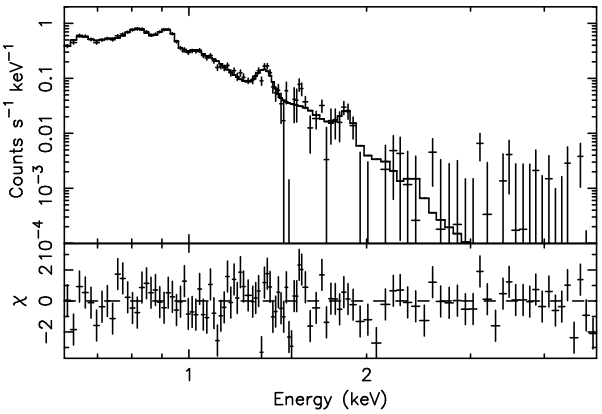

Figure 4.9: MOS1+2 spectra of the NW region. The best-fit NEI model is shown with the solid-line.

to collection of point sources but truly diffuse.

The photon index of the hard X-ray emission ($\Gamma \sim 1.5$) is small in comparison with SN 1006, the established SNR emitting synchrotron X-ray ($\Gamma \sim 2.2$; Bamba et al. 2003b). If we assume the X-ray emission is inverse compton of the cosmic micro-wave background, the fluxes and the photon (energy) indices of the radio and X-ray emission can be explained simultaneously with the magnetic field strength of 0.3 μG.

4.2 G272.2−3.2

4.2.1 Previous Observations

G272.2−3.2 was discovered by Greiner, Egger, & Aschenbach (1994) in the RASS. It presents a centrally filled X-ray morphology and a thermally dominated X-ray spectrum. The shape is nearly circular with a diameter of about 15 arcmin. In the optical band, Winkler, Hanson, & Phillips (1993) measured the [S$_{II}$]/Hα ratio and detected emission from [N$_{II}$] 658.3 nm and [O$_{II}$] 732.5 nm. Both of these characteristics are typical of SNRs and confirmed that the nebulosity is a SNR. From the *ROSAT* and *ASCA* observations, Harrus et al. (2001) found that the X-ray emission is described by an NEI model with a temperature of ∼0.7 keV, an ionization time-scale of the plasma of 3200 cm^{-3} yr, and a relatively high column density ($N_{\rm H} \sim 10^{22}$ cm^{-2}). From the thermal emission and the morphology, they interpreted this

]

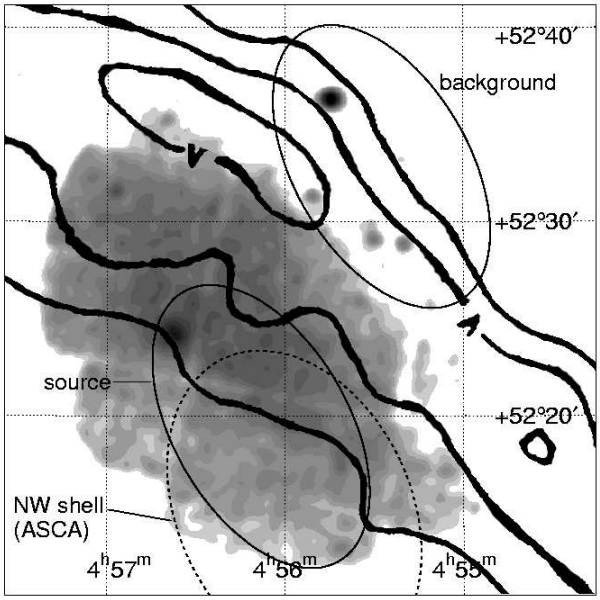

Figure 4.10: Comparison of spectral regions of G156.2+6.7 north-west. The *ASCA* NW-shell region (*dotted-line ellipse*), the source and background regions for the *XMM-Newton* observations (*solid-line ellipses*) are shown on the MOS1+2 image in the 0.5–2.0 keV band. The intensity contours of the polarized component of the radio emission (2695 MHz; Reich, Fuerst, & Arnal 1992) is overlaid.

remnant as a "thermal composite" SNR. In order to explain the centrally peaked X-ray morphology, they introduced cloud evaporation and thermal conduction models. Mainly because of the uncertainty in the distance toward the SNR, they could not conclude which model is the case.

4.2.2 Observation, Data Reduction and Image

G272.2−3.2 was observed with *XMM-Newton* on December 10, 2001. Both the PN, MOS1 and MOS1 cameras were operated in the standard full-frame mode with the thin filters. Since the coverage of the PN camera is not complete due to the large gap between CCD chips and statistics of the combined MOS1 and 2 data was enough for our study, we used the PN data only for consistency check. We report only the result of the MOS1+2 data. Since the background showed flares during the observations we accumulated the background light curves of the full-field data between 10–12 keV energy (Appendix A), and screened out

the time intervals when the count rate is larger than 0.15 count s^{-1} for the MOS1 and 2 cameras, and 0.7 count s^{-1} for the PN camera. The resultant exposure times are shown in Table 4.8.

Table 4.8: *XMM-Newton* observations performed on G272.2−3.2.

Obs. Id	Date yyyy/mm/dd	Pointed Direction (R.A., Dec.)$_{J2000}$	Total Exposure M1/M2/PN (ks)	Screened Exp. M1/M2/PN (ks)
0112930101	2001/12/10	($09^h06^m46.0^s$, $-52°07'12''$)	37/37/28	17/17/11

The MOS1+2 images in several energy bands are shown in Figure 4.11. In order to see spatial distribution of Si and S line emission, narrow-band images ((b) and (c)) were also created. The X-ray emission in the soft-band (0.7–2.0 keV) is rather smooth, supporting the *ROSAT* result. The emission in the 2.3–2.6 keV band is enhanced in the inner part suggesting that S is concentrated toward the center. No conspicuous emission is seen in the hard-band (3.0–7.0 keV).

4.2.3 Spectral Analysis

X-ray spectra were extracted from the three regions shown in Figure 4.11: the Inner region, the Outer region, and the Region A. The "A" region, where the X-ray emission is enhanced in the west part, corresponds to the region "A" in Harrus et al. (2001). The background for the region A was extracted from the elliptical region (*dotted-line ellipse*) shown in Figure 4.11. Since the vignetting effect is substantial and the center part of the FOV is occupied by G272.2−3.2 itself, the backgrounds for the Inner and Outer regions were estimated separately for the non-X-ray background and the CXB. The non-X-ray background was evaluated using the CLOSED data, whereas the CXB was derived from literature. According to Ishisaki (1997), the spectrum of the cosmic X-ray background above 1.2 keV is consistent with a single power-law with photon index 1.49±0.06 and the brightness of 10^{-8} ergs s^{-1} cm^{-2} str^{-1} in the 2–10 keV.

The background-subtracted spectra are shown in Figure 4.12. Since all the spectra show line emissions and suggested emissions from thin thermal plasmas, we fitted those with a NEI model (vnei model in XSPEC v11.2). As for the spectra of the Outer and Inner regions, power-law models with photon index 1.49 and Gaussians at energies 1.487 and 1.740 keV were added to represent the CXB, and the cosmic-ray induced instrumental lines (Al and Si lines), respectively. While the normalizations of the power-law models (the CXB) were fixed

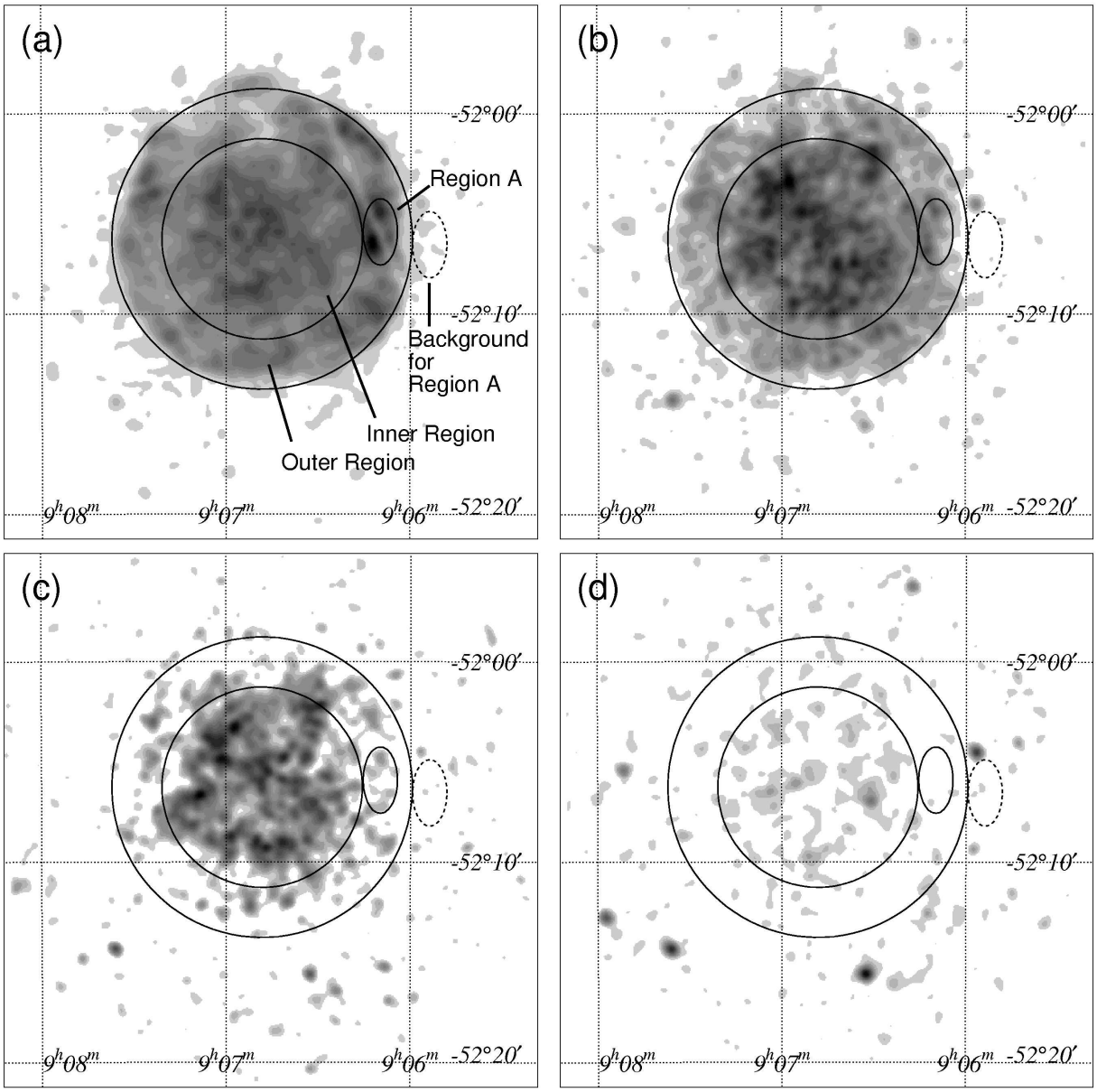

Figure 4.11: *XMM-Newton* MOS1+2 images of G272.2-3.2 in the energy bands of 0.7–1.7 keV (a), 1.7–2.0 keV (b), 2.3–2.6 keV (c), and 3.0–7.0 keV (d). Spectral region are designated with circles and ellipses. Scales are linear. Coordinates are R.A. and Dec. (J2000).

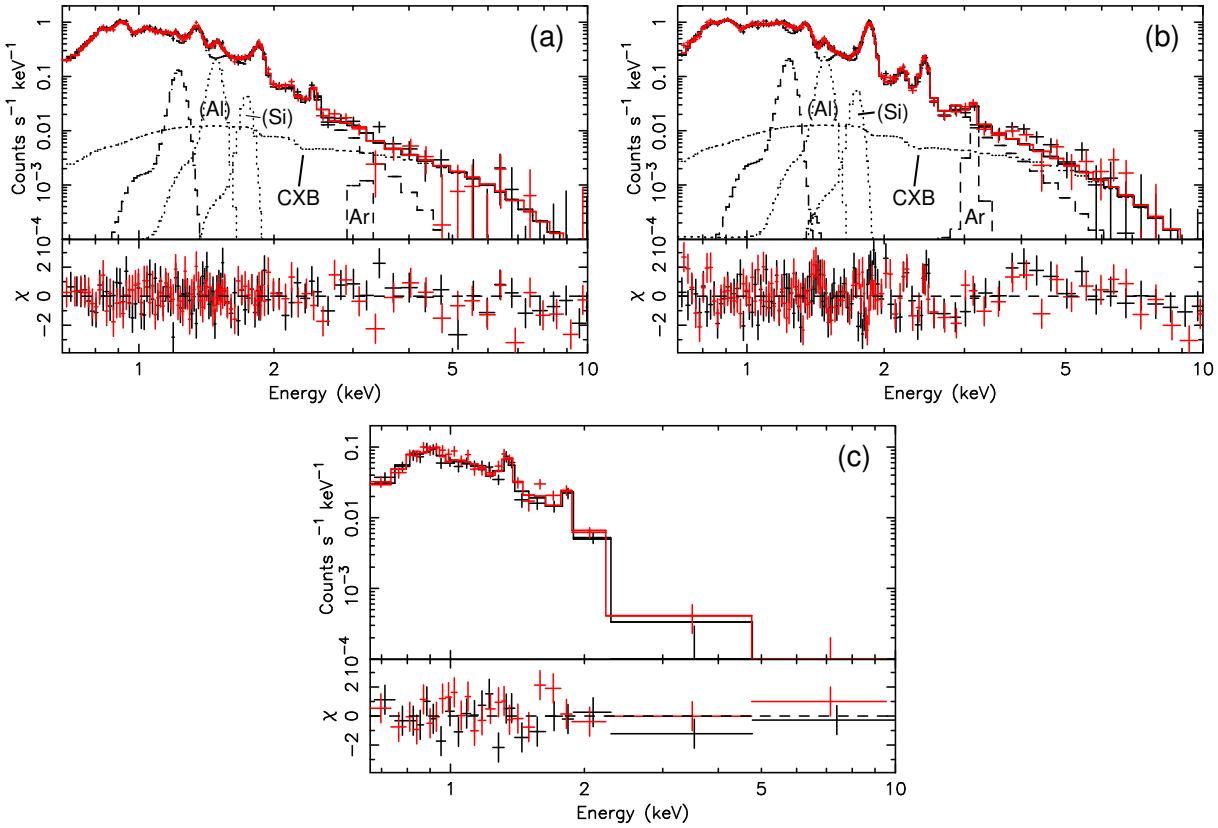

Figure 4.12: Background subtracted spectra of 3 regions of G272.2-3.2. (a): the Outer region. (b): the Inner region. (c): the region A.

to the value determined from the size of the sky region, the fluxes of the instrumental lines were fitted.

4.2.4 Discussion on G272.2−3.2

We found that the abundances in the inner part are higher than the solar values, while those in the outer part are lower than the solar. This suggests that the inner part is dominated by the ejecta, and that the outer part is dominated by the swept-up ISM. Therefore, it is inferred that this SNR is in the Sedov phase. It is notable that the abundance of the outer region which corresponds to that of the ambient ISM around G272.−3.2 is substantially lower than the solar value. Low abundances are reported on several SNRs in our Galaxy, for example the Cygnus Loop (Miyata et al. 1994).

The temperature of the ejecta is higher than that of the forward shock, which is also the

Table 4.9: Best-Fit Model Parameters for G272.2−3.2.

Parameter	Outer Region	Inner Region	Region A
NEI model:			
kT[keV]	$0.51^{+0.05}_{-0.05}$	$0.83^{+0.04}_{-0.08}$	$0.44^{+0.12}_{-0.09}$
O	$0.20^{+0.10}_{-0.09}$	$1.5^{+0.5}_{-0.7}$	$0.088(< 0.45)$
Ne	$0.34^{+0.12}_{-0.07}$	$1.0^{+0.3}_{-0.2}$	$0.17^{+0.25}_{-0.11}$
Mg	$0.28^{+0.06}_{-0.03}$	$0.9^{+0.1}_{-0.3}$	$0.20^{+0.14}_{-0.08}$
Si	$0.50^{+0.05}_{-0.05}$	$2.3^{+0.4}_{-0.4}$	$0.4^{+1.4}_{-0.1}$
S	$1.7^{+1.0}_{-0.4}$	$5.5^{+1.3}_{-1.3}$	1.0 (fixed)
Fe	$0.22^{+0.06}_{-0.04}$	$1.9^{+0.3}_{-0.5}$	$0.13^{+0.14}_{-0.07}$
$\log(n_{\rm e}t$ [cm^{-3} s])	$10.75^{+0.14}_{-0.12}$	$10.63^{+0.05}_{-0.08}$	$10.8^{+0.5}_{-0.5}$
norm[a]	$0.50^{+0.13}_{-0.13}$	$8.3^{+3.8}_{-1.5}$	$0.09^{+0.08}_{-0.06}$
Ar-line flux[b]	$2.0(< 5.3)$	$8.2^{+2.9}_{-3.1}$	...
Additional Line:			
center	$1.225^{+0.015}_{-0.011}$	$1.235^{+0.010}_{-0.005}$	...
flux[c]	$1.3^{+0.4}_{-0.3}$	$2.0^{+0.6}_{-0.4}$	...
$N_{\rm H}$ [10^{21} cm^{-2}] ..	$9.4^{+0.7}_{-0.5}$	$10.7^{+0.3}_{-0.3}$	$7.9^{+2.1}_{-2.4}$
χ^2/d.o.f.	183/182	308/200	44.6/40

[a] $n_e n_p V/4\pi D^2 (\times 10^{12}$ cm$^{-5})$.
[b] Flux of Ar-line ($\times 10^{-6}$ cm^{-2} s^{-1}). The center energy is fixed to 3.14 keV.
[c] $\times 10^{-4}$ cm^{-2} s^{-1}.

case for G349.7+0.2, an SNR expanding into a dense medium (Lazendic et al. 2004b). Since all the abundances of region A are consistent with those of the Outer region (the forward shock), the X-ray emission of Region A is enhanced not by ejecta but because the density of the ISM is locally high.

4.3 G299.2−2.9

4.3.1 Previous Observations

G299.2−2.9 was also discovered in the RASS data (Busser, Egger, & Aschenbach 1996). This object has a nearly circular shape with a diameter of $\sim$ 15 arcmin. The emission from this region was identified as two distinct sources in the Einstein Slew Survey: 1ES 1212−651 and 1ES 1212−652 (Slane, Vancura, & Hughes 1996). ESO/SRC red survey plates (ESO Schmidt

plate R 2978) show faint filaments around the southern rim of G299.2−2.9, with emission in the western and central regions as well. A ring emission is also evident in the *IRAS* data. The infrared emission is presumably associated with shock heating of the surrounding dust. Two distinct radio sources coincident with the extended regions of G299.2−2.9 are listed in the PMN 4.85 GHz radio survey catalog, with a combined flux of $\sim$ 180 mJy. Slane, Vancura, & Hughes (1996) proposed two scenarios for this SNR: a nearby young remnant and a distant Sedov-phase remnant.

4.3.2 *XMM-Newton* Observations

G299.2−2.9 was observed with *XMM-Newton* twice (Table 4.10). However, one of these observations (Obs. Id:0112890201) suffered from high background radiation due to the soft protons for all the exposure time. Therefore, we concentrate on the other one (Obs. ID: 0112890101). The MOS1 and MOS2 cameras were operated in the standard full-frame mode with the medium filters. High background intervals were screened out in the same manner as the analysis of G156.2+5.7 using the light curve of 10–12 keV events (see Appendix C?). Here, the threshold count rates were set to be 0.12, 0.12 and 0.5 count s^{-1} for MOS1, 2 and PN, respectively. The resultant exposures are shown in Table 4.10.

Table 4.10: *XMM-Newton* observations performed on G299.2−2.9.

Obs. Id	Date	Pointed Direction	Total Exposure	Screened Exp.
	yyyy/mm/dd	(R.A., Dec.)$_{J2000}$	M1/M2/PN (ks)	M1/M2/PN (ks)
0112890101	2002/02/24	($12^h15^m20\overset{s}{.}6$, $-65°30'23''$)	13/13/0.41	8.8/7.8/0.41
0112890201	2002/08/19	($12^h15^m10\overset{s}{.}4$, $-65°30'05''$)	15/15/9.5	0/0/0

The MOS1+2 images in several energy bands are shown in Figure 4.13. In the soft-band image (0.5–2.0 keV), we see a ring-like structure, which reminds us of a emission from the forward shock. The shape of the ring is not circular but rather elliptical with major and minor axes of $6'$ and $4\overset{'}{.}5$, which suggests asymmetrical explosion or non-uniform ambient ISM. The inner region of the ring-like structure is filled with relatively faint emission, which might be a reverse-shock component or a projected component of the forward-shock emission. There is a enhanced emission on the north-east part of the ring structure, which we call "Bright Spot", hereafter. There is also an emission outside of the ring in the north-east. In the Si and S bands, differences of the brightnesses between the Inner and Outer regions are less than in the soft band, which infer us the abundances of Si and S are larger in the Inner

Region. In the hard band, no emission is significant over the background.

X-ray spectra were extracted from the 4 regions shown in Figure 4.13: Inner Region, Outer Region, Bright Spot, and NE Edge. From the Outer Region, Bright spot and a hard source designated with a dashed-line circle was excluded. Background was extracted from a nearby source-free region on approximately the same distance from the nominal point as the source regions (*solid-line ellipse* in Figure 4.13). The background-subtracted spectra are shown in figure 4.14.

Table 4.11: Best-Fit Model Parameters for G299.2−2.9.

Parameter	Inner Region	Outer Region	Bright Spot	NE Edge
NEI model:				
kT[keV]	$0.46^{+0.01}_{-0.01}$	$0.44^{+0.03}_{-0.01}$	$0.44^{+0.07}_{-0.08}$	$0.42^{+0.08}_{-0.08}$
N, O	$0.14^{+0.02}_{-0.01}$	$0.14^{+0.03}_{-0.01}$	$0.15^{+0.07}_{-0.08}$	0.14(fixed)
Ne	$0.40^{+0.04}_{-0.03}$	$0.34^{+0.03}_{-0.03}$	$0.42^{+0.17}_{-0.11}$	0.34(fixed)
Mg	$0.33^{+0.08}_{-0.03}$	$0.30^{+0.03}_{-0.03}$	$0.49^{+0.19}_{-0.12}$	0.30(fixed)
Si	$1.9^{+0.2}_{-0.2}$	$0.61^{+0.05}_{-0.07}$	$0.6^{+0.3}_{-0.2}$	$1.4^{+0.6}_{-0.5}$
S	$4.8^{+0.8}_{-0.8}$	$2.1^{+0.7}_{-0.3}$	$2.3^{+2.5}_{-1.7}$	1.0 (fixed)
Fe	$0.56^{+0.06}_{-0.04}$	$0.26^{+0.03}_{-0.02}$	$0.32^{+0.08}_{-0.09}$	0.26(fixed)
log($n_e t$ [cm^{-3} s])	$11.22^{+0.03}_{-0.05}$	$10.98^{+0.04}_{-0.07}$	$11.01^{+0.36}_{-0.08}$	$10.8^{+0.8}_{-0.2}$
norm[a]	$1.11^{+0.09}_{-0.03}$	$5.4^{+0.7}_{-0.8}$	$0.7^{+0.2}_{-0.3}$	$0.33^{+0.30}_{-0.12}$
Additional Line:				
center	$1.23^{+0.01}_{-0.02}$	$1.231^{+0.017}_{-0.006}$	1.23 (fixed)	...
flux[b]	$7.9^{+2.2}_{-2.0}$	$1.4^{+0.2}_{-0.4}$	$0.15^{+0.10}_{-0.10}$	...
$N_{\rm H}$ [10^{21} cm^{-2}] ..	$3.2^{+0.3}_{-0.2}$	$3.1^{+0.1}_{-0.2}$	$2.9^{+0.8}_{-0.8}$	$2.9^{+0.7}_{-0.7}$
χ^2/d.o.f.	187/148	240/191	125/97	74.1/75

[a] $\int n_e n_p dV (\times 10^{12}$ cm$^{-5})$.

[b] Photon flux of the line ($\times 10^{-4}$ cm^{-2} s^{-1}).

4.3.3 Discussion on G299.2−2.9

The X-ray emission from the Outer region can be ascribed to the shock-heated swept-up interstellar matter. The plasma is in non-equilibrium ionization state ($n_e t \sim 1 \times 10^{11}$ cm^{-3} s). We found this SNR is in the Sedov phase of evolution. The absorption is almost consistent with the *ASCA* value ($(4.0 - 4.7) \times 10^{21}$ cm^{-2}; Bai & Wang 2000).

The abundances of elements lighter than Mg in the Inner and Outer regions are not

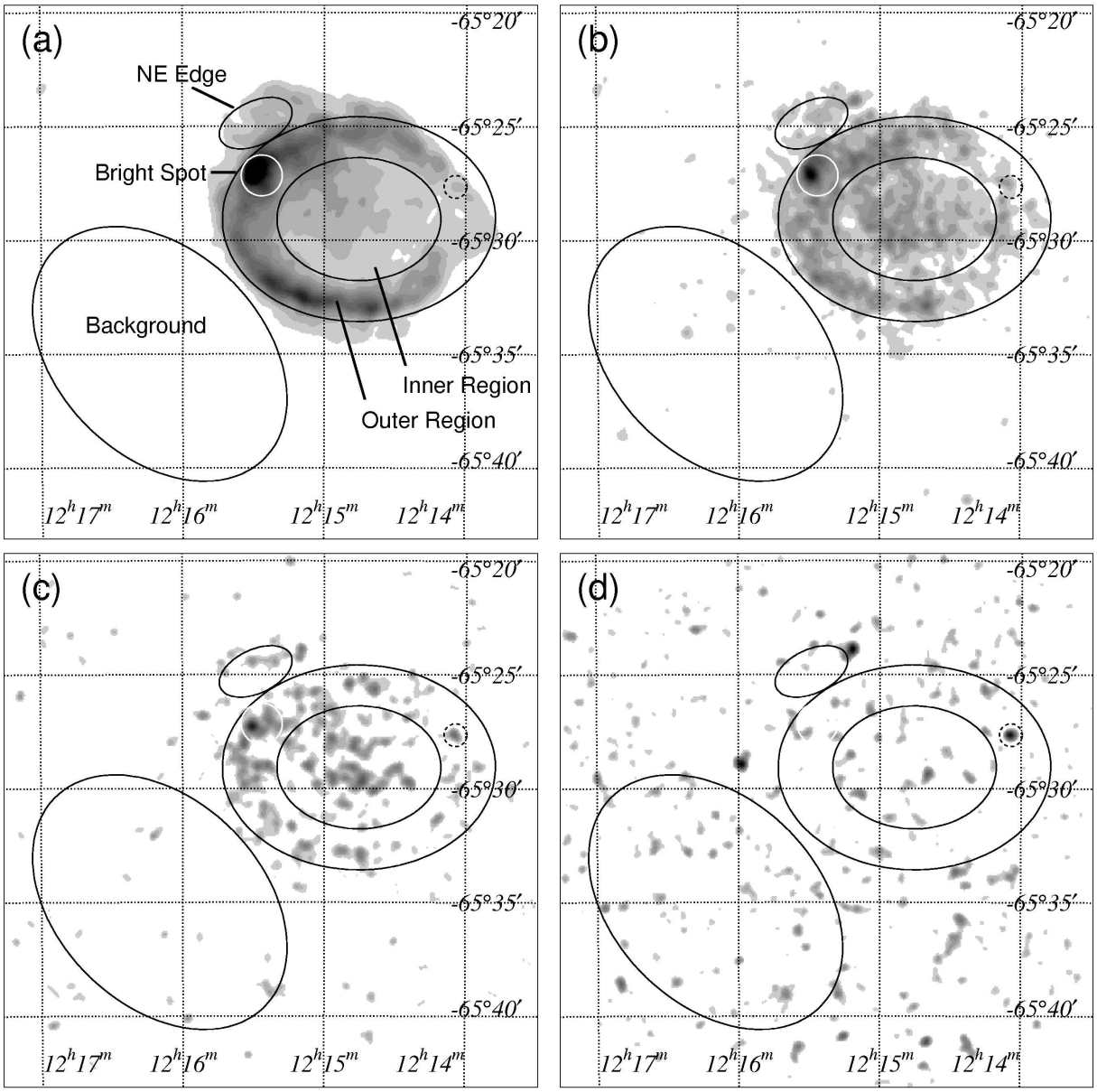

Figure 4.13: *XMM-Newton* MOS1+2 images of G299.2−2.9 in the energy bands of 0.5–1.7 keV (a), 1.7–2.0 keV (b), 2.3–2.6 keV (c), and 2.0–7.0 keV (d). Scales are linear. Coordinates are R.A. and Dec. (J2000).

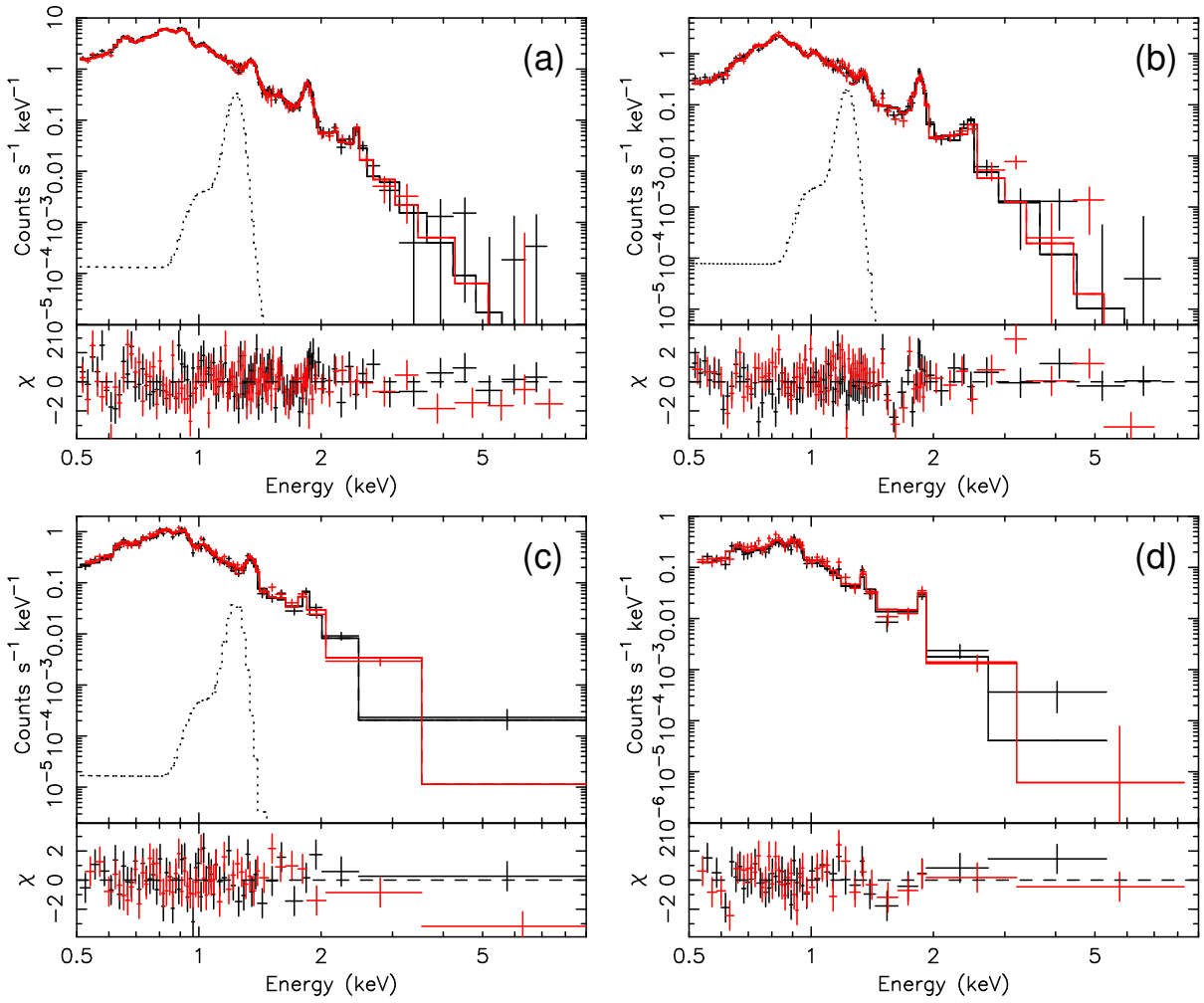

Figure 4.14: Background subtracted spectra of 4 regions of G299.2-2.9.

different within the 90% error regions. It suggests that the production of light elements are less in the supernova explosion. Therefore, it is inferred that the type of the SN was type Ia.

Chapter 5

Search for New SNRs with the *ASCA* Galactic Plane Survey

5.1 *ASCA* Galactic Plane Survey

The *ASCA* Galactic Plane Survey was performed from 1996 to 1999 (Yamauchi et al. 2002). This survey is a collaborative project of the *ASCA* team, aimed at the systematic study of the Galactic X-ray sources. It was planned to cover the area of the Galactic inner disk of $|l| \leq 45^\circ$ and $|b| \leq 0.^\circ 4$ with successive pointing observations with $\sim$ 10 ks exposure time for each. Comprehensive study of the survey is reported by Sugizaki (1999) and Sugizaki et al. (2001).

Soft X-rays are absorbed easily by the interstellar medium (ISM). For example, if we assume averaged hydrogen density of the ISM is 1 cm^{-3}, the mean free-path of a 1 keV X-ray photon is only $\sim$2 kpc. Therefore hard X-ray observations are essential for finding new X-ray sources embedded in the galactic plane. Moreover, since the Galactic Plane is bright diffuse X-ray source (the Galactic Ridge emission; e.g., Koyama et al. 1986; Kaneda et al. 1997), the imaging capability is required to reduce background and therefore essential for high sensitivity. From these reasons, the *ASCA* survey, which was the first survey with imaging capability in the energy band $>$ 3keV, is suited for finding faint X-ray sources in the galactic plane. As a matter of fact, X-ray emissions from about 20 SNRs are newly detected in this *ASCA* survey (Yamauchi et al. 2002).

5.2 New Extended Hard X-ray Sources

Although SNRs are the primary candidates for the acceleration sites of the galactic cosmic rays, what fraction of the flux showering onto the earth can be explained by SNRs is yet unknown. In order to resolve this issue, we have to proceed with mainly two studies: acceleration efficiency in each SNR and the number of SNRs in our Galaxy. For the former study, the number of SNRs exhibiting evidence of acceleration is yet too small. Therefore, more SNRs which show evidence of cosmic ray acceleration are required for the systematic study. The most sensitive information showing particle acceleration in SNRs is non-thermal X-rays such as synchrotron or bremsstrahlung. Since these X-ray emissions tend to extend up-to high energy than thermal X-rays, a survey in the hard X-ray band is suited. The study of the number of SNRs in our Galaxy, the latter study, should be performed with an X-ray survey. SNRs have been extensively searched for with radio observations. However, the Galactic plane is a strong radio emitter and the extended emission makes high background, and as a result, the sensitivity becomes lower in the regions near the galactic plane. As shown by the RASS, an X-ray survey should be a efficient way for discovering new SNRs.

Thus we searched for unidentified extended X-ray sources in the hard band images of the *ASCA* Galactic Plane Survey. Sugizaki et al. (2001) also searched for discrete sources, however, their survey was mainly sensitive for sources with extension smaller than the PSF of *ASCA* (FWHM $\sim 1'$) and they have not yet determined each source is extended or not. Therefore, many extended X-ray sources might remain to be found in the data set of the *ASCA* survey.

There are mainly 4 possibilities for extended X-ray objects located in the direction of the Galactic plane: SNRs, pulsar-wind nebulae, star-forming regions, and clusters of galaxies. Among the numbers of X-ray detected sources at this moment, that of SNRs is the largest. Therefore, SNRs are naively the most probable objects for unidentified extended X-ray sources. Although study of clusters of galaxies located behind the Galactic plane, especially toward the inner Galaxy, has been almost impossible due to the large absorption, the expected number can be estimated from the high latitude observations.

5.2.1 Source Finding

We used 173 pointing observations of the *ASCA* Galactic Plane Survey. Since about 34% of the surveyed regions are suffered from stray lights from nearby bright sources, we excluded these regions. The regions analyzed are the same as Sugizaki et al. (2001) (Figure 1) except

that the Galactic ridge observations (from $l = 57.^\circ5$ to $l = 62.^\circ5$) are not included in this thesis. We screened these data with the criterion shown in §3.1.2. To gain the statistical accuracy, we summed the data of GIS-2 and GIS-3, hereafter. Exposure corrected images of the AGPS data in the 0.7–2.0 and 2.0–7.0 keV bands were produced with the following procedures (see Figure 5.1):

(1) First, in order to make each image containing only cosmic X-ray events, non-X-ray background (NXB) is subtracted from the raw images. We used the night earth observations from 1993 to 1994 provided by HEASARC for estimating the NXB. The night earth observations are screened with the same criterion as the survey data (§3.1.2) except that ELV$< -5^\circ$. Then we normalized the image of the night earth observation for the exposure time, and subtracted it from each raw image.

(2) An exposure map for each observation is made from blank-sky observations with bright sources excluded, which Dr. Ishisaki kindly supplied. If we properly subtract NXB from the blank-sky observations, the data contain only the cosmic X-ray background. Since the cosmic X-ray background (CXB) can be thought to be flat, each pixel of the image shows efficiency map of the detector. We normalized the NXB subtracted blank-sky image for the exposure time and regard it as an exposure map. According to Ishisaki (1997), the brightnesses of the the CXB in the 0.7–2.0 keV and 2.0–7.0 keV bands are 8.5×10^{-7} and 6.0×10^{-7} counts cm^{-2} s^{-1} arcmin^{-2}, respectively. (These values are calculated from the energy flux in Ishisaki (1997) using the PIMMS software, on assumption that the spectrum of the CXB is an absorbed power-law with photon index $\Gamma = 1.5$ and $N_{\rm H} = 1 \times 10^{21}$ cm^{-2}.)

(3) Next, we mosaicked both the NXB subtracted images and the exposure maps by casting them onto the sky coordinate and by superposing them. Since the data of the survey is very large (long), the surveyed area is divided into $1.^\circ5$ long along the Galactic plane and analyzed. In order to avoid dividing extended structures with borders, we made margins of $0.^\circ25$ long on each end of the images and as a result, the size of each mosaicked image is $\sim 2.^\circ0 \times 0.^\circ8$.

(4) The mosaicked images are divided by the exposure maps. Here, the resultant images are exposure corrected images, with a number in each pixel designating surface brightness (counts cm^{-2} s^{-1} arcmin^{-2}) at that position.

We searched for extended sources from the exposure-corrected images in the 2.0–7.0 keV band. In order to avoid mistaking bright sources for diffuse sources, we first excluded sources with flux larger than 4×10^{-12} ergs cm^{-2} s^{-1} (0.7−10 keV) in Sugizaki et al. (2001). Next, in order to distinguish significant excess in these images, we made distributions of brightness

in each pixel and made images showing only pixels with brightness 1σ larger than the mode. Then, extended structures are searched for from those images. When a picked-up extended source has already been identified as a SNR or some other kind of objects by Sugizaki et al. (2001), it is excluded here. Images and names of extended X-ray sources discovered in this way are shown in Figure 5.2 and Table 5.1, respectively. Each source is designated with the galactic coordinate, such as G22.0+0.0.

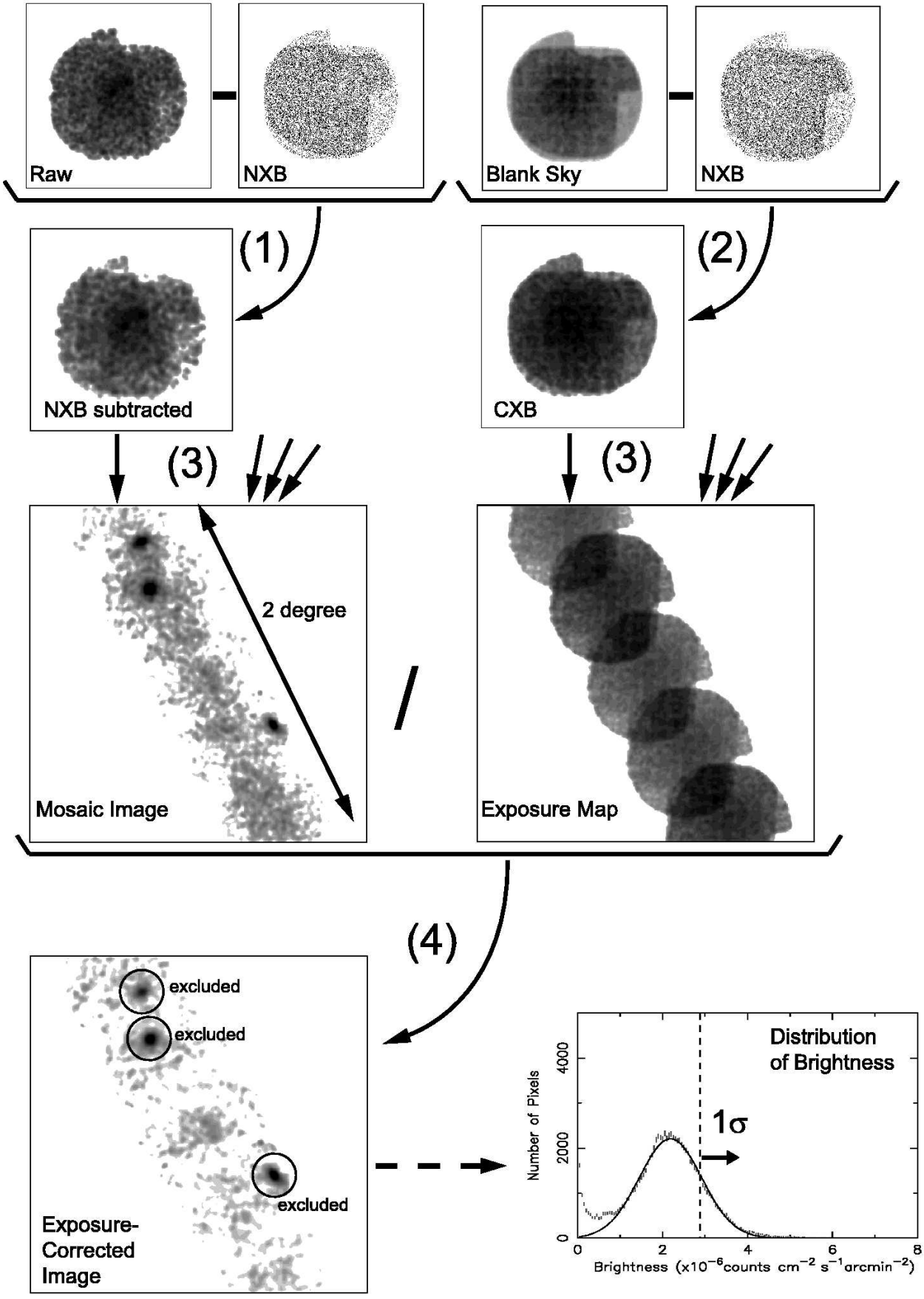

Figure 5.1: Flow chart of how to create an exposure-corrected mosaic image. The numbers in the parentheses correspond to the procedures in the text.

Table 5.1: Parameters of newly found extended hard X-ray sources.

Source Name	size	PL Parameters[a]				PSF[b]	PSF + Gauss[c]				
	(′)	Γ	$N_{\rm H}$	Flux	$\chi^2_\nu/\nu^{\rm d}$	$\chi^2_\nu/\nu^{\rm d}$	flux	σ (′)	norm	const.	$\chi^2_\nu/\nu^{\rm d}$
G11.0+0.0	15	$1.7^{+0.4}_{-0.4}$	$0.8^{+0.6}_{-0.5}$	4.0	31.2/33	173/48	22^{+9}_{-8}	$6.2^{+1.1}_{-0.9}$	$2.2^{+0.5}_{-0.4}$	$2.58^{+0.08}_{-0.10}$	36.8/46
G22.0+0.0	14	$1.0^{+0.7}_{-0.3}$	$0^{<1.3}$	2.2	17.3/18	153/48	$5^{<10}$	$6.4^{+1.8}_{-1.5}$	$1.7^{+0.6}_{-0.4}$	$2.25^{+0.09}_{-0.11}$	52.1/46
G23.5+0.1	16×12	$2.5^{+1.1}_{-0.8}$	6^{+4}_{-3}	2.5	12.3/9	103/48	$3^{<10}$	$6.6^{+1.3}_{-1.0}$	$2.5^{+0.8}_{-0.6}$	$2.00^{+0.12}_{-0.11}$	40.5/56
G25.0+0.0	11	$2.9^{+1.0}_{-0.7}$	$3.1^{+1.6}_{-1.1}$	2.2	22.9/8	87.6/48	$2^{<5}$	$4.6^{+1.4}_{-1.0}$	$1.3^{+0.6}_{-0.4}$	$2.44^{+0.06}_{-0.07}$	47.3/46
G25.5+0.0	12	$1.9^{+0.8}_{-0.6}$	$1.9^{+1.3}_{-0.9}$	1.8	12.5/17	211/48	$0^{<3}$	$6.4^{+1.5}_{-0.9}$	$1.9^{+0.3}_{-0.3}$	$2.45^{+0.08}_{-0.11}$	67.7/46
G26.0+0.0	16	$2.2^{+1.3}_{-0.9}$	5^{+6}_{-3}	2.7	4.0/10	187/48	$0.9^{<5}$	$9.7^{+2.4}_{-1.5}$	$1.6^{+0.2}_{-0.2}$	$2.2^{+0.1}_{-0.3}$	50.4/46
G26.6−0.1	14	$1.2^{+0.6}_{-0.3}$	$0.1^{+0.9}_{-0.1}$	2.8	20.1/12	—	—	—	—	—	—
G28.6−0.1	11	$2.1^{+1.0}_{-0.8}$	$2.4^{+2.1}_{-1.0}$	2.2	10.0/11	136/48	$1^{<6}$	$4.4^{+0.9}_{-0.7}$	$2.3^{+0.7}_{-0.6}$	$2.22^{+0.07}_{-0.07}$	46.5/46
G32.45+0.1	10	$2.6^{+1.8}_{-1.2}$	7^{+9}_{-4}	2.0	2.9/8	128/48	$2^{<8}$	$3.9^{+0.8}_{-0.6}$	$3.0^{+0.9}_{-0.8}$	$2.26^{+0.07}_{-0.07}$	34.4/46
G35.5+0.0	14×10	$1.2^{+0.2}_{-0.2}$	$0^{<0.2}$	2.3	19.8/14	123/48	12^{+5}_{-5}	$6.5^{+2.0}_{-1.5}$	$1.2^{+0.4}_{-0.3}$	$1.60^{+0.07}_{-0.09}$	52.2/46
G36.0+0.0	17	$1.3^{+0.7}_{-0.4}$	$2.7^{+2.4}_{-1.5}$	2.6	25.2/14	97.0/48	7^{+4}_{-3}	$8.3^{+3.4}_{-1.7}$	$0.9^{+0.2}_{-0.2}$	$1.54^{+0.08}_{-0.14}$	31.2/46
G37.0−0.1	7	$2.0^{+1.1}_{-0.9}$	7^{+7}_{-4}	2.2	8.2/5	90.3/48	26^{+9}_{-12}	5^{+4}_{-2}	$1.2^{+1.7}_{-0.6}$	$1.45^{+0.07}_{-0.10}$	51.9/46
G316.8−0.1	7	$2.4^{+1.0}_{-0.8}$	$3.1^{+2.3}_{-1.6}$	1.3	1.6/5	76.2/48	$7^{<19}$	$1.6^{+0.7}_{-0.1}$	6^{+4}_{-3}	$1.38^{+0.05}_{-0.04}$	50.2/46
G318.6+0.0	18×12	$2.2^{+1.6}_{-1.1}$	10^{+13}_{-6}	2.5	19.3/12	71.9/23	$1^{<5}$	$4.7^{+1.6}_{-1.0}$	$1.2^{+0.5}_{-0.4}$	$1.35^{+0.05}_{-0.07}$	16.0/21
G337.1+0.0	15	$1.8^{+0.9}_{-0.6}$	7^{+6}_{-3}	3.9	30.8/21	183/48	21^{+5}_{-7}	$7.9^{+1.8}_{-1.2}$	$1.9^{+0.3}_{-0.3}$	$2.25^{+0.12}_{-0.16}$	34.3/46

[a] Best-fit parameters of a power-law model [photon index Γ, absorption column density $N_{\rm H}$ ($\times 10^{22}$ cm^{-2}), and absorbed flux ($\times 10^{-12}$ ergs cm^{-2} s^{-1}) in 2.0–10.0 keV] are shown.

[b] The fitting results of the radial profiles with a PSF + constant. Since the fitting was rejected for all the sources, only χ^2 is shown.

[c] Best-fit parameters of the radial-profile with a combined model of a PSF + a Gaussian + constant [Flux of the central point source ($\times 10^{-5}$ counts cm^{-2} s^{-1}), σ and normalization (counts cm^{-2} $^{-1}$ arcmin^{-2}) of the Gaussian, the brightness of the constant component ($\times 10^{-6}$ counts cm^{-2} s^{-1} arcmin^{-2}), and reduced χ^2] are shown.

[d] χ^2/degree of freedom (ν).

5.2.2 Spatial and Spectral Characteristics of Newly Found Sources

We tested whether these newly found sources are significantly extended or not by making radial profiles. The NXB was subtracted from the radial profiles and the vignetting and exposure were corrected, utilizing the exposure map made in the above.

The center of the radial profile of each source was determined as follows: (1) If there is a (point) source listed by Sugizaki et al. (2001) inside the candidate, the center of the profile was determined to its position. (2) If multiple sources by Sugizaki et al. (2001) are located inside, the center was determined to the position of the brightest one. (3) If no source is detected inside, the center of the profile was manually determined to be approximately the center of the emission. Before binning the images, regions of nearby sources listed in Sugizaki et al. (2001) are excluded with circular regions of $3'$ or $6'$ radii, depending on the flux in the 0.7–10 keV range ($6'$ for flux $> 5 \times 10^{-12}$ ergs cm^{-2} s^{-1}, and $3'$ for else; *thick solid-line circles* in Figure 5.2).

The resultant radial profiles are shown in Figure 5.3. We see the profiles are flat at the large radii and therefore can confirm that the correction for the vignetting and exposure is properly performed. In order to determine whether these profiles can be explained with a point source or not, we first fitted these profiles with a point-spread function (PSF) + constant. The PSF was evaluated with the observations of Cyg X-1 (Takahashi et al. 1995). We made radial profiles of Cyg X-1 observed on several positions of GIS and fitted those with 3 gaussians. As a result, we found that best-fit 3 gaussians for pointing "P3" with GIS 3 can reproduce any PSF in the FOV better than 20% for radius between $0'$ and $2'$. Thus we used the best-fit 3 gaussians as the PSF. If the fitting was rejected with a 90% confidence level, we fitted the profile adding a Gaussian for the next. The results are tabulated in Table 5.1. We found no radial profiles of the candidates can be explained with a point source (a PSF + constant), and thus we can conclude that all the 15 sources listed here are extended sources.

X-ray spectra of the newly found sources are extracted with the source and background regions shown in Figure 5.2 (*thin solid lines* and *thin broken lines*, respectively). The point sources located inside the source regions are included into the spectra, whereas those located inside the background regions are excluded with circular regions of 2' radii.

The background-subtracted spectra are shown in Figure 5.4. In order to estimate the hardness and absorption of each source, we first fitted each spectrum simply with a power-law model. The resultant best-fit parameters are shown in Table 5.1. For several sources, the power-law model was rejected with a 90% confidence level. Fittings with other models are discussed in §5.3.

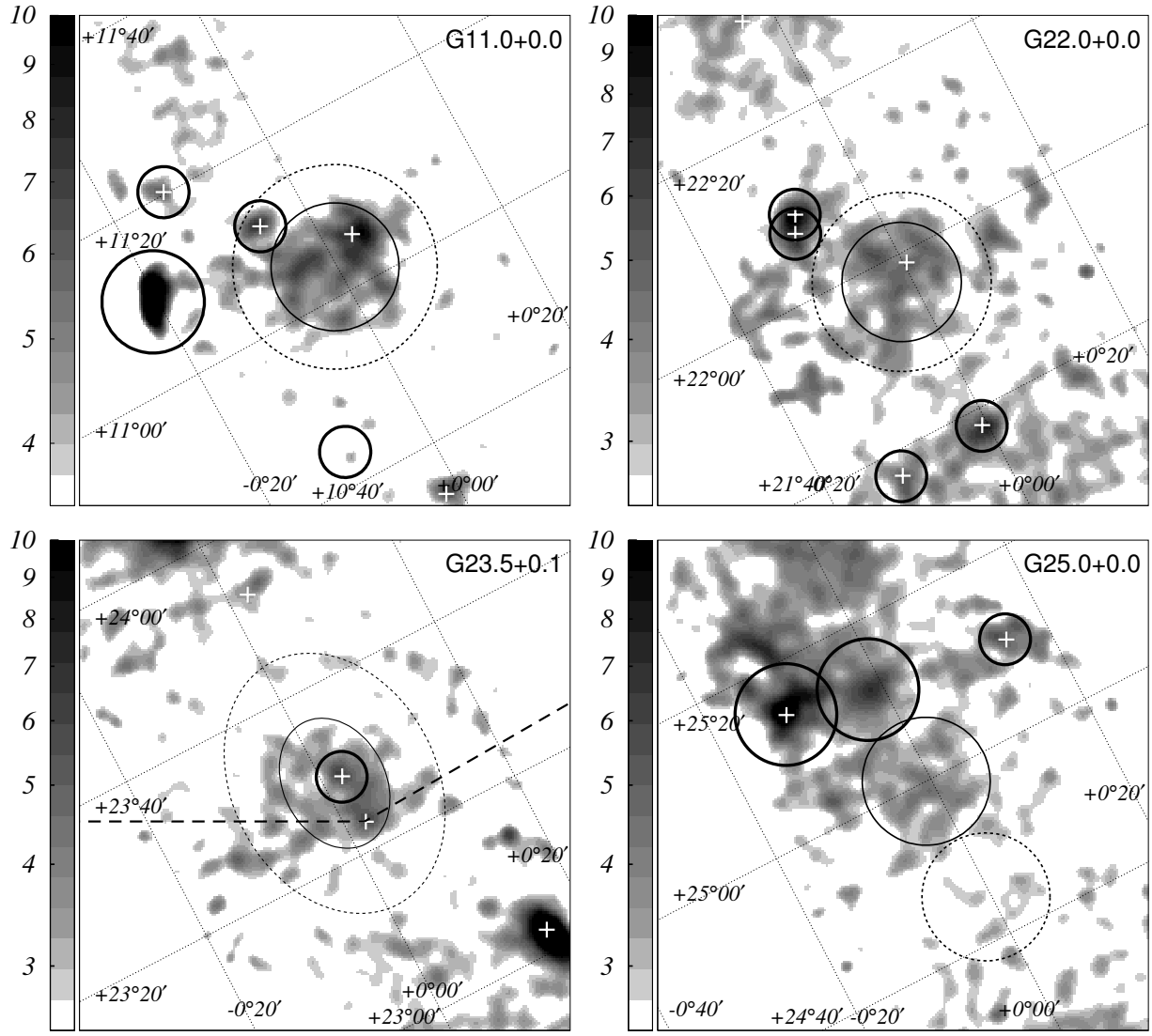

Figure 5.2: ASCA GIS images of newly found extended X-ray sources in the 2.0–7.0 keV band. See text about the production of these images. Scales are logarithmic and the numbers next to the scale bars show surface brightness ($\times 10^{-6}$ counts cm^{-2} s^{-1} arcmin^{-2}). The orientation is equatorial (J2000), whereas the coordinates shown are galactic. The sources detected in Sugizaki et al. (2001) are designated with white crosses. The circular regions excluded from the radial profiles are shown with thick solid-line circles (small, and large ones are with radii of $3'$ and $6'$, respectively). As for G23.5+0.0, only the northern region of the dashed-lines is used for the radial profile. The source and background regions for the spectra are designated with thin solid lines and dotted lines (a circle or an ellipse), respectively.

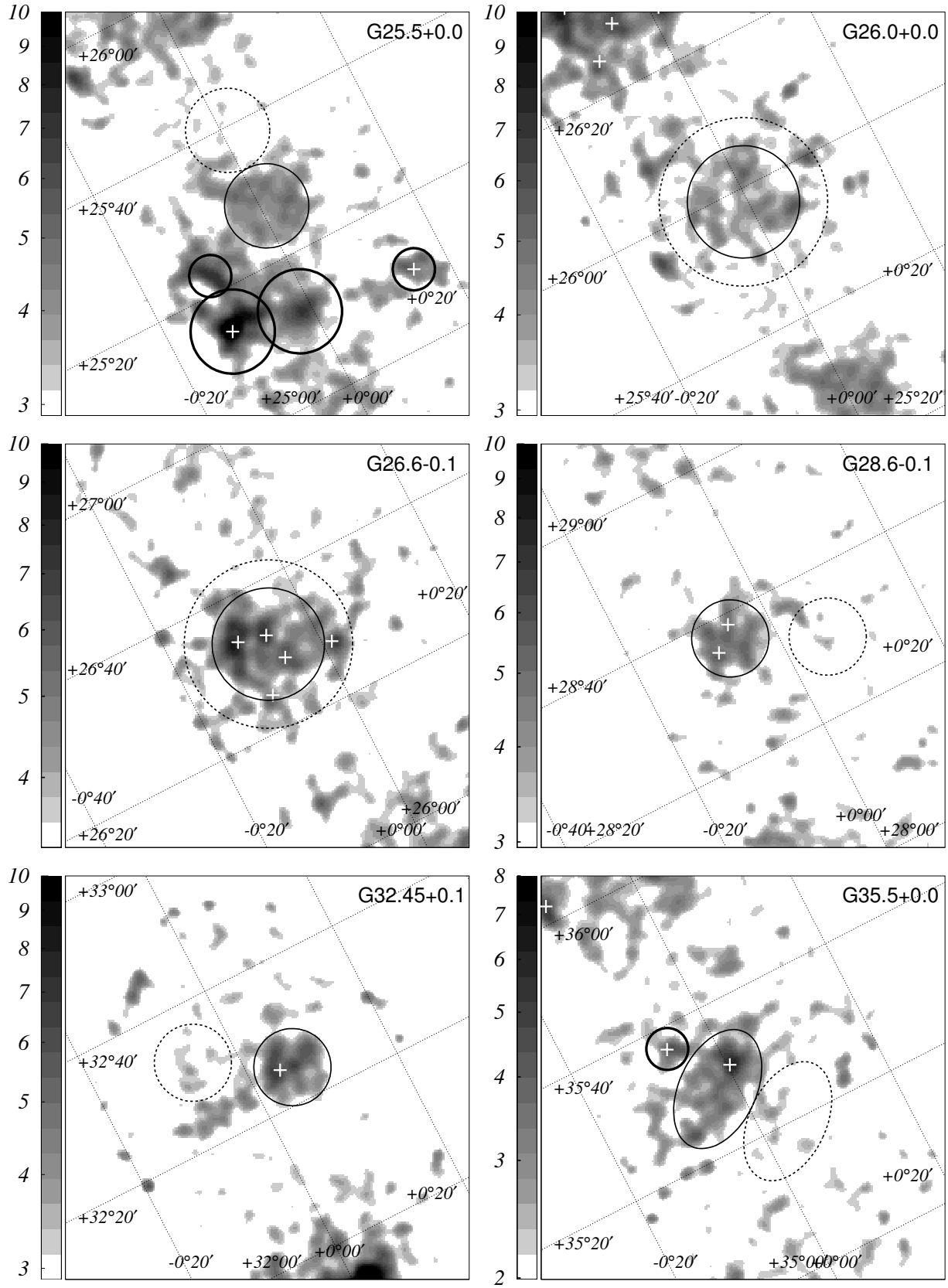

Figure 5.2: (Continued)

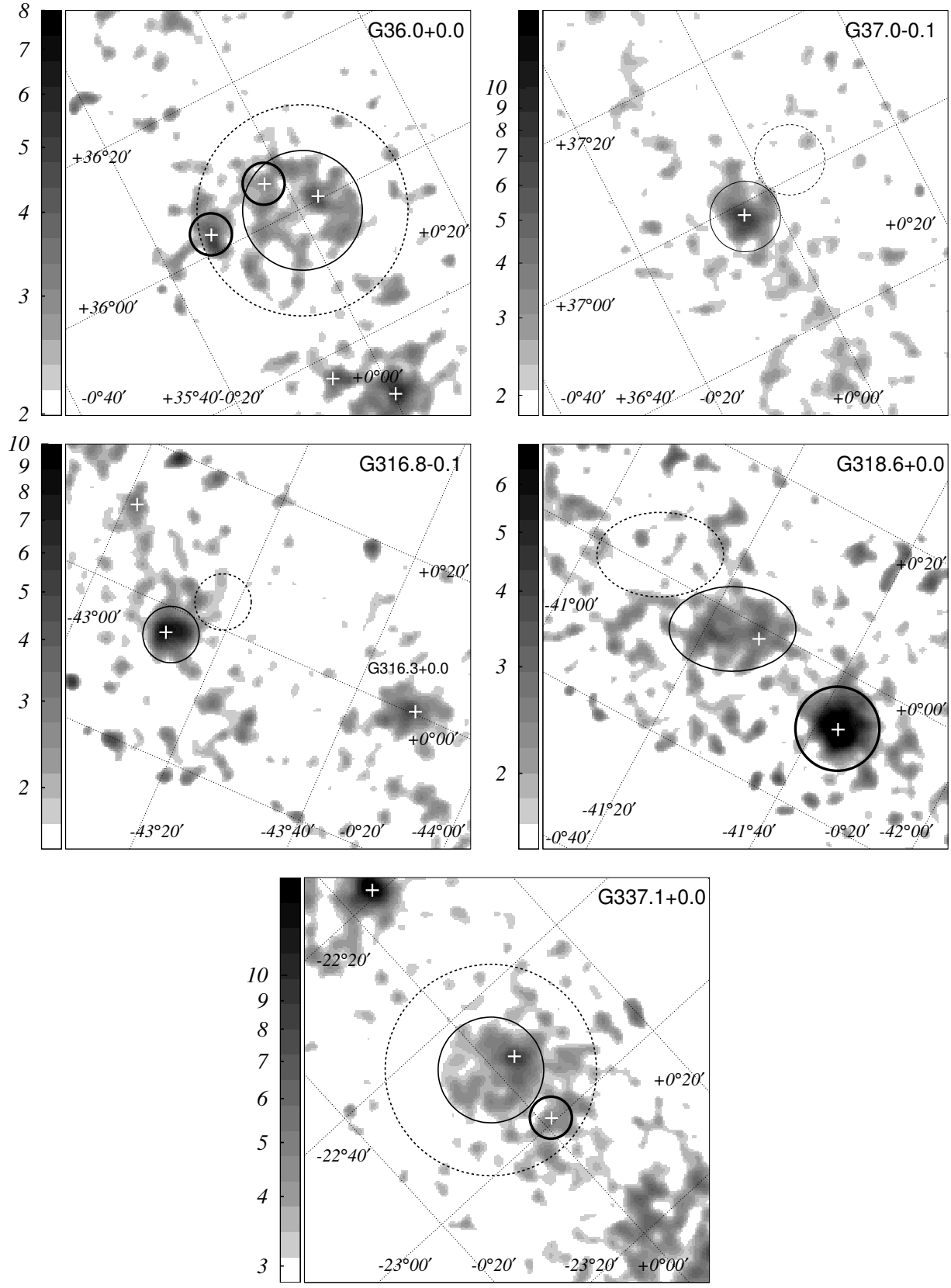

Figure 5.2: (Continued)

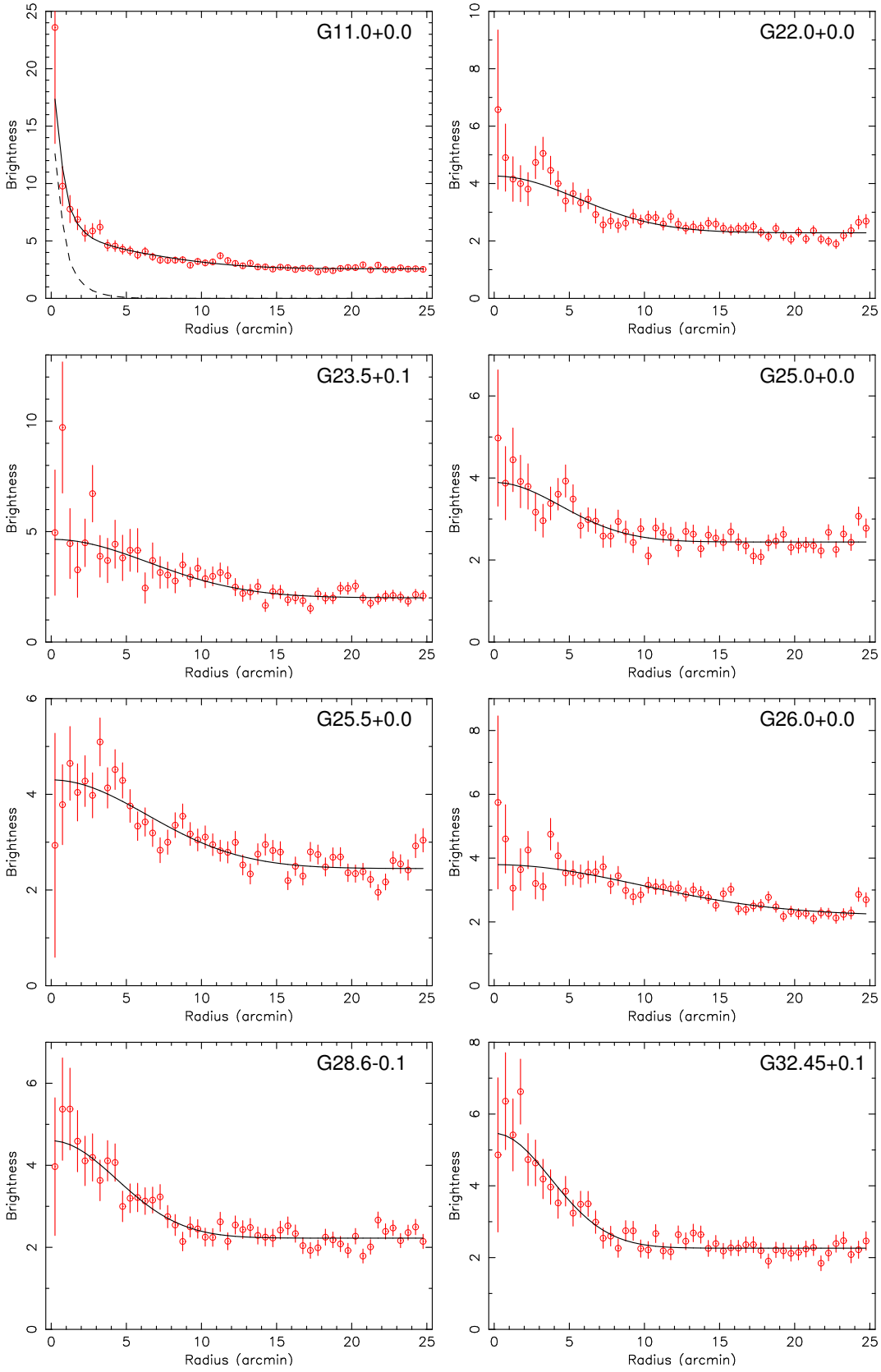

Figure 5.3: Radial profiles of the newly detected SNR candidates. The vertical axis shows brightness ($\times 10^{-6}$ counts cm^{-2} s^{-1} arcmin^{-2}). The best-fit models (Table 5.1) are shown with solid lines.

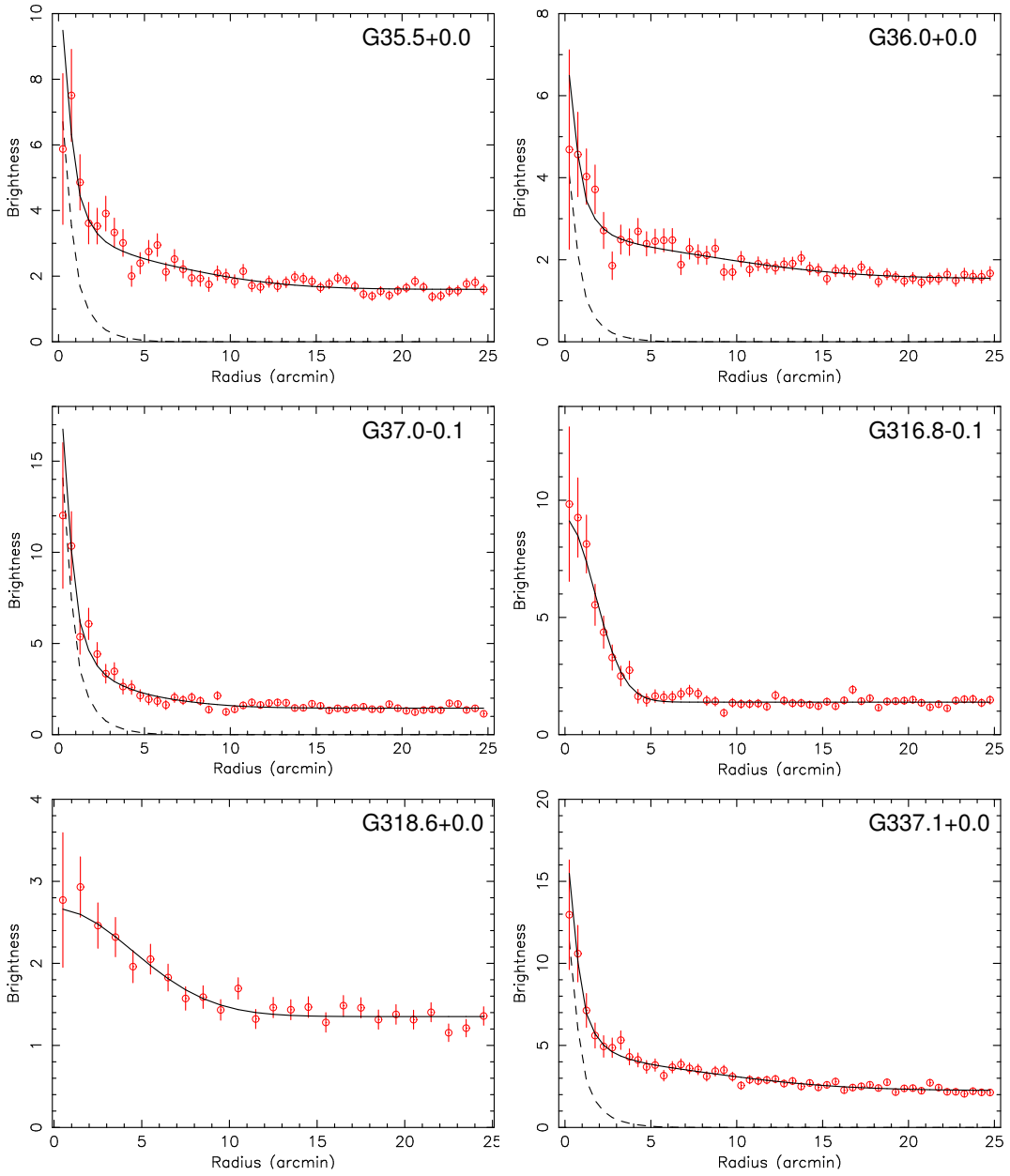

Figure 5.3: (Continued)

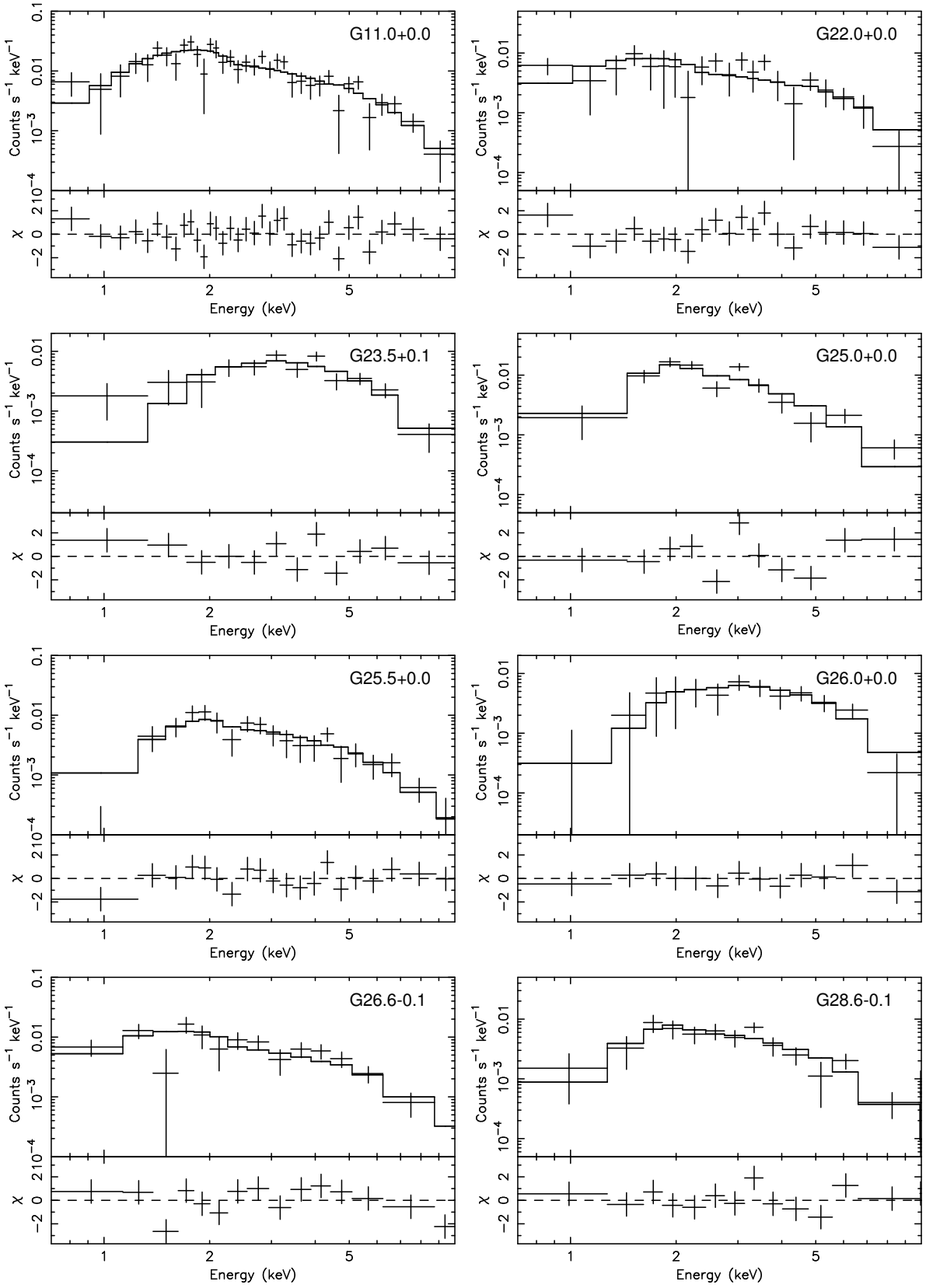

Figure 5.4: *ASCA* GIS spectra of the newly found SNR candidates. The best-fit power-law models are shown with solid-lines. The best-fit parameters are shown in Table 5.1

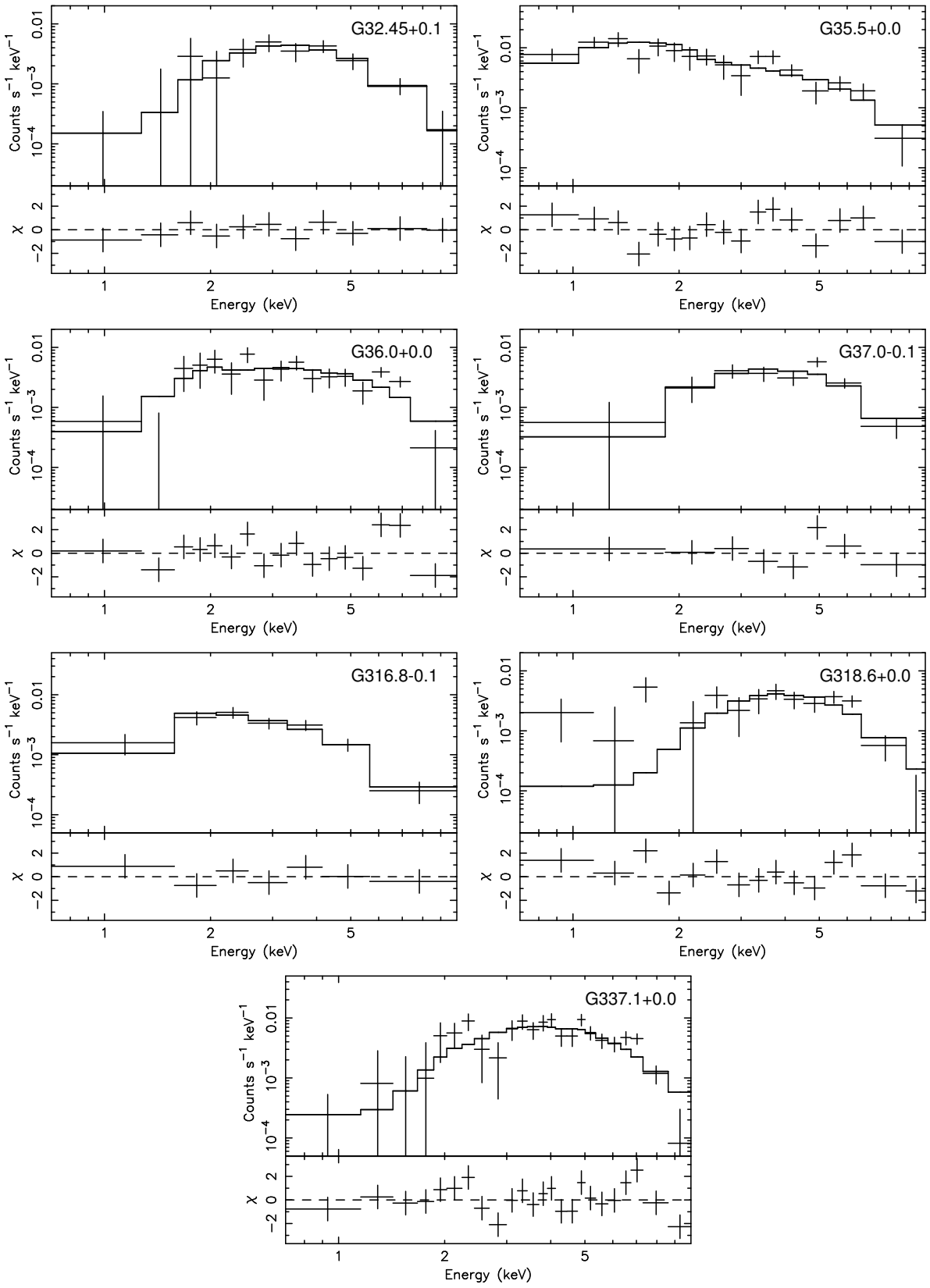

Figure 5.4: (Continued)

5.3 Comments on the individual sources

Characteristics of the individual sources are discussed in this section. Since sources listed in Table 6.1 except for G32.45−0.1 (G11.0+0.0, G25.5+0.0, G26.6−0.1, G28.6−0.1) are observed further with *ASCA*, *ASCA* results of these sources are discussed in the following sections.

G22.0+0.0

The spatial structures of G22.0+0.0 in the soft and hard X-ray bands are quite different. It was, however, impossible to make spectra spatially resolving the soft and hard components, because of the poor statistics and low spatial resolution of *ASCA*. This is likely to be the reason for the extremely low $N_{\rm H}$ obtained with the spectral fitting (Table 5.1). An observation with higher spatial resolution with enough statistics is required to determine the spectra of these components separately.

G23.5+0.1

The large absorption ($N_{\rm H} > 3.2 \times 10^{22}$ cm^2) of the X-ray spectrum indicates that G23.5+0.1 is located at distance of at least $\sim$ 10 kpc. For the discussion below, we estimate the lower limit of the X-ray luminosity. With the X-ray spectrum given, the smallest flux in the 0.5–10 keV band (6.1×10^{-12} ergs cm^{-2} s^{-1} within 90% error) corresponds to a combination of the smallest photon index and absorption within the error ranges ($\Gamma = 1.6$ and $N_{\rm H} = 3.2 \times 10^{22}$ cm^2, respectively). Then, on assumption of the 10 kpc distance, the lower limit of the X-ray luminosity is 3×10^{34} erg s^{-1} (0.5–10 keV).

A radio pulsar, PSR 1830−08 (Clifton & Lyne 1986), is located at (l, b) = (23.°39, 0.°06), inside G23.5+0.1. This pulsar is relatively active with spin-down luminosity of 6×10^{35} ergs s^{-1} and young (age $\sim 1 \times 10^5$ yr), and shows glitches (Clifton & Lyne 1986; Shemar & Lyne 1996). The *ASCA* point-source, AX J183345−0828, is located at 1.5 arcmin distance from this pulsar, and may be the counterpart (Sugizaki et al. 2001). A part or whole of the diffuse X-ray emission might be a pulsar-wind nebula created by this pulsar. If all the X-ray emission is powered by this pulsar, the effeciency with which the pulsar's spin-down is converted to the nebula X-ray is $L_X/\dot{E} = 0.5$. Though there is large uncertainty in the X-ray luminosity, this value is significantly larger than those of other pulsars (Becker & Truemper (1997)). Therefore, it is unlikely all of the X-ray emission of G23.5+0.1 is powered by PSR 1830−08.

A H II region with the radio flux of 2.6 Jy at 4.85 GHz is located at (l, b)=(23.°538, -0.°041) (Kuchar & Clark 1997). The X-ray emission may be originate from the associated

star-forming region, or a supernova of a massive star which evolved in the star-forming region.

G25.0+0.0

Since the X-ray emission around (l, b)=(25.°2, 0.°0) is very complicated with many point-like sources and extended structures, it is difficult to determine the spatial extent of each discrete source. This situation may be the reason for the complicated X-ray spectrum of G25.0+0.0; the spectrum leaves wavy residuals against the fitted power-law model and the model is rejected ($\chi^2_\nu/\nu = 22.9/8$). Spatially resolved observation is required for a disscussion on the origin of this extended X-ray emission.

G26.0+0.0

The highly absorbed ($N_{\rm H} \geq 2.1 \times 10^{22}$ cm^{-2}) X-ray spectrum suggests that G26.0+0.0 is at large distance ($\geq$ 5 kpc). Then, the physical diameter and the X-ray luminosity in the 2.0–10.0 keV band are $\geq$22 pc and $\geq 8.0 \times 10^{33}$ ergs $^{-1}$, respectively. Since no radio source in the NVSS data (Condon et al. 1998) spatially correlates well, G26.0+0.0 is not likely to be a H II region. When the spectrum is fitted with a thin thermal plasma model (APEC; Smith et al. 2001), the best-fit temperature is 3.8 (1.9–16.3) keV. Since this temperature is relatively high for a middle age SNR with $\sim$20 pc diameter, the X-ray emission may be non-thermal, such as synchrotron X-rays.

G32.45+0.1

We found a shell-like structure of 6′ diameter is located at the same position in the radio continuum image (1.4 GHz; Condon et al. 1998). Therefore, G32.45+0.1 is very likely to be an SNR. The X-ray spectrum of G32.45+0.1 is fitted well with deeply absorbed ($N_{\rm H} \geq 3 \times 10^{22}$ cm^{-2}) power-law model. Although the error range is large, the photon index of $\Gamma \sim 2.5$ reminds us of the non-thermal X-ray emissions from SN1006 and G347.3−0.5 (Koyama et al. 1995, 1997; Slane et al. 1999), the archetypal SNRs emitting synchrotron X-rays. Spatially resolved observation with *XMM-Newton* will be reported in §6.3.

G35.5+0.0

The point-like source at (l, b)=(35.°52, 0.°01), AX J185608+0218 (Sugizaki et al. 2001), is accompanied by extended emission also in the soft X-ray band (0.7–2.0 keV), though the extension ($\sim$6 diameter) is smaller than in the hard band. An extended hard X-ray emission with a point source on its center is typical of pulsar-wind nebulae. However, in pulsar-wind nebulae, X-ray emission ordinarily becomes softer as the distance from the center becomes larger, because of synchrotron loss. The G35.5+0.0 case conflicts with this. Spectral analysis

spatially resolving hard extended emission and AX J185608+0218 is required to reveal the origin, which could not be performed with the survey data due to poor statistics.

G36.0+0.0

The X-ray spectrum clearly shows excess around 6.0–7.0 keV against the fitted power-law model. When an emission line is added to the model, we obtained a much improved fit with $\chi^2_\nu/\nu = 8.6/12$. The center energy of the emission line was $6.43^{+0.15}_{-0.08}$ keV, indicating a K-line from low-ionized Fe. In this fitting the best-fit photon index and the absorption column density were $\Gamma = 1.9^{+1.1}_{-0.5}$ and $N_{\rm H} = 3.3(^{+1.5}_{-1.4}) \times 10^{22}$ cm^{-2}. Several SNRs have been reported to show emission lines from low-ionized Fe (Tycho's SNR, Kepler's SNR, RCW86, and G344.7−0.1; Hwang, Hughes, & Petre 1998; Kinugasa & Tsunemi 1999; Vink, Kaastra, & Bleeker 1997; Yamauchi et al. 2005).

The large absorption ($N_{\rm H} \geq 1.4 \times 10^{22}$ cm^{-2}) indicates G36.0+0.0 is located at distance of further than 4 kpc, and therefore the diameter is larger than ~ 20 pc. This physical size suggests G36.0+0.0 is an SNR similar to RCW 86 (28 pc diameter), rather than the young SNRs, Tycho and Kepler (5.4 and 2.5 pc diameters, respectively). If this analogy is the case, the hard X-ray emission of G36.0+0.0 may be synchrotron X-ray emission accompanied by a Fe-K line (Rho et al. 2002).

G37.0−0.1

The best-fit photon index obtained with the power-law model is consistent with this emission being synchrotron X-ray emission from a SNR. The large absorption column indicates, this source is at distance of ~ 10 kpc or further.

G316.8−0.1

G316.8−0.1 is also know as a H II region with several kinds of masers (e.g., OH and H_2O) and molecular lines (e.g, CO) (Shaver et al. 1981 and references therein). After extensive disussion on kinematic distance and other observations, Shaver et al. (1981) conclude the distance is 2.9 kpc.

The radio continuum emission (1415 MHz; Shaver et al. 1981) and the X-ray emission have good spatial correlation with sizes of $\sim 7'$. If the X-ray emission is due to the H II region, the spectrum is likely to be thermal. We also tried spectral fitting with a thin thermal plasma model (APEC; Smith et al. 2001), resulting in a statistically acceptable fit. The best-fit temperature and absorption column density are $3.1^{+5.1}_{-1.2}$ keV and $2.8(^{+1.7}_{-1.3}) \times 10^{22}$ cm^{-2}. The observed flux and the absorption-corrected luminosity at 2.9 kpc (0.7–10 keV) is 1.3×10^{-12} ergs cm^{-2} s^{-1} and 3.0×10^{33} erg s^{-1}, respectively. The tem-

perature and the luminosity is similar to those observed in other H II regions (e.g., W3 and NGC6334; Hofner & Churchwell 1997; Sekimoto et al. 2000). Therefore, the X-ray emission of G316.8−0.1 is likely to arise from the multiple young stars embedded in the H II region. Since the absorption column density is slightly large for the 2.9 kpc distance, intrinsic absorption by the associated molecular cloud would be significant.

G318.6+0.0

In the X-ray spectrum (Figure 5.4), we see an excess around 6.0 keV against the fitted power-law model. When an emission line is added to the model, χ^2_ν/ν is much improved to be 11.9/11 with the best-fit center energy of the line $5.9^{+0.2}_{-0.2}$ keV. Since no atomic line of any abundant element corresponds to this energy, this line is likely to be a red-shifted Fe K-line from a cluster of galaxies with $z \sim 0.14$. In this case, the X-ray luminosity in the 2.0–10 keV is calculate to be $\sim 2 \times 10^{44}$ ergs s^{-1} ($H_0 = 50$ km Mpc^{-1}). According to the relation between temperature and X-ray luminosity of clusters of galaxies (Arnaud & Evrard 1999), a cluster with this luminosity is expected to have ∼3–4 keV temperature, which is consistent with the hardness of the spectrum. The large absorption column ($N_{\rm H} > 4.1 \times 10^{22}$ cm^{-2}) is also consistent with that G316.8+0.0 is located behind the Galactic plane.

G337.1+0.0

In the X-ray spectrum (Figure 5.4), a line-like excess against the best-fit power-law model is seen around 6.7 keV, which suggests the emission is due to a thin thermal plasma. When fitted with a thin thermal model (APEC; Smith et al. 2001), χ^2_ν was much improved ($\chi^2_\nu/\nu = 20.5/21$), with the best-fit temperature and absorption column of $kT = 6.8^{+6.0}_{-3.3}$ keV and $N_{\rm H} = 7.0(^{+3.3}_{-2.6}) \times 10^{22}$ cm^{-2}. If we assume the average density of the ISM on the line of sight is $n_{\rm H} = 1$ cm^{-3}, the distance is estimated to be at least 11 kpc. Then, the physical diameter is at least 48 pc.

An radio SNR candidate, G337.2+0.1, listed by Whiteoak & Green (1996) is located nearby at (l, b) = (337.°18, 0.°06). Since the size of G337.2+0.1 is $3' \times 2'$, and is slightly smaller than the X-ray source G337.1+0.0, a part of G337.1+0.0 might have been enhanced and detected in the radio band.

5.4 Summary of the Extended Source Survey

(1) We searched extended X-ray sources in the hard band image of the *ASCA* Galactic Plane Survey.

(2) As a result, we found 15 unidentified extended sources.

(3) Many sources (11 sources) are deeply absorbed $N > 10^{22}$ cm^{-2}, and suggests they are distant ($\sim$ 10 kpc).

(4) G316.8−0.1 is identified with a H II region.

(5) G318.6+0.0 may be a cluster of galaxies located behind the Galacitc plane, which is suggested by a line emission around 5.5 keV.

(6) Follow-up observations with higher spatial resolution and rich statistics are required for all the candidates to establish their origin.

Chapter 6

Follow-up Observations of the New *ASCA* Sources

Since the data set of the *ASCA* Galactic Plane Survey is limited in statistics and spatial resolution, we performed follow-up observations with *ASCA*, *Chandra*, and *XMM-Newton* as shown in Table 6.1.

Table 6.1: Follow-up observations on the SNR candidates

Target	*ASCA*[a] (ks)	*CXO* (ks)	*XMM* (ks)	results
G11.0+0.0	49	-	-	?
G25.5+0.0	50	-	-	?
G26.6−0.1	45	(20)[b]	-	?
G28.6−0.1	81	100	-	SNR
G32.45+0.1	10	-	27	SNR

[a] Including the exposures of the *ASCA* Galactic Plane Survey.
[b] Observed with *Chandra*, but the data is not archived.

6.1 Follow-ups of G11.0+0.0, G25.5+0.0, and G26.6−0.1

6.1.1 Observations and Images

In order to study spatial and spectral characteristics, we performed *ASCA* follow-up observations on G11.0+0.0, G25.5+0.0, and G26.6−0.1 for longer exposures than the galactic

Table 6.2: *ASCA* observations performed on G11.0+0.0, G25.5+0.0, and G26.6−0.1

Obs. Id	Date yyyy/mm/dd	Pointed Direction (R.A., Dec.)$_{J2000}$	Exposure (ksec)	Observation Type	Observation Number
54005000	1996/08/04	($18^h09^m50\overset{s}{.}4$, $-19°24'40''$)	10.3	Survey	1
57027000	1999/09/28	($18^h09^m36\overset{s}{.}0$, $-19°27'08''$)	39.0	Follow-up	2
55002090	1997/10/14	($18^h37^m48\overset{s}{.}0$, $-06°36'42''$)	12.4	Survey	3
57029000	1999/09/26	($18^h37^m45\overset{s}{.}6$, $-06°36'43''$)	37.3	Follow-up	4
55004010	1997/04/20	($18^h39^m43\overset{s}{.}2$, $-05°42'58''$)	9.8	Survey	5
57026000	1999/10/03	($18^h40^m14\overset{s}{.}4$, $-05°40'44''$)	35.9	Follow-up	6

plane survey. The observation dates and the on-axis positions are summarized in Table 6.2.

We screened the GIS data using the standard procedures with a little different criteria shown in §3.1.2; the thresholds for the cutoff rigidity and the elevation angle for selected events were set to be COR > 6 (GV) and ELV > 10 (°), respectively, and screening for SFR and HFR were not performed. The resultant exposures after these screenings are shown in Table 6.2.

The GIS images in the 0.7–7.0 keV band around the SNR candidates are shown in Figure 6.1. The diffuse structures discovered in the *ASCA* Galactic Plane survey are clearly seen in those images. Weak point-like sources 1, 7, and 12 are detected in G11.0+0.0, G25.5+0.0, and G26.6−0.1, respectively. We also checked the *ROSAT* and *Einstein* point-source catalogs and found only one source, 1RXS J184049.1−054336 in G26.6−0.1 (at the same position as source 12) within $15'$ radius regions around the diffuse sources.

6.1.2 Spectral Analysis

For the spectral analyses, we combined the survey and the follow-up observation data: Observation 1 and 2 for G11.0+0.0, Observation 3 and 4 for G25.5+0.0, and Observation 5 and 6 for G26.6−0.1 (see Table 6.2). The spectra were made using the events in the circular regions of $15'$ diameter for G11.0+0.0, and $12'$ diameter for both G25.5+0.0 and G26.6−0.1, respectively (*solid-line circles* in Figure 6.1). X-ray events of point source 1 for G11.0+0.0, 7 for G25.5+0.0, and 12 for G26.6−0.1 were excluded from the spectra by neglecting circular regions of $3'$ around these sources. In order to properly subtract the Galactic ridge X-rays (Koyama, Makishima, Tanaka, & Tsunemi 1986; Kaneda et al. 1997), the background

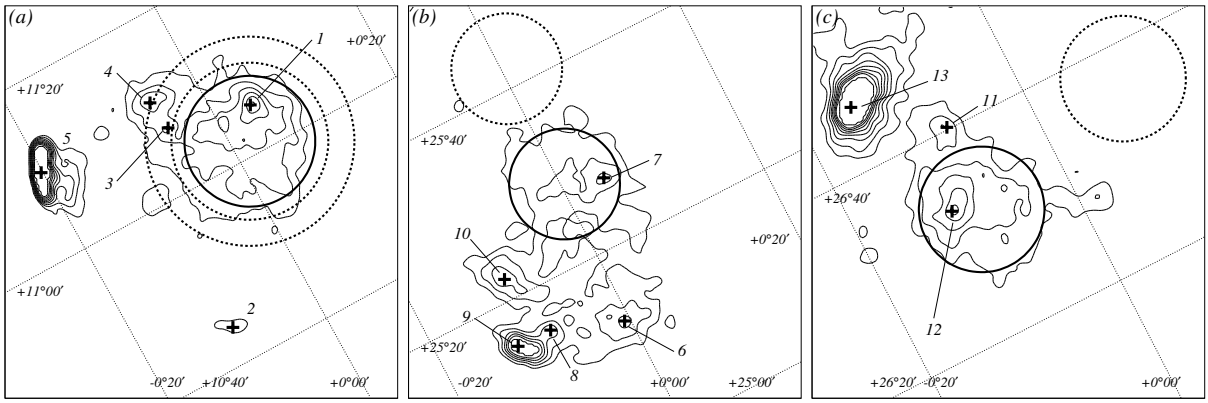

Figure 6.1: GIS images with Galactic coordinate around (a)G11.0+0.0, (b)G25.5+0.0, and (c)G26.6−0.1 in the 0.7–7.0 keV band, where exposure time and vignetting effect are corrected. The images are smoothed with a Gaussian profiles of $\sigma = 0'.5$. The contour levels are linearly spaced with 6.4×10^{-4} counts arcmin^{-2} s^{-1} interval from the lowest level of 1.9×10^{-3} counts arcmin^{-2} s^{-1} for G11.0+0.0, 1.5×10^{-3} counts arcmin^{-2} s^{-1} for G25.5+0.0, and 2.4×10^{-3} counts arcmin^{-2} s^{-1} for G26.6−0.1. For bright point sources, the higher contour levels are truncated. The source and background regions for the spectral analysis (see text) are shown with the solid and dashed-line circles. The crosses indicate the position of point-like sources.

spectra were extracted from the source-free regions near the targets within the same FOVs, and at the same distance from the Galactic plane as the source region. For the background of G11.0+0.0, we selected the annular region between $18'$ and $24'$ diameter, but excluded circular regions of $12'$ diameter around sources 3 and 4.

The background-subtracted spectra are shown in Figure 6.2. We see relatively flat spectra and no line feature. Those spectra were fitted with two models of a thin thermal plasmas in nonequilibrium ionization (NEI; Borkowski et al. 2001b) and a power-law model. Both of these models are statistically acceptable for all the spectra, with the best-fit parameters shown in Table 6.3. The best-fit power-law models are shown in Figure 6.2 (*solid-line*).

6.1.3 Discussion

On assumption that the average density in the Galaxy toward the inner disk is $n_{\rm H} = 1$ cm^{-3}, we estimated the distances using the best-fit absorption column densities. The results are listed in Table 3 together with the physical diameters and X-ray luminosities. We used the best-fit parameters with the power-law models (Table 6.3), whereas using those with the

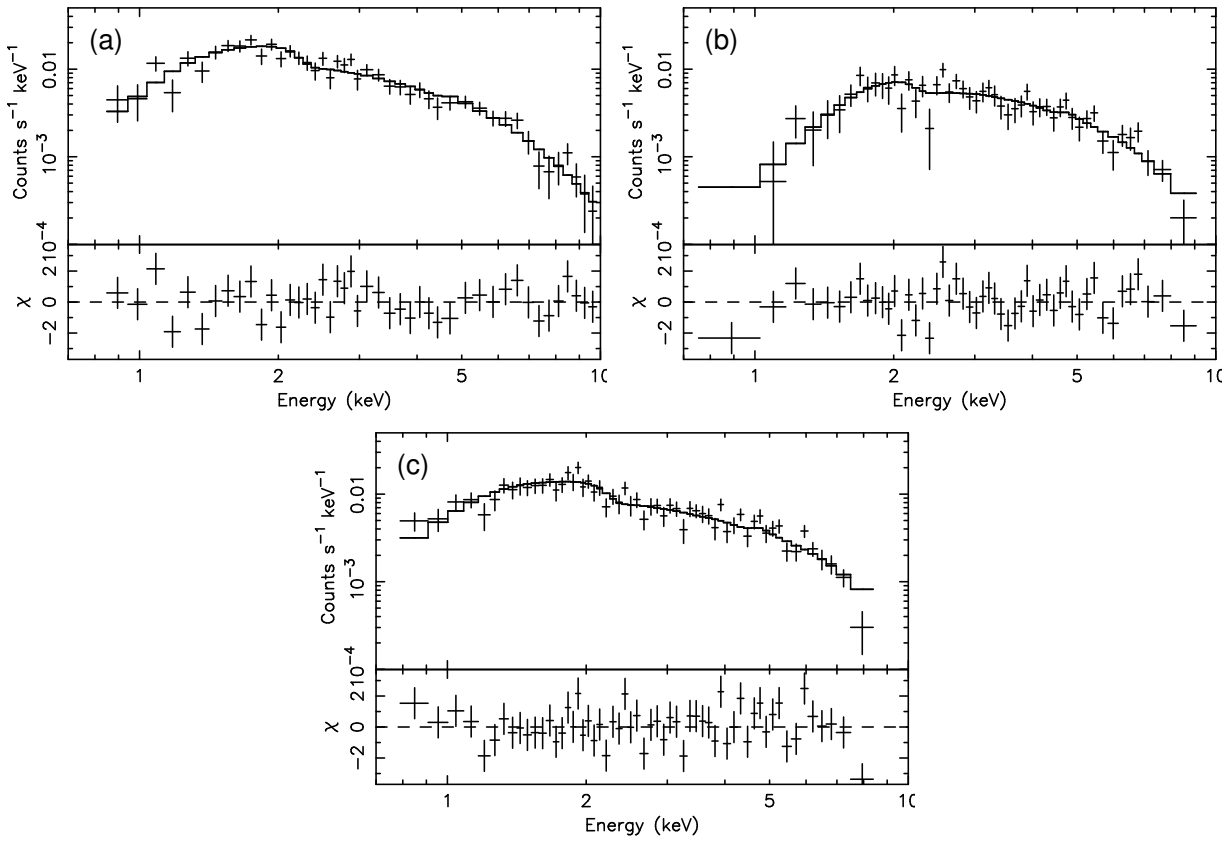

Figure 6.2: Background-subtracted spectra (*crosses*) of (a) G11.0+0.0, (b) G25.5+0.0, and (c) G26.6−0.1. The spectra of GIS 2 and 3 are combined. The best-fit power-law models (Table 6.3) are designated with solid-lines.

NEI model makes no essential difference.

Counterparts in other wavelengths

In order to discuss the origins of the extended X-ray emissions of G11.0+0.0, G25.5+0.0, and G26.6−0.1, we first looked for counterparts in other wavelengths using the SIMBAD database.

In the region of G11.0+0.0, a radio young pulsar, PSR 1809−1917, was found in the north (Morris et al. 2002), whose position corresponds to source 1. This pulsar is relatively powerful with spin-down luminosity of 2×10^{36} ergs s^{-1}. If all the X-ray emission of G11.0+0.0 is powered by this pulsar, the efficiency with which the pulsar's spin-down is converted into nebular X-ray is $L_X/\dot{E} = 1.9 \times 10^{-3}$. This value is typical for young pulsars (Becker & Truemper 1997). Therefore, significant fraction of X-ray emission from G25.5+0.0 may be

Table 6.3: Best-fit Spectral Parameters of G11.0+0.0, G25.5+0.0, and G26.6−0.1

Parameter	G11.0+0.0	G25.5+0.0	G26.6−0.1
Power-law Model:			
Photon Index	1.6 (1.4–1.9)	1.8 (1.6–2.2)	1.3 (1.2–1.5)
$N_{\rm H}(10^{22}$ cm$^{-2})$	0.8 (0.5–1.1)	2.4 (1.8–3.2)	0.4 (0.2–0.6)
Flux[a] (ergs cm^{-2} s^{-1})	3.8×10^{-12}	2.0×10^{-12}	3.5×10^{-12}
χ^2/degrees of freedom	44.2/42	55.4/48	73.2/55
srcut model[b]:			
Break frequency ($\times 10^{19}$Hz)	3.2 (> 0.4)	0.4 (0.07–36)	1.3×10^3 (> 12)
Flux density[a] (mJy)	9.0 (8.4–9.6)	9.6 (8.8–11)	5.6 (5.2–5.9)
$N_{\rm H}$ (10^{22} cm^{-2})	0.8 (0.6–0.9)	2.3 (2.0–2.7)	0.6 (0.4–0.7)
χ^2/degrees of freedom	45.3/42	55.3/48	75.6/55
NEI model:			
kT (keV)	11.5 (7.3–21.0)	7.1 (4.5–14.0)	14.5 (8.7–34.8)
Abundance	0.7 (0.1–1.8)	0.4 (0.1–0.7)	0.5 (0.1–1.1)
$n_{\rm e}t$ (10^9 s cm^{-3})	0.9 (< 4.2)	3.2×10^2 (> 58)	5.1 (3.0–9.1)
$N_{\rm H}(10^{22}$ cm$^{-2})$	0.6 (0.4–1.1)	2.3 (1.8–3.0)	0.9 (0.5–1.4)
Flux[c] (ergs cm^{-2} s^{-1})	3.8×10^{-12}	2.0×10^{-12}	3.4×10^{-12}
χ^2/d.o.f.	42.7/40	63.5/53	31.1/45

[a] Absorbed flux in the 0.7–10.0 keV band. [b] The radio spectral index is fixed to 0.5. [c] At the 1 GHz band.

Table 6.4: Physical Parameters of the Diffuse Sources

Parameter	G11.0+0.0	G25.5+0.0	G26.6−0.1
Distance[a](kpc)	2.6	7.8	1.3
Diameter (pc)	11	27	4.5
Luminosity[b] (ergs s^{-1})	3.7×10^{33}	2.3×10^{34}	8.1×10^{32}

[a] Calculated from the best-fit absorption column in Table 6.3 assuming the mean density in the Galactic plane is 1 cm^{-3}.

[b] Absorption-corrected luminosity in the 0.7–10.0 keV.

powered by this pulsar. However, the X-ray emission is spatially asymmetric with respect to the pulsar. We need X-ray observation with higher spatial resolution to conclude what fraction of the G25.5+0.0 can be explained by the pulsar.

H II regions were found within all the three sources; G10.9+0.1 and G11.0+0.0 in G11.0+0.0, G25.4+0.0 in G25.5+0.0, and G26.6−0.1 in G26.6−0.1 (Kuchar & Clark 1997; Note several names of the H II regions are the same as the X-ray sources). However, since their spatial sizes are significantly smaller than those of the X-ray emissions, these H II regions are not likely to be the direct power source of the X-ray, although a supernova originating these H II regions may be the power source.

Thermal Emission Scenario

The high temperatures derived with the NEI models indicate G11.0+0.0, G25.5+0.0, and G26.6−0.1 are very young SNRs. On assumption of a uniform density plasma sphere, we estimate the emission measures (EM), dynamical times (t =radius/sound velocity), electron densities (n_e), total masses (M), and thermal energies (E), which are listed in Table 6.5.

We find that total masses of G11.0+0.0 and G26.6−0.1 are only a few times solar, consistent with young SNRs. However, the thermal energies are significantly smaller than the canonical explosion energy of a supernova (1×10^{51} ergs). Therefore, only a small fraction of explosion energy must be converted to the thermal energy; hence, they may be in the free expansion phase. In this case, the X-ray emitting plasma is attributable to the supernova ejecta with large metallicity, but the observations show no such large abundance. Thus, thermal X-ray emissions from young SNRs are not likely the case for G11.0+0.0, and G26.6−0.1.

For G25.5+0.0, the physical parameters are consistent with the adiabatic phase SNR; however, the plasma density (< 0.1 H cm^{-3}) is much smaller than that of the interstellar gas in the Scutum arm. We thus regard that a thermal SNR for this diffuse source is also unlikely.

SN 1006-like case

We discuss the possibility that they are SN 1006-like SNRs. Photon indices of G11.0+0.0 and G25.5+0.0 are ~ 2, which are smaller than those of typical SN 1006-like SNRs, SN 1006 itself, G347.3−0.5, and G266.2−1.2. This may indicate that the synchrotron cut-off energy of electrons is higher in G11.0+0.0 and G25.5+0.0 than in those typical SN 1006-like SNRs.

In order to establish the SN 1006-like SNRs, the presence of synchrotron radio emis-

Table 6.5: Parameters for thermal plasma scenario.

Parameter	G11.0+0.0	G25.5+0.0	G26.6−0.1
Emission measure EM[a] (cm^{-3})	2.3×10^{56}	1.5×10^{57}	4.9×10^{55}
Dynamical time t[b] (s)	1.3×10^{11}	3.9×10^{11}	4.7×10^{10}
Electron density n_e (cm^{-3}) ...	0.11	0.070	0.18
Total mass M ($M_\odot$)	1.8	18	2.3
Thermal energy E[c] (ergs).....	1.2×10^{50}	7.3×10^{50}	1.9×10^{49}

[a] Emission measure $n_e V^2$, where n_e is the electron density and V is the plasma volume.

[b] The ratio of the radius to the sound velocity.

[c] $E = (3/2)(n_i + n_e)VkT$, where n_i is the proton density.

sion is essential. However, no cataloged radio source is found in the NVSS archival data (1.4 GHz; Condon et al. 1998). In order to estimate the radio flux for the case of SN 1006-like SNRs, we tried spectral fitting with a SRCUT model (Reynolds 1998; Reynolds & Keohane 1999). The spectral index at 1 GHz was frozen to $\alpha = 0.5$, the expected value by the first-order Fermi acceleration. The fittings were statistically acceptable, and the best-fit parameters are listed in Table 6.3. We also tried the same fitting with $\alpha = 0.6$ and found no essential difference in the best-fit parameters. The best-fit flux density for each source suggests that the expected surface brightness at 1 GHz is 9.8×10^{-24}, 1.7×10^{-23}, and 9.8×10^{-24} W m^{-2} Hz^{-1} sr^{-1} for G11.0+0.0, G25.5+0.0, and G26.6−0.1, respectively. On the other hand, the minimum surface brightness of the cataloged radio SNRs in our survey field is 2×10^{-21} W m^{-2} Hz^{-1} sr^{-1} (for G3.8+0.3; Case & Bhattacharya 1998), which is similar to SN 1006 (3×10^{-21} W m^{-2} Hz^{-1} sr^{-1}; Long et al. 1988; Winkler & Long 1997) and G347.3−0.5 (4×10^{-21} W m^{-2} Hz^{-1} sr^{-1}; Ellison et al. 2001; assuming $\alpha = 0.5$), but is two or three orders of magnitude larger than our new sources. Even the minimum surface brightness of the all cataloged radio SNRs is larger than our sample, 6.2×10^{-23} W m^{-2} Hz^{-1} sr^{-1} (for G156.2+5.7; Case & Bhattacharya 1998). Therefore, no radio counterpart for our new X-ray sources would be simply due to limited detection threshold of the current radio observations. Therefore, no radio counterpart of our new X-ray sources would be simply due to limited detection threshold of the current radio observations.

Crab-like case

The power-law spectra and the luminosities (10^{34}–10^{35} ergs s^{-1}) suggest that the new sources are also Crab-like (plerionic) objects. We also discuss no detection of radio source in this case. The luminosity ratio between the radio and X-ray band is largely different among

the plerionic SNRs: for example, the radio luminosity of 3C58 is about 10 times smaller, while that of X-ray is about 1000 times smaller than that of the Crab Nebula (Hands et al., 2001). We estimated the expected surface brightness using the flux density of 3C58 and the Crab Nebula (Green, 2004). For the 3C58-like case, the surface brightness of G11.0+0.0, G25.5+0.0, and G26.6−0.1 at 1 GHz is expected to be 2.5×10^{-20}, 5.1×10^{-20}, and 1.9×10^{-20} W m^{-2} Hz^{-1} sr^{-1}, respectively. Since these values are larger than the detection limit in the surveyed region (see previous paragraph), we exclude the 3C58-like case. On the other hand, for the Crab-like case, their respective surface brightness becomes to be 7.3×10^{-23}, 1.5×10^{-22}, and 5.6×10^{-23} W m^{-2} Hz^{-1} sr^{-1}. Therefore, a possibility of the Crab-like case can not be excluded.

6.2 *ASCA* and *Chandra* Follow-up of G28.6−0.1

6.2.1 Follow-up Observations with *ASCA*

G28.6−0.1 was observed with *ASCA* twice other than the ASCA Galactic plane survey (Table 6.6). One of which was performed for the study of the Galactic Ridge Emission (Kaneda et al. 1997), and the other one was for a follow-up observation of G28.6−0.1 itself. In total, 81 ks observations were performed on G28.6−0.1. The exposure-corrected smoothed image is shown in Figure 6.3. Spatially extended X-rays with an elliptical shape is evident especially in the hard band (2.0–7.0 keV), and the extended structure seen in the survey data is confirmed.

The X-ray spectrum was extracted using the photons in an elliptical area of $13' \times 9'$ (the inner ellipse in Figure 6.3), whereas the background spectrum was obtained from an elliptical ring around the source (between the outer and inner ellipses in Figure 6.3). The background-subtracted spectrum is shown in Figure 6.4. The spectrum is hard and without conspicuous structure of lines. In order to find out the origin of this X-ray emission, we fit the spectrum with two models of a power-law and a thin thermal plasma in non-equilibrium ionization (NEI; Masai 1984; Borkowski et al. 2001b). As a result, both of these models were statistically acceptable with the best-fit parameters and the best-fit models shown in Table 6.7 and Figure 6.4, respectively.

The best-fit $N_{\rm H}$ value $(2.6-4.0)\times10^{22}$ cm^{-2} is consistent with that obtained with the survey data. This value is similar to the nearby SNRs, Kes 73 [$(1.6-2.3)\times10^{22}$ cm^{-2}; Gotthelf & Vasisht (1997)] and Kes 75 [$(2.9\pm0.4)\times10^{22}$ cm^{-2}; Blanton & Helfand (1996)] at ($27\overset{\circ}{.}4$, $0\overset{\circ}{.}0$) and ($29\overset{\circ}{.}7$, $-0\overset{\circ}{.}3$), respectively. Using the H I absorption data, the distances of

Table 6.6: *ASCA* observations performed on G28.6−0.1.

Obs. Id	Date	Pointed Direction	Exposure
	yyyy/mm/dd	(R.A., Dec.)$_{J2000}$	(ksec)
90006000	1993/10/22	($18^h44^m40\overset{s}{.}7$, $-03°36'14''$)	19
55004050[a]	1997/04/22	($18^h42^m38\overset{s}{.}2$, $-04°09'13''$)	10
57028000	1999/03/23	($18^h43^m10\overset{s}{.}4$, $-04°03'06''$)	42

[a] This observation is a part of the *ASCA* Galactic Plane Survey.

Kes 73 and Kes 75 are estimated to be 6–7.5 kpc (Sanbonmatsu & Helfand 1992) and 9–21 kpc (Caswell et al. 1975; Becker & Helfand 1984), respectively. Koyama et al. (1990) found many transient sources at the tangent point of the Scutum arm (about 8.5 kpc) with absorptions of around 10^{23} cm^{-2}, which are larger than that of G28.6−0.1 Accordingly, we infer that the distance of G28.6−0.1 is in between 6–8.5 kpc. Hereafter, we assume the distance to be 7 kpc. The X-ray luminosity (0.1–10 keV) and the source size (the mean diameter) are then estimated to be 3×10^{34} ergs s^{-1} and 20 pc, respectively. These parameters are similar to those of shell-like young SNRs.

The high temperature of ∼5 keV corresponds to the shock speed of ∼2000 km s^{-1} and is also consistent with that G28.6−0.1 is a young SNR. The high speed shock indicates that the swept-up mass is not very large and if we assume the explosion energy is 1×10^{51} ergs, the mass is estimated to be $4M_\odot$. Since this value is comparable to the ejected mass, the abundance is expected to be very high with prominent emission lines, which can be seen in most of the young SNRs, such as Cas A, Tycho's SNR, and Kepler's SNR (Holt et al. 1994; Hwang, Hughes, & Petre 1998; Kinugasa & Tsunemi 1999). However, the abundance of G28.6−0.1 with the NEI model is only ∼1 solar. Therefore, it is difficult to attribute the hard and featureless X-ray spectrum of G28.6−0.1 to thermal emission. Thus, we expect the emission from this remnant to be non-thermal. The luminosity is almost consistent with that of the non-thermal component of SN 1006 (∼ 2×10^{34} ergs s^{-1}; Dyer, Reynolds, & Borkowski 2004) and the diameter is similar to SN 1006.

6.2.2 *Chandra* Observations of G28.6−0.1

The *ASCA* observations suggested that G28.6−0.1 is an SNR emitting non-thermal X-rays. However, two other possibilities remained; this source may be a collection of point sources or the origin of the X-ray emission may be thermal plasma in non-equilibrium ionization. In order to exclude these possibilities by resolving point sources and a putative thermal

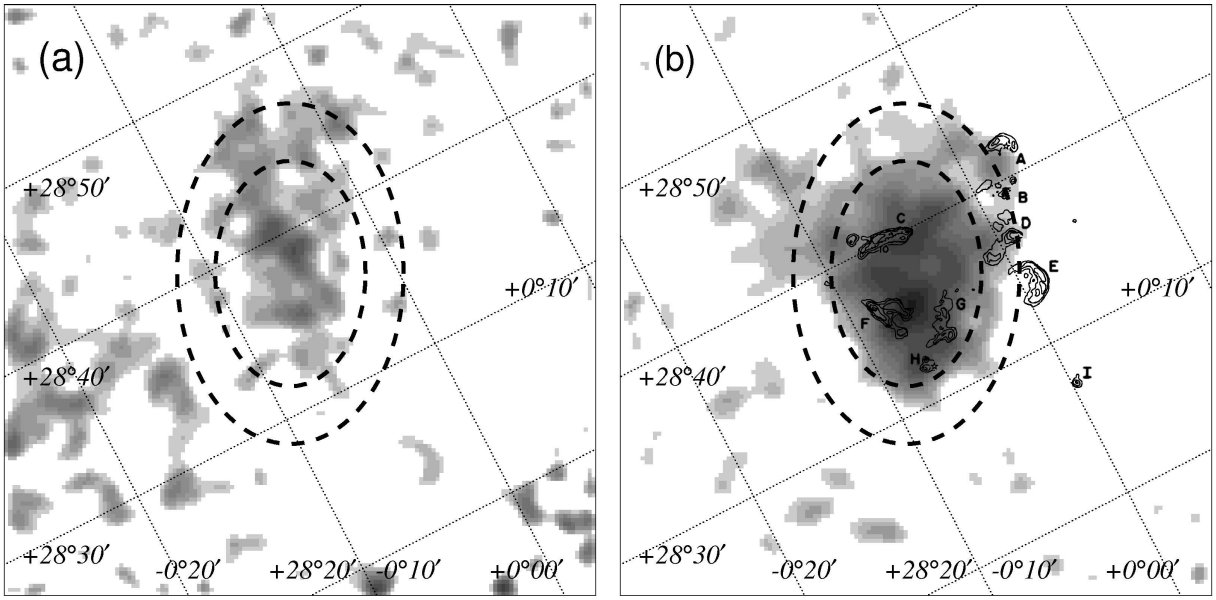

Figure 6.3: ASCA GIS images in the 0.7–2.0 keV (a) and 2.0–7.0 keV (b) bands. The VLA 20 cm radio contours by Helfand et al. (1989) are superposed on the 2.0–7.0 keV image (b). The ASCA images are corrected for the exposure and smoothed with a Gaussian kernel of $\sigma = 75''$. The source and the background regions for the spectrum are shown with broken-line ellipses.

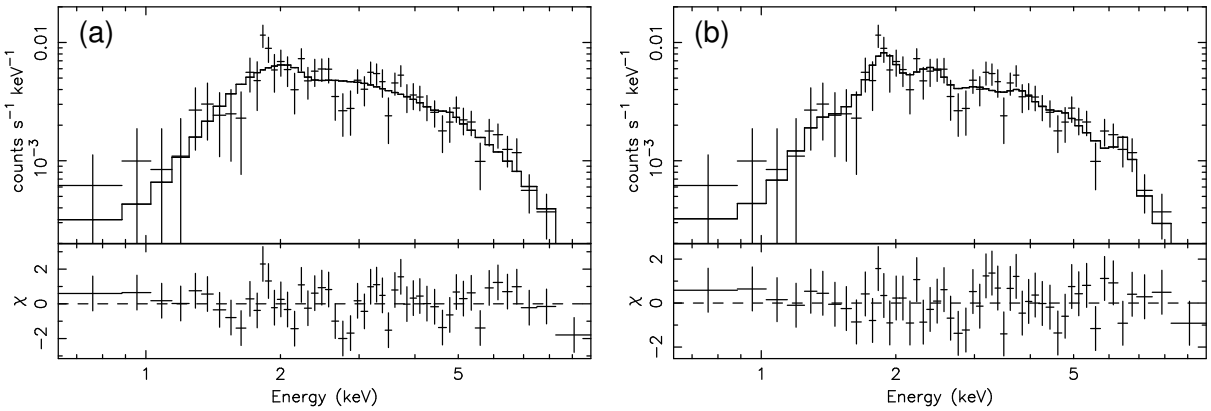

Figure 6.4: Background-subtracted spectrum of the combined GIS2 and 3 data of the 3 observations. The solid lines represent the best-fit power-law model (a) and the best-fit NEI model (b).

Table 6.7: Best-fit parameters of G28.6−0.1 for a power-law and a thin thermal plasma model with the *ASCA* observations*.

Model	Γ / kT .../(keV)	Abundance†	$\log n_e t$ (s cm^{-3})	N_H (10^{22} cm^{-2})	χ^2 /d.o.f.
power-law.....	$2.1^{+0.3}_{-0.4}$	...	...	$2.6^{+0.8}_{-0.6}$	45.7/47
thin thermal plasma	$5.4^{+3.4}_{-1.8}$	$1.5^{+1.9}_{-1.2}$	$9.6^{+0.3}_{-0.3}$	$4.0^{+1.8}_{-1.2}$	32.5/46

* Errors and upper-limits are at 90% confidence for one relevant parameter.

† Assuming the solar abundance ratio (Anders & Grevesse 1989).

component, we performed X-ray observations with the high spatial resolution of *Chandra*.

Observations and Data Reduction

The *Chandra* deep observations on the G28.6−0.1 region were performed on 2000 February 24–26 (here observation 1) and on 2001 May 20–21 (here observation 2). The targeted positions are R.A. = $18^h43^m57^s.8$, decl. = $-04°04'45''.9$ (epoch 2000) and R.A. = $18^h43^m32^s.1$, decl. = $-03°54'44''.8$ (epoch 2000) for observation 1 and 2, respectively. The observation regions were $17' \times 17'$ fields of the ACIS-I arrays.

G28.6−0.1 lies near the northwest edge and the east part of the ACIS-I array, for observation 1 and 2, respectively. Data acquisition from ACIS-I was made in Timed-Exposure Faint mode with the chip readout times of 3.24 s. Data reduction and analysis were made using the *Chandra* Interactive Analysis of Observations (CIAO) software version 2.2. Using Level 2 processed events provided by the pipeline processing at the *Chandra* X-ray Center, we selected the *ASCA* grades 0, 2, 3, 4 and 6, as X-ray events. The other events due to charged particles and/or hot and flickering pixels were removed. We also removed high background data in the observation 1 where total count rates were larger than 5.5 counts s^{-1}. The effective exposures were then about 94 ks and 99 ks for observation 1 and 2, respectively.

Over-all Morphology

In the raw images obtained by these observations, we see numerous point sources. We at first picked up point sources from the raw images in the energy bands of 0.5−3.0 keV, 3.0−8.0 keV, and 0.5−8.0 keV using the program *wavdetect* (Freeman et al. 2002) with the significance criterion at 4.0σ, which corresponds to about 6 – 33 counts s^{-1}, depending on the size of the point-spread function (PSF), the energy band, and the background level. Then 274 sources are found in the two observations, of which 225, 116, and 271 are detected in the energy

bands of 0.5−3.0 keV, 3.0−8.0 keV, and 0.5−8.0 keV, respectively. Surface density of the point sources detected in the 3.0−8.0 keV band is not significantly higher than that expected from the extragalactic sources seen through the Galactic plane. Therefore, most of the hard X-ray sources are considered to be extragalactic (Ebisawa et al. 2001). On the other hand, soft X-ray point sources show significant excess over the extragalactic population. They have low temperature (< 1 keV) thermal spectra and some of them exhibit flare-like temporal variations (Ebisawa et al. 2002). Therefore, most of these soft X-ray sources are presumably nearby active stars.

The combined image (observation 1 + 2), after the exposure correction and smoothing with a Gaussian kernel of $\sigma = 6''$ is shown in Figure 6.5, where the point sources of $> 5.0\sigma$ detection in the 0.5−8.0 keV band are given by crosses. In Figure 6.5, we can see an extended complex at the north (shown by the solid-line ellipse). Since the point sources are scattered uniformly over the field of view, the extended X-ray structure is unlikely to be a local enhancement of many point sources, but will be a really diffuse source. The center position of the diffuse source is at around R.A. = $18^{\rm h}43^{\rm m}50^{\rm s}$, decl. = $-03^\circ52'00''$ (epoch 2000) and the emission is extended in the elliptical shape of $11' \times 7\farcm5$.

We found that G28.6−0.1 consists of numerous clumps. We name the brightest spherical clump in the south-eastern part of G28.6−0.1 as CXOU J184357−035441 from its central position (Although this source is designated as "CXO J184357−035441" in Ueno et al. (2003), "CXOU J184357−035441" fits the *Chandra* source naming convention). A closed-up view of this clump in the 1.0–6.0 keV band is shown in Figure 6.6, together with the 20 cm (1.5 GHz) contour of a radio source F (Helfand et al. 1989). A notable feature is its peculiar shape: an elliptical head with a jet-like tail $30''$ long to the southeast.

The spatial correlation between the diffuse X-ray and radio is demonstrated by the 20 cm VLA contours in Figure 6.5, with the designation of the radio source (A–I) given by Helfand et al. (1989). The X-ray emission consists of many clumps filling an ellipse, which is partly outlined by the radio sources C and F, the SNR candidates proposed by Helfand et al. (1989). The south tail of the radio source G is also correlated with the X-ray enhancement. Though the source H is said to be extragalactic because of its infrared emission (Helfand et al. 1989), it is also inside G28.6−0.1 and may be associated. Note, however, no significant X-ray emission is associated with the source E, which is a partial radio shell and an SNR candidate suggested by Helfand et al. (1989).

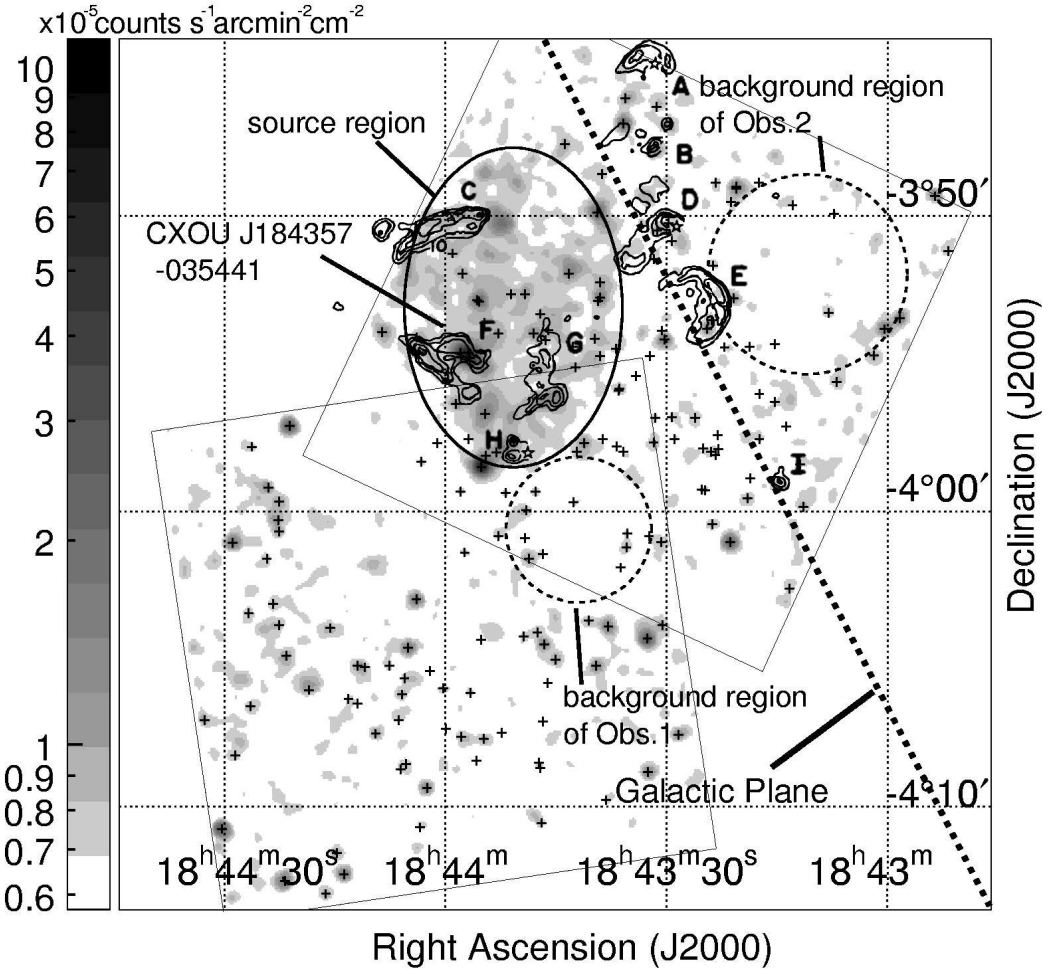

Figure 6.5: Combined ACIS-I image of observation 1 and observation 2 in the 1.5–8.0 keV band overlaid with the VLA 20 cm radio contours by Helfand et al. (1989). The X-ray image is corrected for the exposure, smoothed with a Gaussian kernel of $\sigma = 6''$, and plotted from 5.7×10^{-6} to 1.1×10^{-4} counts cm^{-2} s^{-1} arcmin^{-2} in logarithmic scale. Plotted are FOVs of observations 1 and 2 (*large squares*), G28.6−0.1 source region(*ellipse*) and background region (*circles*), and point sources detected by the *wavdetect* software with significance greater than 5.0σ (*plus signs*). Radio sources are labeled following Helfand et al. (1989).

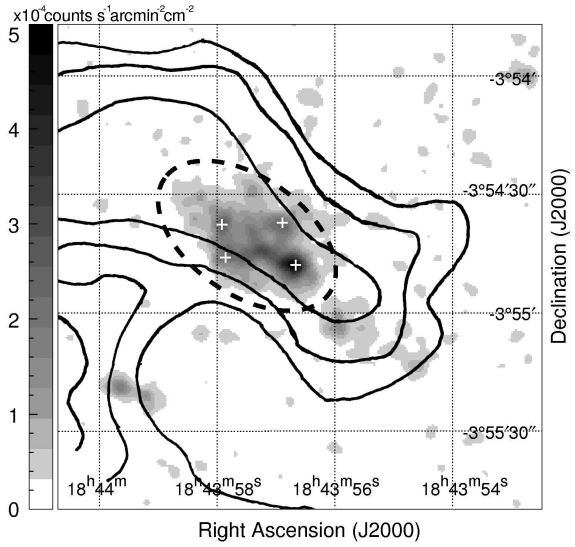

Figure 6.6: Close-up view of CXOU J184357−035441 in the energy band 1.0–6.0 keV. The image is smoothed with a Gaussian kernel of $\sigma = 1\overset{s}{.}5$. Shown are the 20 cm radio continuum source F (Helfand et al. 1989; *solid contours*, the elliptical region for extracting the spectrum of CXOU J184357−035441 (*dashed ellipse*), and the four point sources detected in CXOU J184357−035441 (*white plus signs*).

X-ray Spectra of G28.6−0.1

The X-ray spectra of G28.6−0.1 were separately made for observations 1 and 2, from the elliptical region of $11' \times 7\overset{'}{.}5$ shown by the ellipse in Figure 6.5. An elliptical region surrounding CXOU J184357−035441 (dotted line in Figure 2) was excluded to extract the energy spectrum. Although observation 2 covers full region, observation 1 covers only about the southern $\frac{1}{3}$. The point-source events, which are in the PSF (90% encircled radii) circles around the point sources detected with the *wavdetect* software, were removed from the source events. The background regions were selected at the same Galactic latitude as the source region, so that the GRXE are properly eliminated (e.g., Kaneda et al. 1997). The background regions for observations 1 and 2 are shown by circles in Figure 1. The point-source contribution was excluded from the background spectra, in a way similar to the source regions.

The background-subtracted spectra for observations 1 and 2 have no emission line, as shown in Figure 6.7. We fitted the spectra with a power-law model. The fits are acceptable with χ^2/degree of freedom (d.o.f.) $= 18.9/27$ and $48.1/52$ for observations 1 and observation 2, respectively. The best-fit parameters are given in Table 6.8. Although the spectrum of observation 1 represents only the southern part of G28.6−0.1, the spectral parameters,

except the flux, are consistent with those of observation 2, the full spectrum of G28.6−0.1. We therefore carried out a simultaneous fit to the observations 1 and 2 spectra with a power-law model leaving each normalization of the two observations independent. The fit is acceptable with the best-fit parameters given in Table 6.8.

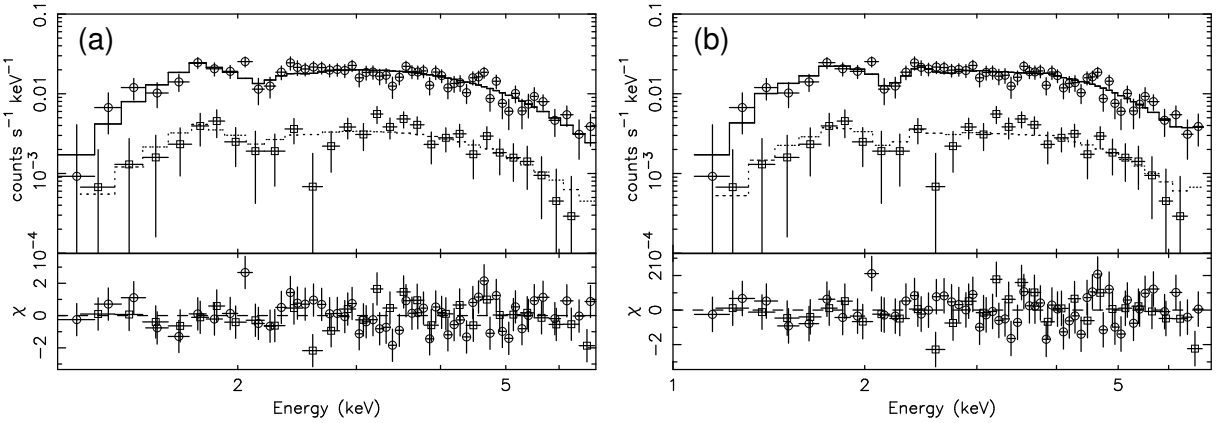

Figure 6.7: Spectra of G28.6−0.1 derived from observation 1 (*squares*) and observation 2 (*circles*) with the best-fit models in the simultaneous fitting for observation 1 (*dotted lines*) and observation 2 (*solid lines*). Fitted models are a power-law model (a) and a NEI model (b), respectively.

To examine the possibility of a thermal plasma origin, we also proceeded with a simultaneous fit with a model of a thin thermal plasma in non-equilibrium ionization (NEI; Borkowski et al. 2001b). This NEI model is acceptable with the best-fit parameters in Table 6.8. The metal abundances, however, are lower ($\sim$ 0.2 solar) and the temperature is higher ($\sim$ 5.4 keV) than any of the diffuse thermal sources (e.g., SNRs and star forming regions) in the Galaxy.

X-ray Spectrum of CXOU J184357−035441

The X-ray spectrum of CXOU J184357−035441 was made from the full elliptical region of $50'' \times 30''$ shown in Figure 6.6. We used the same background spectrum as that for G28.6−0.1 in observations 2. As is shown in Figure 6.8, the background-subtracted spectrum is much softer than that of G28.6−0.1 and shows clear emission lines at 1.85 and 2.41 keV, which are equal to or slightly lower than those from He-like Si and S. We fitted the spectrum with an NEI model. This model is acceptable with the best-fit parameters given in Table 6.9 and the best-fit model in Figure 6.8.

Table 6.8: Best-Fit Model Parameters for G28.6−0.1 with *Chandra*.

	power-law			NEI
Parameter	Observation 1	Observation 2	Observation 1+2	Observation 1+2
Γ/kT [keV].....	$2.4^{+1.1}_{-0.9}$	$2.1^{+0.4}_{-0.4}$	$2.1^{+0.4}_{-0.3}$	$5.4^{+3.5}_{-1.6}$
Abundance.....	···	···	···	$0.17^{+0.17}_{-0.14}$
$\log(n_{\rm e}t$ [cm^{-3} s])	···	···	···	$11.1^{+0.4}_{-0.7}$
$N_{\rm H}$ [10^{22} cm^{-2}]	$4.7^{+2.8}_{-1.8}$	$3.7^{+0.7}_{-0.6}$	$3.8^{+0.7}_{-0.6}$	$3.5^{+0.6}_{-0.5}$
Absorbed flux[a].....	2.3	3.1	3.1[b]	3.0[b]
Unabsorbed flux[c]	3.6	4.3	4.3[b]	4.1[b]
χ^2/d.o.f.	18.9/27	48.1/52	68.1/81	65.3/79

[a] Observed flux (10^{-14} ergs cm^{-2} s^{-1} arcmin^{-2}) per unit area (arcmin^2) in 2.0–10.0 keV.

[b] The fluxes of observation 1+2 are calculated from the normalizations for the spectrum of observation 2, which covers whole G28.6−0.1.

[c] Absorption-corrected flux per unit area (10^{-14} ergs cm^{-2} s^{-1} arcmin^{-2}) in 2.0–10.0 keV.

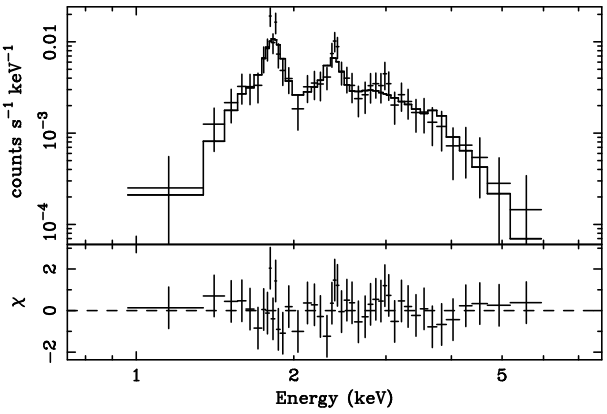

Figure 6.8: Background-subtracted spectrum of CXOU J184357−035441. *Solid line*: Best-fit NEI model.

6.2.3 Discussion on G28.6−0.1 and surroundings

G28.6−0.1

We found that the newly identified SNR, G28.6−0.1, has many X-ray clumps, which are globally filling an elliptical region. The X-ray spectrum is well-fitted with either a power-law or a thin thermal plasma model, similar to the *ASCA* spectrum. *Chandra* gives more severe constraint on the thin thermal parameters than *ASCA*, due mainly to the removal of the

Table 6.9: Best-fit parameters for CXOU J184357−035441 by the NEI model.

Parameter	Value
kT	$0.71^{+0.22}_{-0.16}$ keV
Abundance	$1.1^{+1.4}_{-0.7}$
$\log[n_e t$ (cm^{-3} s)]	$10.4^{+1.5}_{-0.3}$
$N_{\rm H}$	$7.4^{+1.6}_{-1.2} \times 10^{22}$ cm^{-2}
Absorbed flux[a].....	1.1×10^{-13}erg cm^{-2} s^{-1}
Unabsorbed flux[b] ...	4.5×10^{-11}erg cm^{-2} s^{-1}
χ^2/d.o.f.	22.2/39

[a]Observed flux in the energy band 0.7–10.0 keV.

[b]Absorption-corrected flux in the energy band 0.7–10 keV.

contamination from the thermal source CXOU J184357−035441. The thermal scenario of G28.6−0.1 requires uncomfortably high temperature (> 3.8 keV) and low metal abundance (< 0.34 solar; Table 6.8). This strengthens the conclusion made with *ASCA* that the X-rays of G28.6−0.1 is non-thermal origin with a power-law spectrum.

The absorption ($N_{\rm H}$) of $(3.2 - 4.5) \times 10^{22}$ cm^{-2} determined with *Chandra* is slightly larger than, but roughly similar to the *ASCA* result. We therefore adopt the source distance of 7 kpc, following the discussion given in §6.2.1. The X-ray luminosity (2.0–10.0 keV) and the source size are then estimated to be 1.5×10^{34} ergs s^{-1} and 18 pc (mean diameter), respectively.

Since the spectrum is a power-law with the photon index of 2.1 (the energy index of 1.1), the X-rays would be due to synchrotron emission from high energy electrons in a power-law distribution. The corresponding spectral index of the electrons is 3.2, which is larger than the value of 2 which is expected by the first-order Fermi acceleration. This steepening in the X-ray band is also seen in all of the well established SNRs as a site of high energy electrons (SN 1006, G347.3−0.5, and G266.2−1.2, e.g., Koyama et al. 1995, 1997; Slane et al. 2001), and their photon indices are very similar (between $2.2 - 2.6$).

In order to study the wide-band spectrum of the synchrotron emission, we fitted the X-ray spectrum with an SRCUT model (Reynolds 1998), on an assumption that the energy index (α) in the radio band (1 GHz) to be 0.5 or 0.6. The derived cutoff energy and the flux density at 1.5 GHz are shown in Table 6.10. Here the absorption is consistent with the fit with the power-law model. Both of the predicted radio fluxes at 1.5 GHz (= 20 cm) by the SRCUT model are smaller than the summed flux of the radio clumps C, F, G, and

Table 6.10: Best-Fit Parameters by the SRCUT Model

Parameter	$\alpha = 0.5$[a]	$\alpha = 0.6$[a]
Cut-off frequency [10^{17} Hz]	7.2 $(2.8 - 27)$	11 $(2.2 - 92)$
Flux density[b] [Jy]	1.8 $(1.1 - 4.6) \times 10^{-2}$	0.11 $(0.07 - 0.45)$
$N_{\rm H}[10^{22}$ cm$^{-2}]$	$3.6^{+0.3}_{-0.2}$	$3.7^{+0.2}_{-0.3}$
χ^2/d.o.f.....	75.1/82	75.0/82

[a] The fixed value of α.

[b] Flux density at 1.5 GHz.

H ($\sim$1 Jy; Helfand et al. 1989). This apparent inconsistency may be due to our simple assumption that magnetic field strength (B) and density of high-energy electrons (n_e) are uniform in G28.6−0.1. A more realistic assumption is that the radio clumps have higher B than average, hence producing the high contrast in the radio image. On the other hand, the X-ray flux contrast in the radio clumps is small, because the number n_e of higher energy electrons (which emit X-rays) is smaller than average, because the synchrotron energy loss is large at high B. This scenario is consistent with the observed X-ray and radio morphology. In this case, the SRCUT model predicts that in the radio clumps the cutoff energy is lower and the X-ray spectrum is steeper than in the other regions. The limited photon flux, however, does not allow us to verify this scenario. Discrepancy between synchrotron X-ray and radio morphology is also seen in G347.3−0.5, an established source as an SNR emitting synchrotron X-rays (Slane et al. 1999).

CXOU J184357−035441

The X-ray energy spectrum of CXOU J184357−035441, thin thermal spectrum with 0.7 keV temperature and solar abundance, is typical for young and intermediate-age SNRs. Since the projected position of this source is in the SNR, G28.6−0.1, and is associated with the non-thermal radio source F (Helfand et al., 1989), a naive scenario is that CXOU J184357−035441 is a thermal counterpart of the SNR. It may be possible that we have a large shell whose soft X-ray emission is invisible because heavily absorbed. While a reverse shock is propagating toward the center, the core region makes harder spectrum. Hence, CXOU J184357−035441 might be one of the clumps made by the reverse shock. Adopting the same distance as G28.6−0.1 (7 kpc), we estimate that the X-ray luminosity (0.7–10.0 keV) is 2.7×10^{35} erg s^{-1} and the physical size is 1.7×1.0 pc of "head" and 1.0 pc-long "jet". Assuming a uniform density of a prorate sphere with $1.7 \times 1.0 \times 1.0$ pc diameters, the density of the "head" is

~ 15 cm^{-3}. From the ionization parameter ($n_e t$) of $(1.4 - 83) \times 10^{10}$ cm^{-3} s, this plasma would be heated-up very recently ($30 - 1700$ years ago), possibly by the reverse shock.

Since CXOU J184357−035441 exhibits 2 times larger absorption than G28.6−0.1, this source is likely located at the distance of 14 kpc. Derived plasma luminosity, size and density are still consistent with being a young SNR behind AX J1843.8−0352.

Since the absorption of CXOU J184357−035441 is nearly the same as the total Galactic absorption through the Galactic plane (Ebisawa et al., 2001), a possibility of an extragalactic source can not be excluded. The jet-like morphology is also unusual for an SNR plasma, but rather resembles the hot plasmas associated with the jet sources, like SS433 or AGN. It is unclear whether CXOU J184357−035441 is a thermal component associated with G28.6−0.1, another SNR located in the far side of our Galaxy, or an extragalactic source.

6.3 *XMM-Newton* Follow-up of G32.45+0.1

6.3.1 *XMM-Newton* Observation

Data reduction and image

G32.45+0.1 was observed with *XMM-Newton* in September 25, 2003. Although both the MOS and PN cameras were operated, the major part of G32.45+0.0 was not covered with the PN camera due to the CCD gaps and bad columns, and we verified that cleaned PN data do not improve precision of results obtained with the MOS cameras only. Therefore, we ignore the PN data. For data reduction and analysis, we have used the version 5.4.1 of the Standard Analysis System (SAS) software. Since the background showed flares, we accumulated the background light-curve of the full-field events with 10–12 keV energy, and screened out the time intervals when the count rate is larger than 0.3 count s^{-1}. After this filtering of the high background intervals, the effective exposure times of MOS1 and MOS2 are 20.5 and 21.2 ks, respectively.

Figure 6.9 shows the soft (0.5–2.0 kev) and the hard (2.0–7.0 keV) band X-ray images. Only in the hard band image (b), we see a shell-like diffuse structure, whose radius is about 4 arcmin.

In order to estimate the accurate flux of the diffuse X-rays, we picked up point-sources using the *ewavelet* software of the SAS, with the detection threshold of 5σ. Detected point sources are designated with crosses in Figure 6.10. Three sources are located in the diffuse shell, however, the extents of them determined by the *ewavelet* software are larger than the

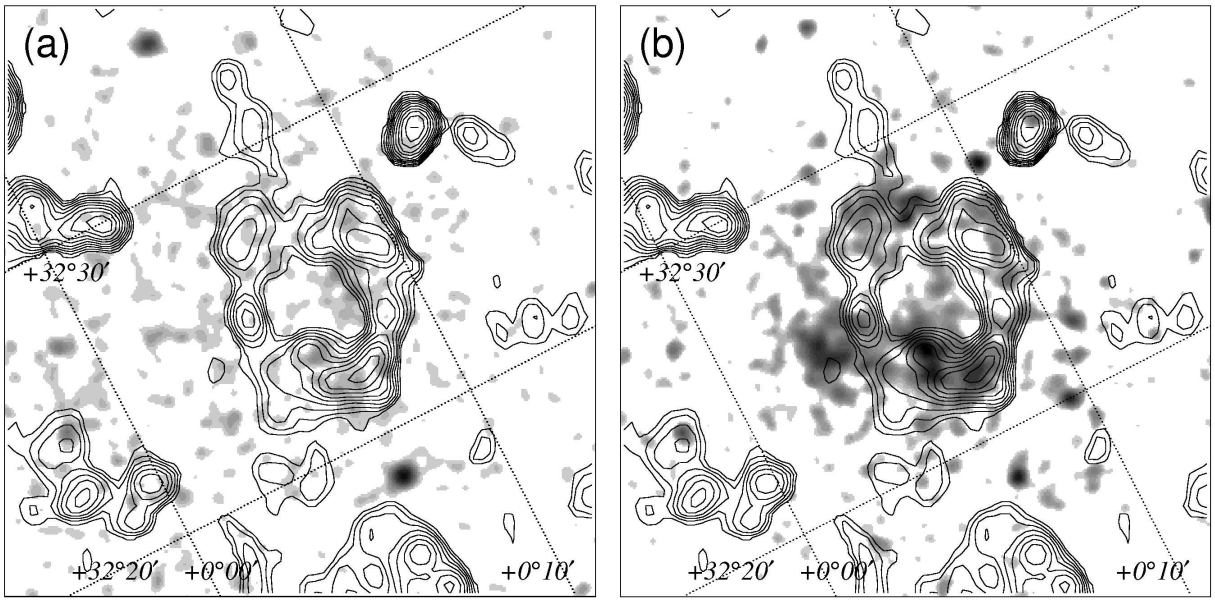

Figure 6.9: *XMM-Newton*/MOS1+2 images of G32.45+0.1 in the soft (0.5–2.0 keV; (a)) and the hard (2.0–7.0 keV; (b)) bands superimposed the NVSS 20 cm radio contours (Condon et al. 1998). The images are smoothed with a Gaussian kernel of $\sigma = 9\farcs6$. The coordinates are galactic.

Table 6.11: The positions and the extents of the point-like sources in the shell (*crosses* in the ellipses in Figure 6.9).

$(\mathrm{R.A.,\ Dec.})_{\mathrm{J2000}}$	region	extent (FWHM in arcsec)
$(18^{\mathrm{h}}50^{\mathrm{m}}19^{\mathrm{s}}, -00°26'20'')$	southeast	60 ± 25
$(18^{\mathrm{h}}50^{\mathrm{m}}06^{\mathrm{s}}, -00°25'58'')$	southwest	60 ± 25
$(18^{\mathrm{h}}50^{\mathrm{m}}05^{\mathrm{s}}, -00°26'04'')$	southwest	26 ± 6.1

point spread function of *XMM-Newton* (FWHM $\sim 5''$). We, therefore, conclude that these are not discrete point sources, but local enhancements of the diffuse emission. Thus, the diffuse structure discovered with the *ASCA* survey data was confirmed with the high spatial resolution of *XMM-Newton*.

Spectral Analysis

The spectrum was extracted from a region consists of three ellipses shown in Figure 6.10 (*solid-line*). The background was extracted from the neighborhood ellipses (Figure 6.10;

dotted-line). This region was selected so as that the intrinsic brightnesses of the background X-ray emission (the Galactic Ridge Emission; Kaneda et al. 1997) and the vignetting effect are the same for both the source and background regions; the background region is on the same distances from both the galactic plane and from the nominal point as the source region. The background-subtracted spectra of MOS1 and MOS2 are shown in Figure 6.11. Since these spectra are consistent with each other and have no emission line, we fitted them simultaneously with a power-law model modified by the interstellar absorption. The cross-sections of the absorption were adopted from Morrison & McCammon (1983), and the solar abundance (Anders & Grevesse 1989) was assumed. The fitting was statistically acceptable with the best-fit parameters given in Table 6.12.

To examine the possibility of a thermal plasma origin, we also tried fitting with a thin thermal plasma model in non-equilibrium ionization (an NEI model; Borkowski et al. 2001b), and as a result, obtained a statistically acceptable fit with the best-fit parameters shown in Table 6.12.

Table 6.12: Best-fit parameters of G32.45−0.1 for a power-law and a thin thermal plasma model with the *XMM-Newton* observations.

Model	Γ / kT .../(keV)	Abundance[†]	$\log(n_e t)$ [cm^{-3} s]	N_H (10^{22} cm^{-2})	χ^2 /d.o.f.
power-law.....	$2.2^{+0.8}_{-0.4}$	...	...	$5.2^{+2.3}_{-1.3}$	52.4/46
thin thermal plasma	$5.2^{+6.8}_{-2.2}$	$1.0 \times 10^{-2}(< 0.35)$	13.6	$4.6^{+1.5}_{-1.2}$	52.4/44

[†] Assuming the solar abundance ratio (Anders & Grevesse 1989).

6.3.2 Discussion on G32.45+0.1

We found a clear shell-like structure with a radius of $\sim 4'$ in the hard X-ray band (2.0–7.0 keV) with an *XMM-Newton* observation. The X-ray spectrum is well fitted with either a power-law or a thin thermal plasma model. Here, the thermal model requires temperature of 3.0–12 keV, which is similar to that of typical young SNRs such as Cas A and Tycho's SNR ($kT \sim 2-4$ keV; e.g.,). However, the thermal model also requires an low metal abundance (< 0.35 solar), which conflicts with the case of young SNRs. Typical X-ray emissions from young SNRs are dominated by those from ejecta, and the abundances are high (~ 2 solar). Therefore, the origin of the X-ray emission is not likely to be thermal, but non-thermal with the power-law spectrum.

The best-fit parameter of $N_H = 5.2(3.9-7.5) \times 10^{22}$ cm^{-2} gives rough estimation on

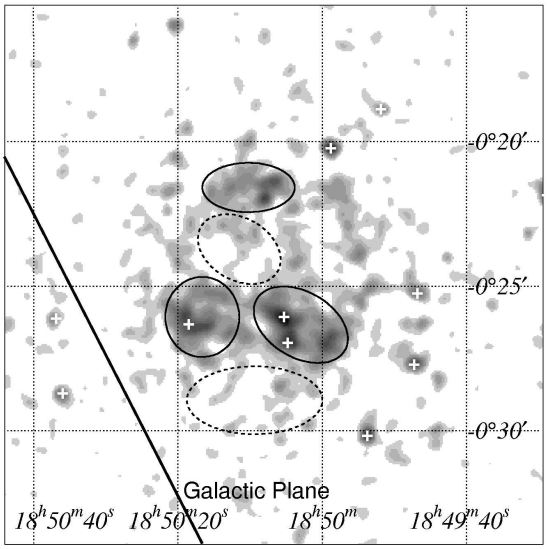

Figure 6.10: MOS1+2 hard-band (2.0–7.0 keV) image with the spectral regions. The source and background regions are shown with solid-line and dotted-line ellipses, respectively. The point-like sources detected with the *ewavelet* software are designated with white crosses. The coordinates are R.A. and DEC. (J2000).

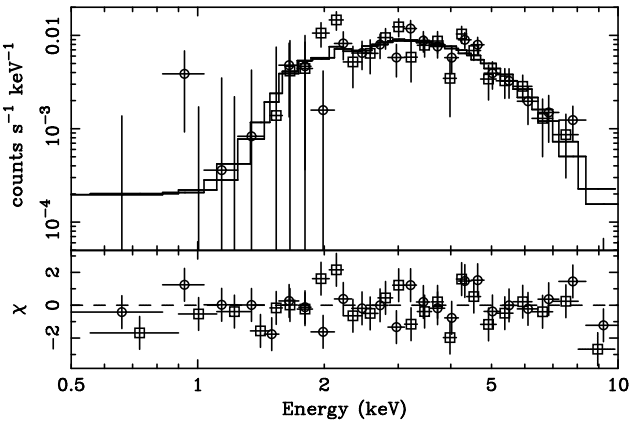

Figure 6.11: Background-subtracted spectra of G32.45+0.1 observed with MOS1 (*circle*) and MOS (*square*). The solid lines show the best-fit power-law models.

the source distance to be 17 kpc on an assumption that the averaged density in the galactic plane is 1 cm^{-3}. Then the X-ray luminosity (0.5–10 keV) and the radius are estimated to be $\sim 9.5 \times 10^{34}$ ergs s^{-1} and ~ 20 pc, respectively. These values are not largely different from those of the non-thermal component of SN 1006 ($\sim 2.0 \times 10^{34}$ ergs s^{-1} and ~ 9.5 pc; Dyer, Reynolds, & Borkowski 2004).

We found a radio shell at the position of G32.45+0.1 from the NRAO/VLA Sky Survey (NVSS) data at 1.4 GHz (Condon et al. 1998) with the flux sum ~ 0.17 Jy. Although the size of the shells seen in the X-ray and radio bands are quite similar, the enhanced positions are different between them. Bad correlation between X-ray and radio synchrotron emissions in SNRs was already pointed out in the discussion of G28.6−0.1, which can be explained by non-uniformity of the magnetic field strength. In order to discuss the wide-band spectrum assuming the synchrotron emission, we fitted the X-ray spectrum with a SRCUT model (Reynolds 1998). The best-fit parameters are shown in Table 6.13. The radio flux obtained

Table 6.13: Best-Fit Parameters by the SRCUT Model

Parameter	$\alpha = 0.5$[a]	$\alpha = 0.6$[a]
Cut-off frequency [10^{17} Hz]	3.4 (0.79–91)	5.4 (<35)
Flux density[b] [Jy]	1.6 (1.4–1.8)$\times 10^{-2}$	8.6 (7.4–9.4)$\times 10^{-2}$
$N_{\rm H}$[10^{22} cm^{-2}]	5.2 (4.5–6.2)	5.2 (4.4–6.1)
χ^2/d.o.f.	52.4/46	52.4/46

[a] The fixed value of α.

[b] Flux density at 1.4 GHz.

with the SRCUT model is lower than the observed flux in both the $\alpha = 0.5$ and $\alpha = 0.6$ cases. This is consistent our argument of magnetic field non-uniformity; the radio emission is detected from regions of stronger magnetic field, whereas the X-ray emission is detected from those of weaker magnetic field.

Chapter 7

Discussion

7.1 Properties of SNRs emitting synchrotron X-rays

In this thesis, we newly discovered SNRs emitting synchrotron X-rays: G28.6−0.1, G32.45+0.1. Moreover we found many candidates for such SNRs with the *ASCA* Galactic Plane Survey. It is notable that these SNRs are discovered with X-ray observations. Nowadays, up to 231 galactic SNRs are known (Green 2004), which are mostly discovered with radio observations. However, synchrotron X-rays are detected from only ∼10 SNRs. On the other hand, SNRs discovered with X-rays often show synchrotron X-rays (or non-thermal X-rays of other processes). These facts infer us that most SNRs emitting synchrotron X-rays are faint in the radio band.

In order to discuss this supposition, we utilize the Σ–D relation adding newly found SNRs. The Σ–D relation is a phenomenological relation between radio surface brightness and diameters of SNRs (e.g., Clark & Caswell 1976; Case & Bhattacharya 1998) introduced for estimating a distance of each SNR. The mean surface brightness at a specific radio frequency, Σ_ν, is a distance-independent parameter and, to a first approximation, is an intrinsic property of the SNR (Shklovskii 1960). Therefore, if the Σ–D relation is reliable, we can determine physical size (D) of a SNR from Σ, and as a result the distance is determined. Although it has been controversial that the Σ–D relation can be used for estimating distance of a SNR (e.g., Green 2004), there is a clear trend for the surface brightness of SNRs to decrease with increasing diameter. Moreover, diameters show approximate ages of SNRs at least. In order to see evolution stages of the newly found synchrotron X-ray sources and to compare their surface radio brightness with the other *radio selected* SNRs, we plotted them to the Σ–D relation.

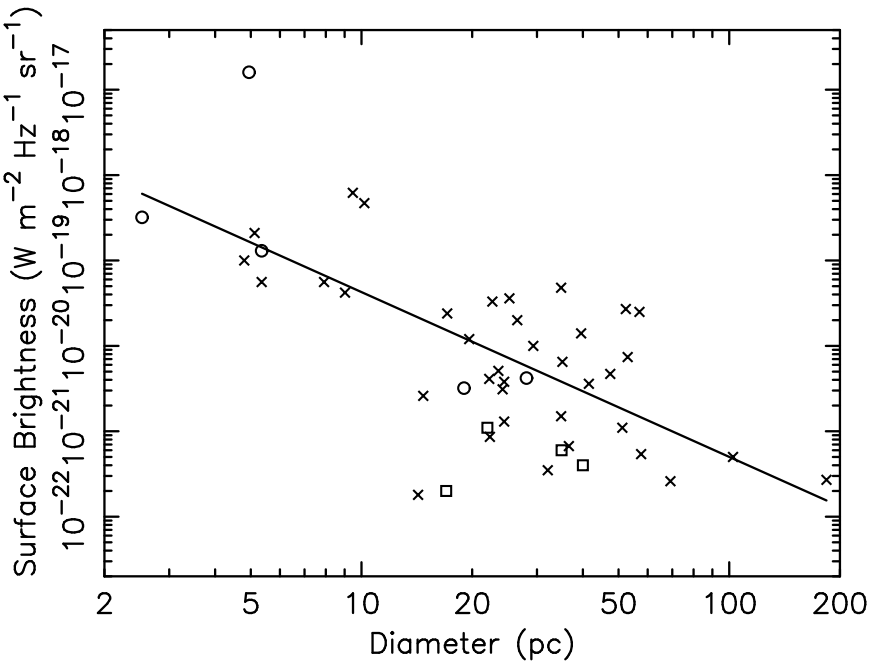

Figure 7.1: The surface brightness vs. diameter (Σ–D) relation for shell SNRs with known distances (see Table 7.1 and 7.2). The circles and crosses designate SNRs with and without synchrotron X-rays listed in Table 7.1. The squares designate SNRs we added (Table 7.2). The solid line shows the best-fit power-law function (see text)

As *radio selected* SNRs, we consider those lied in Table 2 of Green (2004). The utilized values of distances and sizes, and calculated diameters and radio surface brightnesses at 1 GHz are shown in Table 7.1. Those distances are measured mainly 4 methods independently of X-ray observations: e.g., optical expansion and proper motion studies, 21 cm H I absorption spectra, and association with H I or CO features in the surrounding ISM (see Green 2004). In order to restrict the discussion to shell SNRs, Crab-like "SNRs" were excluded here, which are cataloged with the type flag "F" in Green (2004). We also excluded W50 (G39.7−2.0) and RCW 89 (G20.4−1.2), since whether these objects are SNRs or not is controversial.

Figure 7.1 shows the resultant Σ–D relation. SNRs listed in Table 7.1 are designated with the circles and crosses depending on whether synchrotron X-rays have been detected or not, respectively. SNRs emitting synchrotron X-rays are Kepler's SNR (Cassam-Chenaï et al. 2004), Cas A (Vink & Laming 2003), Tycho's SNR (Hwang et al. 2002), RCW 86 (Bamba et al. 2000; Borkowski et al. 2001b), and SN 1006 (Koyama et al. 1995). Although

Table 7.1: Shell SNRs with Known Distances

Remnant	Other name	Distance[a] (kpc)	Size[a] (′)	D[b]	Σ[c]	n_0[d]	Reference
G4.5+6.8	Kepler's SNR	2.9	3	2.5	3.2×10^{-19}	···	···
G6.4−0.1	W28	1.9	48	27	2.0×10^{-20}	0.1	Rho & Borkowski (2002)
G11.2−0.3	···	4.4	4	5.1	2.1×10^{-19}	···	···
G18.8+0.3	Kes 67	14	14	57	2.5×10^{-20}	···	···
G21.5−0.9	···	4.6	4	5.4	5.6×10^{-20}	···	···
G27.4+0.0	Kes 73	6.8	4	7.9	5.6×10^{-20}	0.8	Gotthelf & Vasisht (1997)
G33.6+0.1	Kes 79	7.8	10	23	3.3×10^{-20}	0.2	Sun et al. (2004)
G34.7−0.4	W44	2.8	31	25	3.6×10^{-20}	0.08	Harrus et al. (1997)
G43.3−0.2	W49B	10	3.5	10	4.7×10^{-19}	0.5	Kawasaki et al. (2002)
G49.2−0.7	W51C	6.0	30	52	2.7×10^{-20}	0.14	Koo et al. (2002)
G53.6−2.2	3C400.2	2.8	30	24	1.3×10^{-21}	0.01	Yoshita et al. (2001)
G55.0+0.3	···	14	17	69	2.6×10^{-22}	···	···
G74.0−8.5	Cygnus Loop	0.4	190	22	8.6×10^{-22}	0.5	Miyata et al. (1994)
G84.2−0.8	···	4.5	18	24	5.1×10^{-21}	···	···
G89.0+4.7	HB21	0.8	100	24	3.1×10^{-21}	0.04	Leahy & Aschenbach (1996)
G93.3+6.9	DA 530	2.2	23	15	2.6×10^{-21}	0.01	Landecker et al. (1999)
G93.7−0.2	CTB 104A	1.5	80	35	1.5×10^{-21}	···	···
G109.1−1.0	CTB 109	3.0	28	24	3.8×10^{-21}	0.16	Sasaki et al. (2004)
G111.7−2.1	Cas A	3.4	5	4.9	1.6×10^{-17}	4.5	Willingale et al. (2003)
G114.3+0.3	···	0.7	70	14	1.8×10^{-22}	···	···
G116.5+1.1	···	1.6	70	32	3.5×10^{-22}	···	···
G119.5+10.2	CTA 1	1.4	90	37	6.7×10^{-22}	0.04	Slane et al. (1997)
G120.1+1.4	Tycho's SNR	2.3	8	5.4	1.3×10^{-19}	0.4	Seward et al. (1983)
G132.7+1.3	HB3	2.2	80	51	1.1×10^{-21}	0.015	Leahy et al. (1985)
G166.0+4.3	VRO 42.05.01	4.5	44	58	5.4×10^{-22}	0.01	Burrows & Guo (1994)
G166.2+2.5	OA 184	8.0	80	180	2.7×10^{-22}	···	···
G189.1+3.0	IC443	1.5	45	20	1.2×10^{-20}	1.0	Kawasaki et al. (2002)
G205.5+0.5	Monoceros	1.6	220	100	5.0×10^{-22}	0.003	Leahy et al. (1986)
G260.4−3.4	Pup A	2.2	55	35	6.5×10^{-21}	1	Petre et al. (1982)
G263.9−3.3	Vela (XYZ)	0.3	255	22	4.1×10^{-21}	···	···
G292.0+1.8	MSH 11-54	6.0	10	17	2.4×10^{-20}	0.51	Gonzalez & Safi-Harb (2003)
G292.2−0.5	···	8.4	17	42	3.6×10^{-21}	···	···
G296.8−0.3	1156−62	9.6	17	47	4.7×10^{-21}	···	···
G315.4−2.3	RCW 86	2.3	42	28	4.2×10^{-21}	varies[e]	···
G327.4+0.4	Kes 27	4.8	21	29	1.0×10^{-20}	0.1	Enoguchi et al. (2002)
G327.6+14.6	SN 1006	2.2	30	19	3.2×10^{-21}	0.1	Bamba et al. (2003b)
G332.4−0.4	RCW 103	3.1	10	9.0	4.2×10^{-20}	2	Nugent et al. (1984)
G337.0−0.1	CTB 33	11	1.5	4.8	1.0×10^{-19}	···	···
G348.5+0.1	CTB 37A	8.0	15	35	4.8×10^{-20}	···	···
G348.7+0.4	CTB 37B	8.0	17	40	1.4×10^{-20}	···	···
G349.7+0.2	···	15	2.2	9.5	6.2×10^{-19}	1.0	Lazendic et al. (2004b)

[a] Cited from Green (2004).

[b] Physical diameter (pc).

[c] Radio surface brightness at 1 GHz (W m^{-2} Hz^{-1} sr^{-1}).

[d] Ambient medium density (cm^{-3}) cited from the references. We adopted those calculated from the emission measures of the forward-shock plasmas. We assumed the forward-shock plasma is 4 times compressed than the ambient medium.

[e] Spatial variation of n_0 is large (e.g., Vink, Kaastra, & Bleeker 1997).

Table 7.2: Shell SNRs Emitting Synchrotron X-rays

Remnant	Other name	Distance (kpc)	Size (′)	D^{a}	Σ^{b}	Reference
G28.6−0.1	A J1843.8−0352	7	11	22	1×10^{-21}	this thesis
G32.45+0.1	···	17	8	40	4×10^{-22}	this thesis
G266.2−1.2	RX J0852.0−4622	<1	120	< 30	5×10^{-22}	Duncan & Green (2000)
G347.3−0.5	RX J1713.7−3946	1.0	60	17	2×10^{-22} [c]	Lazendic et al. (2004a)

[a] Physical diameter (pc).

[b] Radio surface brightness at 1 GHz (W m^{-2} Hz^{-1} sr^{-1}).

[c] The surface brightness of G347.3−0.5 as a whole was estimated from Fig. 6 in Lazendic et al. (2004a), regarding the lowest contour level (0.5 mJy beam^{-1}) is the average surface brightness of G347.3−0.5.

the scatter is large, we can see a trend that Σ becomes smaller as D becomes larger. When we fitted the Σ–D relation in Figure 7.1 with a power-law function, the best-fit function was,

$$\Sigma_{1\ \mathrm{GHz}} = 3.6 \times 10^{-18} \times D^{-1.9}\ \mathrm{W\ m^{-2}\ Hz^{-1}\ sr^{-1}}, \tag{7.1}$$

which is shown with the solid line in Figure 7.1. In this fitting, SNRs listed in Table 7.1 (*crosses* and *circles*) were included.

We next added SNRs emitting synchrotron X-rays, both of those already known and those we found, which are shown in Table 7.2. These SNRs are designated with the squares in Figure 7.1. The distances of G28.6−0.1 and G32.45−0.1 are estimated from the X-ray absorption column density (§6.2.3 and 6.3.2). Just as expected, SNRs emitting synchrotron X-rays are mainly located in a region of small Σ. However, three sources (Cas A, and Tycho's and Kepler's SNRs) are located in a region of large Σ.

On the ground that diameters approximately show the ages of SNRs, we can summarize this situation as follows: when SNRs are young, most of them emit synchrotron X-rays. As they evolve, some SNRs faint in radio continue to emit synchrotron X-rays, whereas the others stop the emission. Therefore, it is suggested that the faintness in the radio band is connected with the lifetime of synchrotron X-ray emission in each SNR.

Then what determines the radio surface brightness other than the diameter. The power of synchrotron radiation is proportional to the product of the magnetic field strength and the electron density, and furthermore, the magnetic field strength is known to correlate with the ambient density. Therefore, we can first suspect ambient density is responsible for the scatter of Σ. In order to test whether the scatter of Σ is due to ambient densities, we derived the ratios between Σs expected by the Σ–D relation (equation 7.1) and the observed Σs, and plotted them against ambient densities. Ambient densities can be derived from X-ray

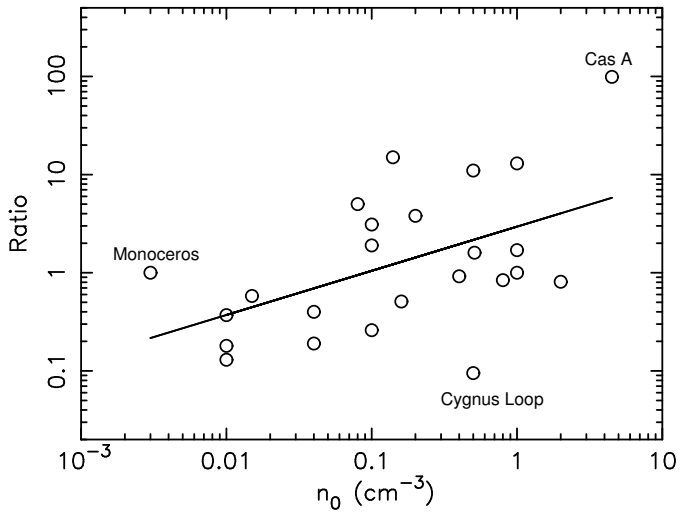

Figure 7.2: The ratio between Σs expected by the Σ–D relation and observed Σs plotted against ambient densities.

observations; ambient densities are cited from literature as shown in Table 7.1. We here picked up only those derived from X-ray luminosities.

Figure 7.2 shows the resultant plot. Although the scatter is large, we can see a positive correlation between ambient densities and the ratios of observed Σs against the Σ–D relation. The correlation index is calculated to be 0.41, and supports the positive correlation. This result confirms that one of the causes for the scatter of Σ is ambient densities of SNRs. Therefore, we can conclude that SNRs which emit synchrotron X-rays for longer time are likely to be located in low density regions.

If we assume the electrons are accelerated by the standard diffusive shock acceleration (e.g., Drury 1983; see Appendix C), we have a relation between the cut-off frequency of synchrotron emission ν_{cutoff} and the shock velocity V such as:

$$\nu_{cutoff} \approx 5 \times 10^{17} \left(\frac{V}{2000 \text{ km s}^{-1}} \right)^2 \xi^{-1} \text{ Hz}, \tag{7.2}$$

where ξ is the gyrofactor. This relation shows that whether electron synchrotron emission is extending up to the X-ray band or not is determined only by the velocity of the shock (ξ is assumed to be ~ 1 and rather constant even for various SNRs). Since SNRs expand sweeping up the ambient matter, in order to maintain the shock velocity high for longer time, the ambient density must be low. For example, in order to maintain the shock velocity V larger than 2000 km s^{-1} until the shell radius is 20 pc, on assumption the SNR is in the

Sedov phase, the ambient density n_0 must be:

$$n_0 < 0.13 \left(\frac{E_0}{10^{51}\ \mathrm{erg}}\right) \left(\frac{D}{20\ \mathrm{pc}}\right)^{-3/5} \left(\frac{V}{2000\ \mathrm{km}}\right)^{-2/5}\ \mathrm{cm}^{-3}, \tag{7.3}$$

where E_0, D are the initial explosion energy of the supernova, and the diameter, respectively. Thus, our hypothesis that SNRs emitting synchrotron X-rays longer time are located in low density region is also supported theoretically.

Our result predicts that small SNRs or radio faint SNRs emit synchrotron X-rays. This may be the case for SNR 0509−67.5, a shell-type SNR in the Large Magellanic Cloud with 7 pc-diameter, in which Warren & Hughes (2004) suggested existence of synchrotron X-rays after a detailed analysis of a *Chandra* observation. However, it is clear that not all the SNRs with small diameters or not all the SNRs faint in radio emit synchrotron X-rays. We suspect there are other causes for the scatter of Σ, for example, the explosion energies of supernovae. Since the number of accelerated electrons is expected to be less in supernova remnants of low energy, brightnesses in radio wwill be small in such SNRs, which is analytically discussed by Berezhko & Völk (2004). However, variation of explosion energies of supernova remnants are not well understood yet.

Our result supports that the shock speed is an important parameter to determine whether we can expect synchrotron X-ray emission from an SNR. Since the thermal energy of the shocked plasma is a conversion of the kinetic energy of the shock, the temperature of the plasma would indicate the shock speed. However, the temperatures of ions and electrons may not have been equilibrated in such thin plasmas in SNRs. For example, though the speed of the north-west shock of SN 1006 ($\sim$2900 km s^{-1}; Winkler, Gupta, & Long 2003) suggests the temperature of the plasma behind the shock is $\sim$ 10 keV, the electron temperature of the plasma measured to be only $\sim$ 0.9 keV (Long et al. 2003). The measurement of the ion temperatures will be possible in the near future; high energy resolution spectroscopy with such instruments as XRS onboard Astro-E2 will enable us to measure thermal Doppler broadening of the emission lines from ions. Hα observations have also been determining the speed of SNR shocks (e.g., Chevalier et al. 1980). However, not only SNRs do not always emit Hα lines but also the regions accompanying synchrotron X-ray emissions are often weak in Hα emissions (e.g., Rho et al. 2002). Therefore, future X-ray observations with high energy resolution would be important in studying the relation between shockk speed and X-ray synchrotron emission.

Protons and ions are expected to be accelerated simultaneously with electrons. Since synchrotron energy loss is negligible for them, the maximum energy is only determined by the acceleration time scale. Under the diffusive shock acceleration theory, the acceleration

time scale is proportional to V^{-2} (see Appendix C). Since shock speeds of SNRs in lower density medium is maintained large for longer time, those SNRs may be responsible for the maximum energy of galactic cosmic rays. According to the discussion above, those SNRs are likely to be faint in radio, and may be found with X-ray observations.

7.2 Properties of the SNR candidates

Although the number of SNRs emitting synchrotron X-ray emission have been small, our discovery of new SNRs and candidates indicate that many such SNRs are located in the galactic plane, and that those are likely to be discovered with X-ray observations.

Assuming the brightness of SN 1006, we estimate the deepness of our search with the data set of the *ASCA* Galactic Plane Survey. In order to compare brightnesses and sizes of the new extended X-ray sources with those of SN 1006, we plotted them in Figure 7.3. The solid-line corresponds to the same brightness as SN 1006, and corresponds to the case that SN 1006 were located more distant. From this plot, we see that we are detecting sources dimmer than 1/2 brightness of SN 1006. If we exclude the galactic center region, the maximum absorption column density within the galaxy is $\sim 5 \times 10^{22}$ cm^{-2} (Ebisawa et al. (2001)). With this absorption column density, 50% of X-ray photons are absorbed in the 2.0–10.0 keV band. However, we can detect sources with dimmer then 1/2 brightness of SN 1006, the sensitivity is enough to detect a distant "SN 1006". On the other hand, a distant "SN 1006" becomes small, the spatial resolution is required to detect the extension. Since the resolution of *ASCA* corresponds to $6'$, "SN 1006" at a distance of 10 kpc is the detection limit.

SNRs located at low longitude are likely to originate from Type II supernovae. Therefore, their distribution is expected to be similar to that of the H II regions, and further that of CO molecular cloud. In order to estimate coverage of the survey, we simply assume a finite disk model for the number density of SNRs η:

$$\eta(r,z) = \begin{cases} \eta_0 \exp\left[-\frac{1}{2}\left(\frac{|z|}{Z_s}\right)^2\right] & (r <= R_d) \\ 0 & (r > R_d) \end{cases} \tag{7.4}$$

According to Sanders et al. (1984), the scale hight of CO (Zs) is $\sim$ 60 pc. We assume $R_d = 5$ kpc, at which radius the galactocentric arms are located (Sanders et al. 1984). We found 37% of the putative SNRs are located in the region covered by the *ASCA* survey ($|l| < 45°$, $|b| < 0.4°$, distance <10 kpc). However, 34% of the survey region

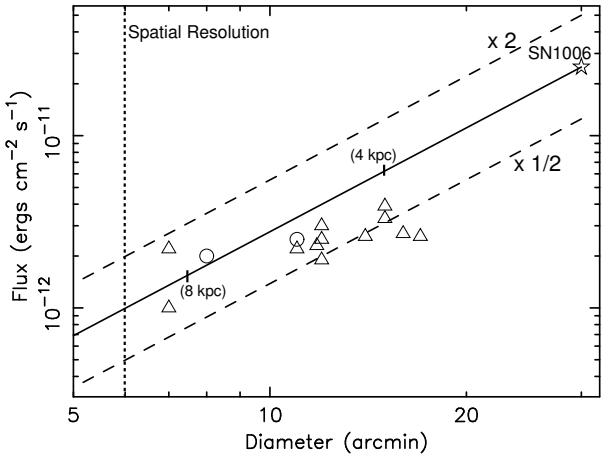

Figure 7.3: Plot of diameters and fluxes for the new extended X-ray sources. SN 1006 is designated with the star, new synchrotron X-ray SNRs, G28.6−0.1 and G32.45+0.1 are with the circles, and other sources are with the triangles. The solid-line shows the points where the surface brightness is the same as SN 1006. If SN 1006 were located at the distance in the parentheses, the diameter and the brightness have the values at the point.

is suffered from stray light and could no be used for extended-source search. Therefore, $1/0.37/(1-0.34)$ ∼4 times the number of SNRs detected with the *ASCA* survey is expected in the galactic plane. In the *ASCA* survey region, at least 3 SNRs emitting synchrotron X-rays (G347.3−0.5, G28.6−0.1, and G32.45+0.1) are located. Among our 15 candidates, G26.6−0.1, G316.8−0.1, and G318.6+0.0 are not likely to be SNRs. Therefore, the number of SNRs emitting synchrotron X-rays in the survey is at most $12 + 1$ (G347.3−0.5)= 13. Therefore, we expect 12∼52 SNRs emitting synchrotron X-rays in the galactic plane.

The discussion in §7.1 indicate that SNRs emitting synchrotron X-rays are located in low-density regions. This seems to be conflicting with that our new SNRs and candidates are located on the low Galactic latitude, where the most of the mass in the galaxy is concentrated. One plausible situation is that the progenitor of these SNRs are exploded in cavities made by stellar wind. One example is recently demonstrated for G347.5−0.5 with a CO observation by Fukui et al. (2003). They argue G347.3−0.5 exploded in a cavity and is expanding at high velocity ∼5000 km s^{-1}. RCW 86 is also suggested to be an SNR exploded in a cavity by Vink, Kaastra, & Bleeker (1997). G28.6−0.1 may be another example for the cavity explosion. We found a strong anti-correlation between the *ASCA* X-ray image aand the CO map as shown in Figure 7.4. This anti-correlation is not likely to be by chance, because the distance determined with X-ray is consistent with the kinematic distance with the CO-line;

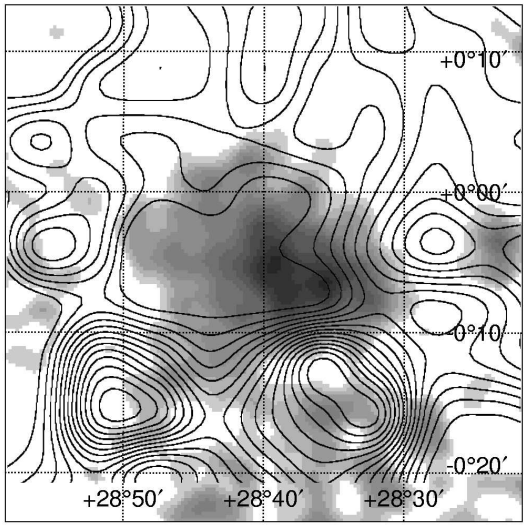

Figure 7.4: *ASCA* 0.7–7.0 keV image around G28.6−0.1 overlaid with the contours of the CO intensity map (courtesy of Y. Moriguchi, the NANTEN group). The CO intensity is derived by integrating the CO spectra from 80 to 90 km s^{-1}. The contours are plotted from 30 K km s^{-1} with intervals of 5 K km s^{-1}.

the former is 7 kpc (see §6.2.1) and the latter is 7.5 kpc.

Appendix A

Background Light Curves of *XMM-Newton*

All the background light curves of the *XMM-Newton* observations appearing in this thesis are accumulated here. These lightcurves are created over the whole detector for signle events in the energy range 10–15 keV and with FLAG values as defined by #XMMEA_EP or #XMMEA_EM depending on the PN or MOS cameras.

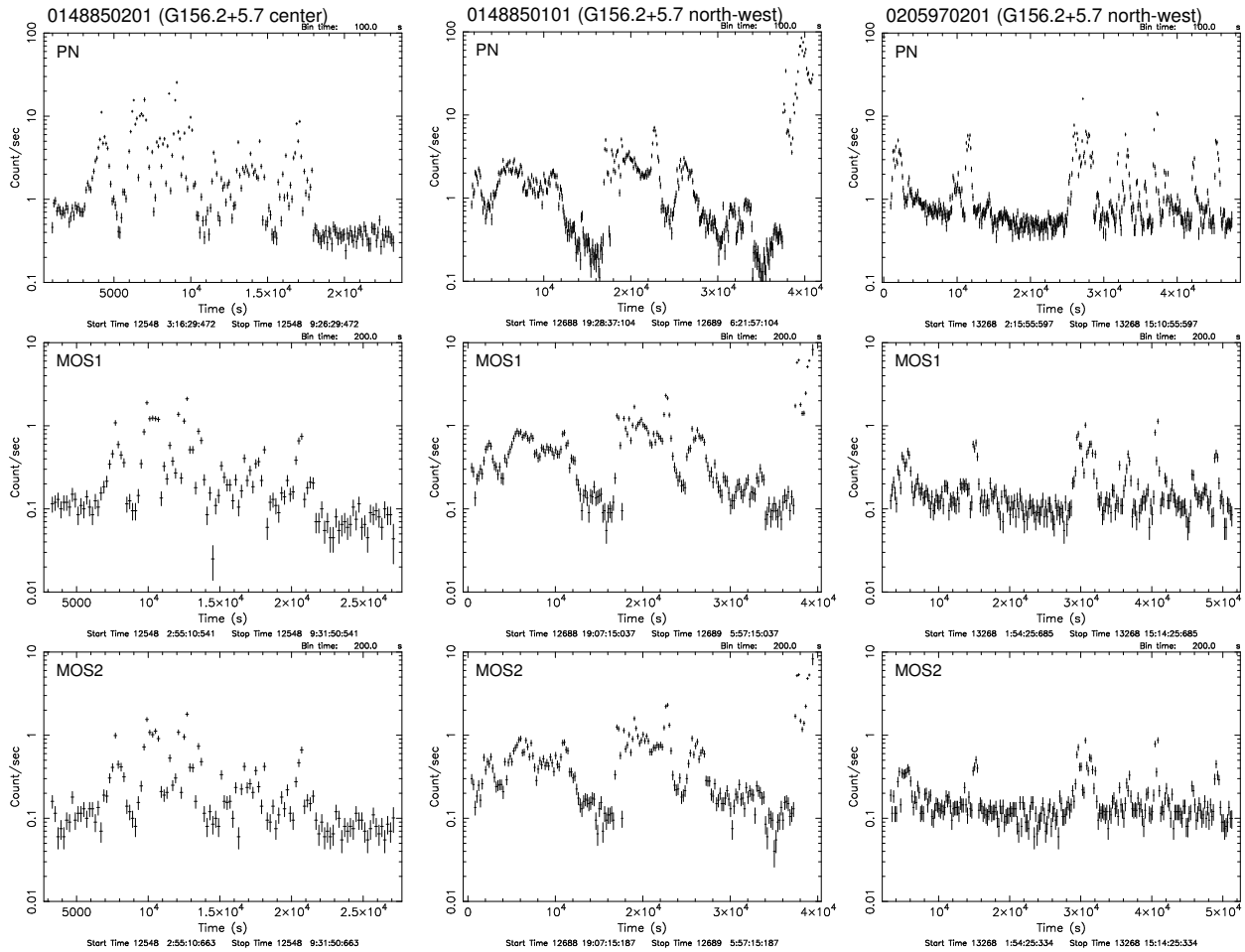

Figure A.1: Background light curves of *XMM-Newton* observations (1).

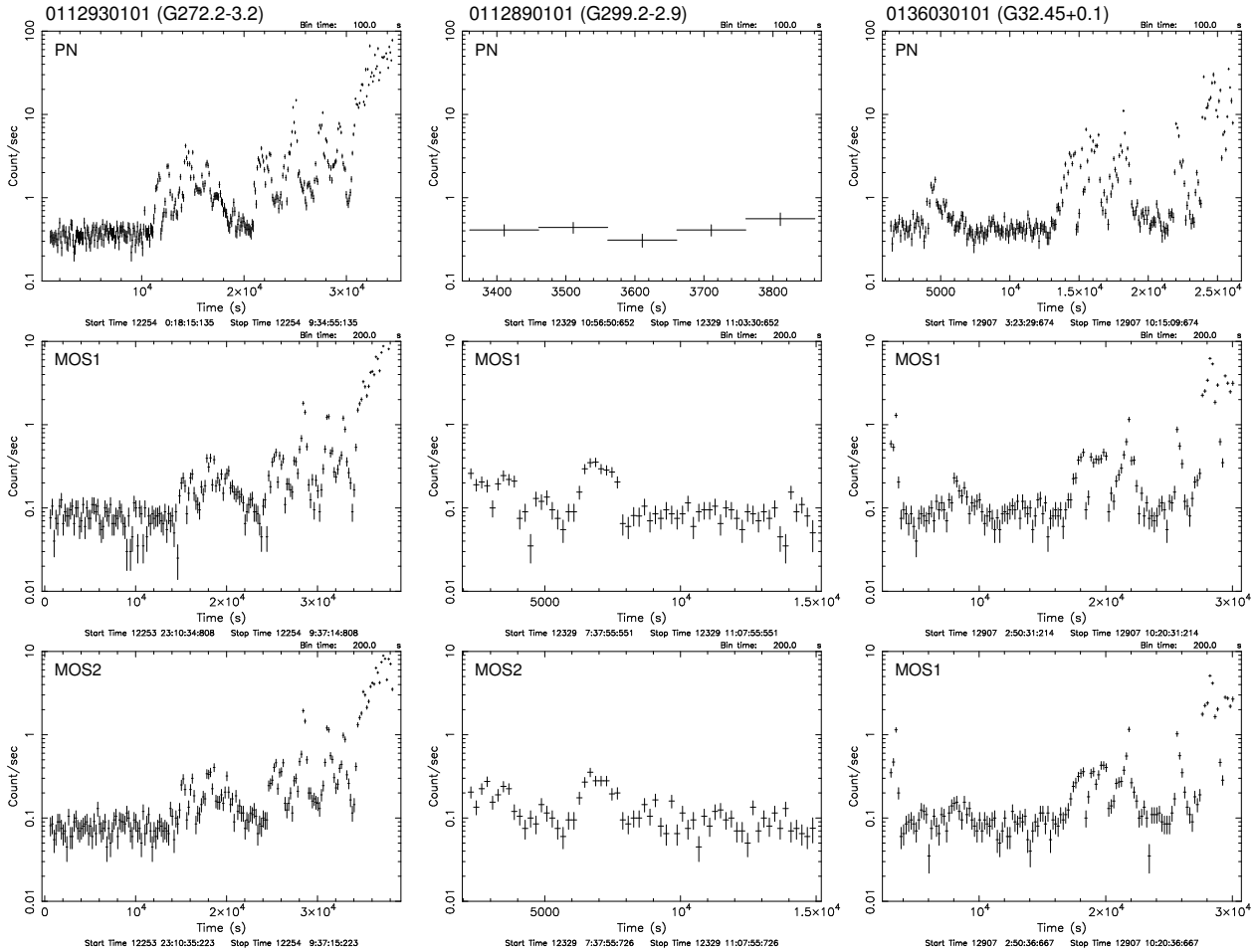

Figure A.2: Background light curves of *XMM-Newton* observations (2).

Appendix B

Serendipitous Discovery of a Cluster of Galaxy with *XMM-Newton*

In the *XMM-Newton* observation of G156.2+5.7, we serendipitously discovered a new cluster of galaxies. In this section, we report on the discovery.

This source was detected in the MOS1+2 image of the 2.0–7.0 keV band using the *emldetect* software. Figure B.1 shows the 0.5–7.0 keV image around the source. We can see a diffuse emission centering on at R.A.=$04^{\rm h}56^{\rm m}37\overset{\rm s}{.}2$, Dec.=$+52°24'12''$ (J2000). We will designate this source as XMMJ J0456372+522412 (or XMMJ J0456372) after its position.

In order to demonstrate the extension of XMMJ J0456372, we made a radial profile around XMMJ J0456372, excluding the nearby point sources detected with the *emldetect* software (*dotted-line circles* in Figure B.1). Figure B.2 shows the result. For comparison, we plotted a radial profile of a point source in the same FOV (source 2 in §4.1.3). Since off-axis angles of XMMJ J0456372 and source 2 are $7'$ and $10'$, respectively, the point spread function at XMMJ J0456372 is sharper than the radial profile of source 2. Thus we can see clearly that the X-ray emission of XMMJ J0456372 is extended about $\sim 45''$.

Source and background regions for the X-ray spectra were chosen to be a circular region of $50''$ and a surrounding annular region with inner and outer radii of $50''$ and $100''$, respectively (*solid-line circes* in Figure B.1). The background-subtracted PN and MOS spectra are shown in Figure B.3. The MOS1 and 2 spectra are combined after checking for the consistency. The spectra show a line-like structure around 5.5 keV, and a wavy structure around 1–2 keV, suggesting the X-ray emission is thermal. Since no abundant element emit X-ray line at 5.5 keV, the line is likely to be a redshifted Fe-K line. Accordingly, the extended

X-ray emission is suspected to be thin thermal plasma emission from a cluster of galaxies. We tried fitting the spectra with a thermal plasma model (APEC in XSPEC v11.3; Smith et al. 2001) allowing the redshift vary. As a result, we obtained an acceptable fit, with best-fit parameters and models shown in Table B.1 and Figure B.3, respectively. The absorption column density is consitent with the total galactic H I column density in this direction (Dickey & Lockman 1990).

If we use a hubble constant $H_0 = 50\ h_{50}$ km s^{-1} Mpc^{-1}, the spatial extent of 45″ radius at a redshift of 0.21 corresponds to a physical diameter of 0.7 h_{50}^{-1}Mpc.

The luminosity is calculated to be $1.0\times10^{44}\ h_{50}^{-3}$erg s^{-1}. According to the L_X–T relation (Arnaud & Evrard 1999), the temperature of 3.2 keV expects the luminosity to be 1.9×10^{22} erg s^{-1}, which agrees well with the observed value. This supports further that XMMJ J0456372 is a cluster of galaxies.

When we searched for counterparts in other wavelength using the NED data system, we found a 2MASS extended source, 2MASX J04563758+5224148, within the extended emission of XMMJ J0456372 (see Figure B.4). This infrared object must be a member galaxy of the cluter, XMMJ J0456372+522412, especially a cD galaxy resting in the center of the cluster.

Table B.1: Best-fit parameters of XMMJ J0456372+522412 with a APEC model.

kT (keV)	redshift	$N_{\rm H}$ (cm^{-2})	Flux[a] (erg cm^{-2} s)	χ^2 /d.o.f.
3.2 (3.0–3.7)	0.21 (0.15–0.23)	3.9 (3.2–5.0)$\times10^{21}$	3.5×10^{-13}	65.0/67

[a] Absorption-corrected flux in the 0.4–10.0 keV.

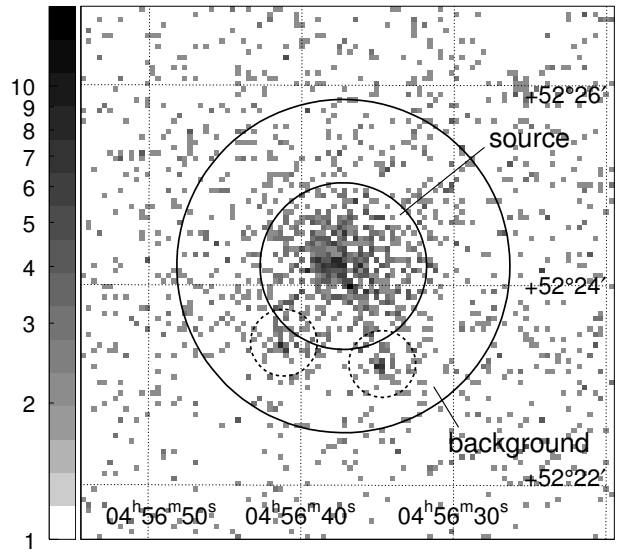

Figure B.1: MOS1+2 image of XMMJ J0456372+522412 in the 1.0–7.0 keV band. The PN and MOS1+2 spectra shown with gray and black, respectively. The spectral regions (source and background) are designated with solid-line circles. The regions around nearby point sources are excluded with the dotted-line circles from the spectral regions.

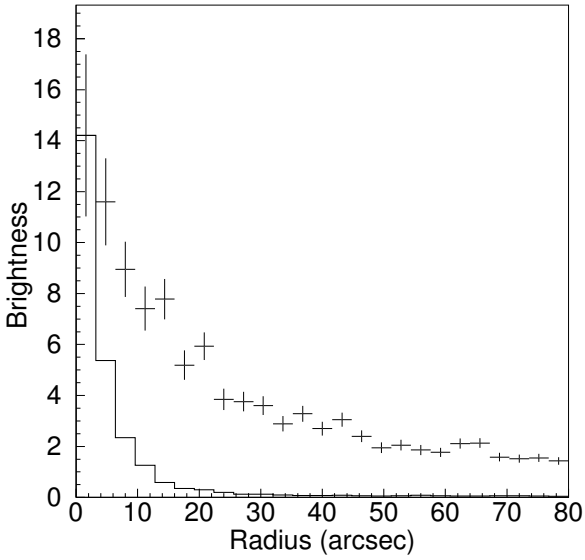

Figure B.2: Radial profile of XMMJ J0456372+522412 in the 1.0–7.0 keV bands (crosses). The vertical acis shows brightness ($\times 10^{-5}$ cnts cm^{-}2 s^{-1} arcmin^{-2}). The contribution of nearby point sources are excluded with 20″- radius regions. For reference, the radial profile of the point source, "source 2" (§4.1.3), normalized at the center is shown as the histogram.

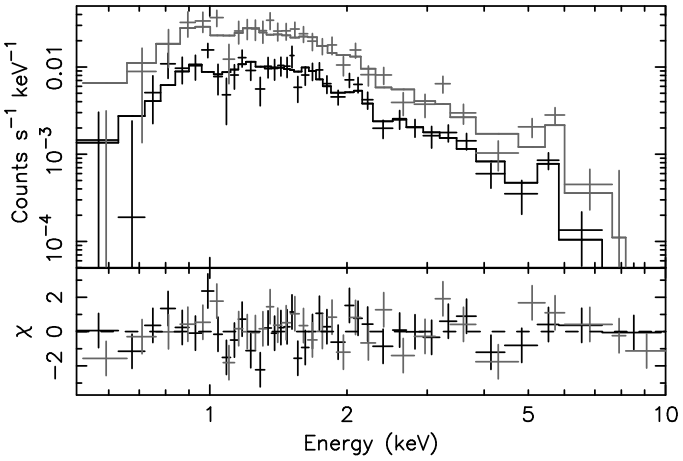

Figure B.3: EPIC spectra of XMMJ J0456372+522412. The best-fit APEC model is shown with the solid-line.

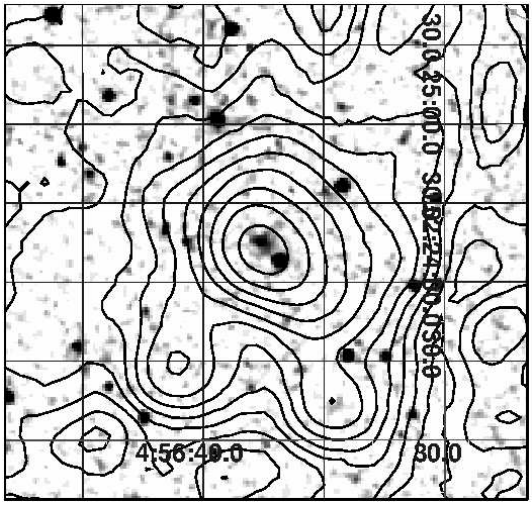

Figure B.4: 2MASS Ks-band image around XMMJ J0456372+522412 overlaid with the MOS1+2 contours in the 1.0–7.0 keV band. Both the image and the contours are in logarithmic scale.

Appendix C

Diffusive Shock Acceleration

Since particles are accelerated by moving back and forth between the shocks, the acceleration time scale is determined by a time which a particles takes for one cycle Δt and a momentum gain per cycle Δp.

The time scale for a particle to complete one cycle is a sum of the mean residence times in the upstream and the downstream regions of each particle and given as

$$\Delta t = \frac{4}{v}\left(\frac{\kappa_1}{U_1} + \frac{\kappa_2}{U_2}\right), \tag{C.1}$$

where U_1 (U_2) and κ_1 (κ_2) are the fluid velocity and the diffusion coefficient in the upstream (downstream) region, respectively (Drury 1983). On the other hand, the mean momentum gain per cycle is given as

$$\Delta p = \frac{4}{3}\frac{U_1 - U_2}{v}p, \tag{C.2}$$

Then, the acceleration time scale is

$$t_{\rm acc} = \frac{p\Delta t}{\Delta p} = \frac{3}{U_1 - U_2}\left(\frac{\kappa_1}{U_1} + \frac{\kappa_2}{U_2}\right). \tag{C.3}$$

For the strong shock, the compression ratio can be assummed to be 4, and thus $U_2 = \frac{1}{4}U_1$. Then the acceleration time scale can be written simply as

$$t_{\rm acc} = \frac{4(\kappa_1 + 4\kappa_2)}{U_1^2}. \tag{C.4}$$

Therefore, the diffusion coeffecients κ_1, κ_2 are essential for the acceleration time scale (just as the name of the theory shows). The diffusion coefficient can be written as $\kappa = \frac{1}{3}\lambda_D c$, where λ_D is the mean free path of particle scattering. Since the particles are diffused by the

interaction with the magnetic field, the mean free path λ_D is thought to be longer than the Lamour radius $r_L = E/ZeB$, and usually written as

$$\lambda_D = \xi r_L \tag{C.5}$$

with the so-called *gyrofactor* ξ, which is always larger than 1. Using ξ, we can write the diffusion coefficient as

$$\kappa = \frac{cr_L}{3}\xi. \tag{C.6}$$

Then, if we take $\kappa_1 = \kappa_2$ for simplicity, equations (C.4) and (C.5) yield

$$t_{\rm acc} = \frac{20}{3}\frac{cr_L}{V^2}\xi. \tag{C.7}$$

where V is the shock velocity ($= U_1$).

For electrons, the synchrotron energy loss is significant and the maximum energy is likely to be determined by the balance between the acceleration time scale and the synchrotron times scale. From equation (2.37), the synchrotron loss time scale is

$$t_{synch} = 1.25 \times 10^3 \left(\frac{E_e}{100\ \mathrm{TeV}}\right)^{-1} \left(\frac{B}{10\ \mu\mathrm{G}}\right)^{-2}\ \mathrm{yr}. \tag{C.8}$$

The maximum energy of accelerated electrons E_e is determined under the condition of $t_{acc} = t_{synch}$, and given as,

$$E_e \approx 67 \left(\frac{B}{10\ \mu\mathrm{G}}\right)^{-1/2} \left(\frac{V}{2000\ \mathrm{km\ s^{-1}}}\right) \xi^{-1/2}\ \mathrm{yr}. \tag{C.9}$$

References

Allen, D. A., Hyland, A. R., Longmore, A. J., Caswell, J. L., Goss, W. M., & Haynes, R. F. 1977, ApJ, 217, 108

Anders, E., & Grevesse, N. 1989, Geochim. Cosmochim. Acta, 53, 197

Arnaud, M., & Evrard, A. E. 1999, MNRAS, 305, 631

Arnett, W. D., Bahcall, J. N., Kirshner, R. P., & Woosley, S. E. 1989, ARA&A, 27, 629

Baade, W., & Zwicky 1934, Phys. Rev. 46, 76

Bai, L. & Wang, Z. 2000, ApJ, 539, 760

Bamba, A., Koyama, K., & Tomida, H. 2000, PASJ, 52, 1157

Bamba, A., Ueno, M., Koyama, K., & Yamauchi, S. 2001, PASJ, 53, L21

Bamba, A., Ueno, M., Koyama, K., & Yamauchi, S. 2003, ApJ, 589, 253

Bamba, A., Yamazaki, R., Ueno, M., & Koyama, K. 2003, ApJ, 589, 827

Becker R. H., & Helfand D. J. 1984, ApJ 283, 154

Becker, W. & Truemper, J. 1997, A&A, 326, 682

Bell, A. R. 1978, MNRAS, 182, 147

Berezhko, E. G. & Völk, H. J. 2004, A&A, 427, 525

Berkhuijsen, E. M. 1986, A&A, 166, 257

Blanton E. L., Helfand D. J. 1996, ApJ 470, 961

Borkowski, K. J., Lyerly, W. J., & Reynolds, S. P. 2001, ApJ, 548, 820

Borkowski, K. J., Rho, J., Reynolds, S. P., & Dyer, K. K. 2001, ApJ, 550, 334

Burke, B. E., Mountain, R. W., Daniels, P. J., Dolat, V. S., Cooper, M. J. 1994, IEEE Trans. Nucl. Sci. 41, 375

Burrows, D. N., & Guo, Z. 1994, ApJ, 421, L19

Busser, J. U., Egger, R., & Aschenbach, B. 1996, A&A, 310, L1

Case, G. L. & Bhattacharya, D. 1998, ApJ, 504, 761

Caswell J. L., Murray J. D., Roger R. S., Cole D. J., Cooke D. J. 1975, A&A, 45, 239

Cassam-Chenaï, G., Decourchelle, A., Ballet, J., Sauvageot, J.-L., Dubner, G., & Giacani, E. 2004, A&A, 427, 199

Cheng, K. S., Ho, C., & Ruderman, M. 1986, ApJ, 300, 500

Chevalier, R. A. 1974, ApJ, 188, 501

Chevalier, R. A., Kirshner, R. P., & Raymond, J. C. 1980, ApJ, 235, 186

Clark, D. H. & Caswell, J. L. 1976, MNRAS, 174, 267

Clifton, T. R. & Lyne, A. G. 1986, Nature, 320, 43

Condon, J. J., Cotton, W. D., Greisen, E. W., Yin, Q. F., Perley, R. A., Taylor, G. B., & Broderick, J. J. 1998, AJ, 115, 1693

Dickey, J. M., & Lockman, F. J. 1990, ARA&A, 28, 215

Dopita, M. A. 1988, Space Science Reviews, 46, 225

Drury, L. O'C. 1983, Rep. Prog. Phys., 46, 973

Duncan, A. R., & Green, D. A. 2000, A&A, 364, 732

Dyer, K. K. 2001, Ph.D. Thesis, North Carolina State University

Dyer, K. K., Reynolds, S. P., & Borkowski, K. J. 2004, ApJ, 600, 752

Dyer, K. K., Reynolds, S. P., Borkowski, K. J., Allen, G. E., & Petre, R. 2001, ApJ, 551, 439

Ebisawa, K., Maeda, Y., Kaneda, H., & Yamauchi, S. 2001, Science, 293, 1633

Ebisawa K., Bamba A., Kaneda H., Maeda Y., Paizis A., Sato G., & Yamauchi S. 2002, in the proceedings of "the New Visions of the X-Ray Universe in the XMM-Newton and Chandra Era" symposium at ESTEC (astro-ph/0203070)

Ellison, D. C., Slane, P., & Gaensler, B. M. 2001, ApJ, 563, 191

Enoguchi, H., Tsunemi, H., Miyata, E., & Yoshita, K. 2002, PASJ, 54, 229

Falle, S. A. E. G. 1981, MNRAS, 195, 1011

Folgheraiter, E. L., Warwick, R. S., Watson, M. G., & Koyama, K. 1997, MNRAS, 292, 365

Freeman, P. E., Kashyap, V., Rosner, R., & Lamb, D. Q. 2002, ApJS, 138, 185

Fukui, Y., et al. 2003, PASJ, 55, L61

Gaskell, C. M., Cappellaro, E., Dinerstein, H. L., Garnett, D. R., Harkness, R. P., & Wheeler, J. C. 1986, ApJ, 306, L77

Gonzalez, M., & Safi-Harb, S. 2003, ApJ, 583, L91

Gotthelf, E. V., & Vasisht G. 1997, ApJ 486, 133

Green, D. A. 2004, Bulletin of the Astronomical Society of India, 32, in press.

Greiner, J., Egger, R., & Aschenbach, B. 1994, A&A, 286, L35

Hamilton, A. J. S., & Sarazin, C. L. 1984, ApJ, 284, 601

Hands, A., Warwick, R., Watson, M., & Helfand, D. 2001, in the proceedings of "New Visions of the X-ray Universe in the XMM-Newton and Chandra Era", astroph/0202180

Harkness, R. P., & Wheeler, J. C. 1990, in Supernovae, ed. A. G. Petschek (New York: Springer-Verlag), 2

Harrus, I. M., Hughes, J. P., Singh, K. P., Koyama, K., & Asaoka, I. 1997, ApJ, 488, 781

Harrus, I. M., Slane, P. O., Smith, R. K., & Hughes, J. P. 2001, ApJ, 552, 614

Helfand, D.J., Velusamy, T., Becker, R. H., & Lockman, F. J. 1989, ApJ, 341, 151

Hofner, P., & Churchwell, E. 1997, ApJ, 486, L39

Holt, S. S., Gotthelf, E. V., Tsunemi, H., & Negoro, H. 1994, PASJ, 46, L151

Hwang, U., Hughes, J. P., & Petre, R. 1998, ApJ, 497, 833

Hwang, U., Decourchelle, A., Holt, S. S., & Petre, R. 2002, ApJ, 581, 1101

Ishisaki, Y. 1997, Ph.D. Thesis, Tokyo University (can be obtaind from http://www.metro.ac.jp/)

Iyudin, A. F., Aschenbach, B., Becker, W., Dennerl, K., Haberl F. 2004, A&A in press (astro-ph/0410372)

Kaneda, H., Makishima, K., Yamauchi, S., Koyama, K., Matsuzaki, K., & Yamasaki, N. Y. 1997, ApJ, 491, 638

Katayama, H., Takahashi, I., Ikebe, Y., Matsushita, K., & Freyberg, M. J. 2004, A&A, 414, 767

Kawasaki, M. T., Ozaki, M., Nagase, F., Masai, K., Ishida, M., & Petre, R. 2002, ApJ, 572, 897

Kinugasa, K. & Tsunemi, H. 1999, PASJ, 51, 239

Koo, B., Lee, J., & Seward, F. D. 2002, AJ, 123, 1629

Koyama, K., Makishima, K., Tanaka, Y., & Tsunemi, H. 1986, PASJ, 38, 121

Koyama K., Kawada M., Kunieda H., Tawara Y., Takeuchi Y., Yamauchi S. 1990, Nature 343, 148

Koyama, K., Petre, R., Gotthelf, E. V., Hwang, U., Matsuura, M., Ozaki, M., & Holt, S. S. 1995, Nature, 378, 255

Koyama, K., Kinugasa, K., Matsuzaki, K., Nishiuchi, M., Sugizaki, M., Torii, K., Yamauchi, S., & Aschenbach, B. 1997, PASJ, 49, L7

Kuchar, T. A. & Clark, F. O. 1997, ApJ, 488, 224

Landecker, T. L., Routledge, D., Reynolds, S. P., Smegal, R. J., Borkowski, K. J., & Seward, F. D. 1999, ApJ, 527, 866

Lazendic, J. S., Slane, P. O., Gaensler, B. M., Reynolds, S. P., Plucinsky, P. P., & Hughes, J. P. 2004, ApJ, 602, 271

Lazendic, J. S., Slane, P. O., Hughes, J. P., Chen, Y., & Dame, T. M. 2004, ApJin press

Leahy, D. A., Venkatesan, D., Long, K. S., & Naranan, S. 1985, ApJ, 294, 183

Leahy, D. A., Naranan, S., & Singh, K. P. 1986, MNRAS, 220, 501

Leahy, D. A., & Aschenbach, B. 1996, A&A, 315, 260

Long, K. S., Blair, W. P., & van den Bergh, S. 1988, ApJ, 333, 749

Long, K. S., Reynolds, S. P., Raymond, J. C., Winkler, P. F., Dyer, K. K., & Petre, R. 2003, ApJ, 586, 1162

Lumb, D. H., Warwick, R. S., Page, M., & De Luca, A. 2002, A&A, 389, 93

Malkov, M A., & Drury, L. O'C. 2001, Rep. Prog. Phys., 64, 429

Makishima, K., et al. 1996, PASJ, 48, 171

Masai, K. 1984, Ap&SS, 98, 367

Miyata, E., Tsunemi, H., Pisarski, R., & Kissel, S. E. 1994, PASJ, 46, L101

Moretti, A., Campana, S., Lazzati, D., & Tagliaferri, G. 2003, ApJ, 588, 696

Morris, D. J., et al. 2002, MNRAS, 335, 275

Morrison, R. & McCammon, D. 1983, ApJ, 270, 119

Nevalainen, J., Lumb, D., dos Santos, S., Siddiqui, H., Stewart, G., & Parmar, A. N. 2001, A&A, 374, 66

Nugent, J. J., Pravdo, S. H., Garmire, G. P., Becker, R. H., Tuohy, I. R., & Winkler, P. F. 1984, ApJ, 284, 612

Ohashi, T., et al. 1996, PASJ, 48, 157

Paladini, R., Burigana, C., Davies, R. D., Maino, D., Bersanelli, M., Cappellini, B., Platania, P., & Smoot, G. 2003, A&A, 397, 213

Pannuti, T. G. & Allen, G. E. 2004, Advances in Space Research, 33, 434

Petre, R., Kriss, G. A., Winkler, P. F., & Canizares, C. R. 1982, ApJ, 258, 22

Pfeffermann, E., et al. 1987, Proc. SPIE, 733, 519

Pfeffermann, E., Aschenbach, B., & Predehl, P. 1991, A&A, 246, L28

Read, A. M. & Ponman, T. J. 2003, A&A, 409, 395

Reich, W., Fuerst, E., & Arnal, E. M. 1992, A&A, 256, 214

Reynolds, S. P. 1998, ApJ, 493, 375

Reynolds, S. P., & Keohane, J. W. 1999, ApJ, 525, 368

Rho, J., & Borkowski, K. J. 2002, ApJ, 575, 201

Rho, J., Dyer, K. K., Borkowski, K. J., & Reynolds, S. P. 2002, ApJ, 581, 1116

Rybicki, G.B., & Lightman, A.P. 1979, "Radiative Processes in Astrophysics", Wiley-Interscience, New York

Sakano, M. 2000, Ph.D. Thesis, Kyoto University

Sanbonmatsu K.Y., Helfand D.J. 1992, AJ 104, 2189

Sanders, D. B., Solomon, P. M., & Scoville, N. Z. 1984, ApJ, 276, 182

Sasaki, M., Plucinsky, P. P., Gaetz, T. J., Smith, R. K., Edgar, R. J., & Slane, P. O. 2004, ApJ, 617, 322

Sedov, L. I. 1959, Similarity and Dimensional Methods in Mechanics, 10th ed. (New York: Academic Press)

Sekimoto, Y., Matsuzaki, K., Kamae, T., Tatematsu, K., Yamamoto, S., & Umemoto, T. 2000, PASJ, 52, L31

Serlemitsos, P. J., Jalota, L., Soong, Y., Kunieda, H., Tawara, Y., Tsusaka, Y., Suzuki, H., Sakima, Y. et al. 1995, PASJ 47, 105

Seta, M., et al. 1998, ApJ, 505, 286

Sevenster, M. N., Chapman, J. M., Habing, H. J., Killeen, N. E. B., & Lindqvist, M. 1997, A&AS, 122, 79

Seward, F., Gorenstein, P., & Tucker, W. 1983, ApJ, 266, 287

Seward, F. D. & Wang, Z. 1988, ApJ, 332, 199

Shaver, P. A., Retallack, D. S., Wamsteker, W., & Danks, A. C. 1981, A&A, 102, 225

Shemar, S. L. & Lyne, A. G. 1996, MNRAS, 282, 677

Shklovskii, I. S. 1960, Soviet Astronomy, 2, 243

Shklovskii, I. S. 1962, Soviet Astronomy, 6, 162

Slane, P., Vancura, O., & Hughes, J. P. 1996, ApJ, 465, 840

Slane, P., Seward, F. D., Bandiera, R., Torii, K., & Tsunemi, H. 1997, ApJ, 485, 221

Slane, P., Gaensler, B. M., Dame, T. M., Hughes, J. P., Plucinsky, P. P., & Green, A. 1999, ApJ, 525, 357

Slane, P., Hughes, J. P., Edgar, R. J., Plucinsky, P. P., Miyata, E., Tsunemi, H., & Aschenbach, B. 2001, ApJ, 548, 814

Smith, R. K., Brickhouse, N. S., Liedahl, D. A., & Raymond, J. C. 2001, ApJ, 556, L91

Sokolsky, P. 1989, Introduction to Ultrahigh Energy Cosmic Ray Physics (New York: Academic Press)

Sramek, R. A., Cowan, J. J., Roberts, D. A., Goss, W. M., & Ekers, R. D. 1992, AJ, 104, 704

Strüder, L., et al. 2001, A&A, 365, L18

Sturrock, P. A. 1971, ApJ, 164, 529

Sugizaki, M. 1999, Ph.D. Thesis, Tokyo University

Sugizaki, M., Mitsuda, K., Kaneda, H., Matsuzaki, K., Yamauchi, S., & Koyama, K. 2001, ApJS, 134, 77

Sun, M., Seward, F. D., Smith, R. K., & Slane, P. O. 2004, ApJ, 605, 742

Takahashi, T., et al. 1995, ASCA News, Vol. 3, p. 34

Tomida, H. 1999, Ph.D. Thesis, Kyoto University

Townsley, L. K., Feigelson, E. D., Montmerle, T., Broos, P. S., Chu, Y., & Garmire, G. P. 2003, ApJ, 593, 874

Turner, M. J. L., et al. 2001, A&A, 365, L27

Uchiyama, Y., Takahashi, T., & Aharonian, F. A. 2002, PASJ, 54, L73

Uchiyama, Y., Takahashi, T., Aharonian, F. A., & Mattox, J. R. 2002, ApJ, 571, 866

Uchiyama, Y., Aharonian, F. A., & Takahashi, T. 2003, A&A, 400, 567

Vink, J., Kaastra, J. S., & Bleeker, J. A. M. 1997, A&A, 328, 628

Vink, J., & Laming, J. M. 2003, ApJ, 584, 758

Warren, J. S. & Hughes, J. P. 2004, ApJ, 608, 261

Whiteoak, J. B. Z. & Green, A. J. 1996, A&AS, 118, 329

Willingale, R., Bleeker, J. A. M., van der Heyden, K. J., & Kaastra, J. S. 2003, A&A, 398, 1021

Winkler, P. F., Hanson, G. J., & Phillips, M. M. 1993, IAU Circ., 5715, 1

Winkler, P. F., & Long, K. S. 1997, ApJ, 491, 829

Winkler, P. F., Gupta, G., & Long, K. S. 2003, ApJ, 585, 324

Yamauchi, S., Ueno, S., Koyama, K., Nomoto, S., Hayashida, K., Tsunemi, H., & Asaoka, I. 1993, PASJ, 45, 795

Yamauchi, S., Koyama, K., Tomida, H., Yokogawa, J., & Tamura, K. 1999, PASJ, 51, 13

Yamauchi, S., et al. 2002, 8th Asian-Pacific Regional Meeting, Volume II, 81

Yamauchi, S., Ueno, M., Koyama, K., and Bamba, A. 2005, PASJsubmitted

Yoshita, K., Tsunemi, H., Miyata, E., & Mori, K. 2001, PASJ, 53, 93

Acknowledgement

I am deeply grateful to Prof. K. Koyama for his continuous guidance and support throughout the five years of my graduate school period. I also thank my collaborators, Prof. S. Yamauchi, Dr. K. Ebisawa, Dr. A. Bamba, Mr. H. Nakajima, and Mr. H. Yamaguchi for their helpful and constructive discussions.

I am grateful to all the members of the Cosmic-ray laboratory in Kyoto University for their continuous discussions, encouragements, and technical advice. I thank Prof. T. Kifune, Prof. M. Mori and all the members of the Cangaroo Team for the constructive discussions.

I would like to thank all the members of the *ASCA* team. The longer I get involved the X-ray astronomy, the more I recognize how the background of *ASCA* was low and how it is important.